FINAL REPORT

Mixing Processes in High-Level Waste Tanks

Principal Investigator
Per F. Peterson
Professor
Department of Nuclear Engineering
University of California, Berkeley
Berkeley, CA 94720-1730

DOE/EM Contract: FDDE-FG07-96ER14731-09/99

Project Duration:
Sept. 15, 1996 - Sept. 14, 2000

to:

Mark Gilbertson, EM-52
U.S. Department of Energy
Office of Environmental Management
Office of Science and Risk Policy
1000 Independence Avenue SW
Washington, DC 20585

and

Dr. Roland Hirsch, SC-73
U.S. Department of Energy
Office of Science
Office of Biological and Environmental Research
19901 Germantown Road
Germantown, MD 20874

Mixing Processes in High-Level Waste Tanks

May 24, 1999

Principal Investigator:
Per F. Peterson
Professor of Nuclear Engineering
Chair of Energy and Resources
University of California, Berkeley
Berkeley, CA 94720-1730
Office: (510) 643-7749 Fax: (510) 643-9685
peterson@nuc.berkeley.edu

RESEARCH OBJECTIVE AND SUMMARY OF RESULTS

Mixing and transport in large waste-tank volumes is controlled by the multidimensional equations describing mass, momentum and energy conservation, and by boundary conditions imposed at walls, structures, and fluid inlets and outlets. For large enclosures, careful scaling arguments show that mixing is generated by free buoyant jets arising from the injection of fluid or buoyancy into the enclosure, and by temperature and/or concentration gradients generated near surfaces by heat and mass transfer at walls, cooling tubes, and liquid-vapor interfaces. For large enclosures like waste-tank air spaces, scaling shows that these free and wall jets are generally turbulent and are generally relatively thin.

When one attempts to numerically solve the multi-dimensional mass, momentum, and energy equations with CFD codes, very fine grid resolution is required to resolve these thin jet structures, yet such fine grid resolution is difficult or impossible to provide due to computational expense. However, we have shown that the ambient fluid between jets tends to organize into either a homogeneously mixed condition or a vertically stratified condition that can be described by a one-dimensional temperature and concentration distribution. Furthermore, we can predict the transition between the well-mixed and stratified conditions. This allows us to describe mixing processes in large, complex enclosures using one-dimensional differential equations, with transport in free and wall jets modeled using standard integral techniques. With this goal in mind, we have constructed a simple, computationally efficient numerical tool, the Berkeley Mechanistic Mixing Model (BMIX), which can be used to predict the transient evolution of fuel and oxygen concentrations in DOE high-level waste tanks following loss of ventilation, and validate the model against a series of experiments. The experiments have been done with both water and air as working fluid.

Using a scaled water tank experiment, the question of the dilution of a ceiling plume of ambient air entering the waste tank at the ventilation penetrations at the top of the waste tank is addressed (see reference [2] included with this final report). The water tank experiments model flow exchange similar to the exchange between the waste tank and the ambient air by partitioning the water tank in two equal sized horizontal compartments with two penetrations. The upper compartment is filled with denser sugar or salt water and the bottom compartment is filled with pure water. When the experiment is started the unstable density potential creates an upward buoyant jet though one penetration and a downward plume in the other. Measurements of buoyant jet dilution in the bottom compartment of the water experiment is accomplished using a new measurement technique using diffraction of a sheet of laser light to measure the density profile in the bottom compartment. Also flow patterns and mixing are observed using dye introduced into the downward directed buoyant jet.

Another main result of this work has been the development of a new numerical tool, the BMIX (The Berkeley Mechanistic Mixing Model) code, for predicting species concentrations and temperature profiles in large stably stratified enclosures mixed by buoyant jets. The BMIX code has a number of attractive features, which include no artificial diffusion, high accuracy with coarse computational grids and high efficiency through a lax stability criterion which is independent of spatial grid resolution (see reference [3] included with this final report).

The first version of the BMIX code, implemtented using the very high level Matlab language, has been successfully applied to the flow exchange experiment in the water tank. The density profiles measured in the water tank experiments have been predicted with good accuracy by the BMIX code which shows the suitability of this new modeling approach and validates the BMIX code.

A next generation BMIX code is currently being developed. The new version of the BMIX code will relax unnecessary limitations in the Matlab version of the BMIX code. Most importantly the new code will treat the fluid as compressible instead of assuming incompressibility as it is done in the Matlab version. The new version of the BMIX code will be able to handle much more general enclosure setups not only related to waste tanks but more general enclosures like reactor containments and indoor environments.

The new version of the BMIX code is being developed using state-of-the-art object-oriented design (OOD) strategies. Using OOD has a number of well-proven attractive benefits including adaptability, flexibility and re-usability. This will ensure that the BMIX code is implemented in a way which makes it easy to adapt to future needs. The new BMIX code will, when completed within the next year, be validated against a number of experimental data sets including both the Berkeley data from the water tank and newly obtained data from a large cylindrical air enclosure.

Therefore, the efforts with the BMIX code promises to provide the research community in different fields with a new tool which can be applied either directly or with additions to a broad range of mixing problems. Due to its flexibility and adaptability of its object-oriented construction, the BMIX code has the potential becoming a foundation upon which many new projects can be built.

During the last year a new experimental setup was completed and measurements were obtained. The experimental setup consists of a large circular insulated enclosure with a horizontal isothermal heating plate at the bottom. A jet of cold air is injected in different directions at the top of the enclosure. This experimental setup models more closely the geometry of the waste tank gas space and provide important information on the mixing processes in the tank when the purging jets are operating. The new experiments measured the forced convection heat transfer augmentation at the isothermal plate. The newest series of experiments addressed the augmentation of the mixing processes by the array of vertical cooling tubes penetrating the waste tank gas space. In this series of experiments the cylindrical tank was refitted with a number of vertical PVC tubes simulating the distributed resistance of the cooling tubes in the real waste tank (a journal paper is under preparation, reference [4]).

RESEARCH PROGRESS DURING THE LAST YEAR

This section outlines research progress made since September 1999, in our studies of mixing processes in high-level waste tanks.

Over the last year we have made substantial progress in our research efforts, both in experiments and numerical model development.

During the completion of the research project, we recognized the importance of having our primary doctoral student working on the project, Jakob Christensen, complete the major part of his dissertation on the topic. The dissertation will insure broader dissemination of the experimental and analytical results. A second doctoral student, funded by General Electric, is working concurrently studying mixing processes in large, stratified volumes (see referece [5] included with this final report), along with a postdoctoral researcher who has focused on the experimental program. Additionally, one Masters student has completed his research project supporting the study.

Our studies focus on the mixing processes that control the distribution of fuel and oxygen in the air space of DOE high-level waste tanks, and the potential to create flammable concentrations at isolated locations, achieving all of the milestones outlined in our proposal. A major motivation for the research has come from efforts at Savannah River to use a large tank process (Tank 48) for cesium precipitation from salt solutions, which release benzene. Under normal operating conditions the potential for deflagration or detonation from these gases would be precluded by purging and ventilation systems, which remove the flammable gases and maintain a well-mixed condition in the tanks. Upon failure of the ventilation system, due to seismic or other events, however, it has proven more difficult to make strong arguments for well-mixed conditions, due to the potential for density-induced stratification which can potentially sequester fuel or oxidizer at concentrations significantly higher than average. As evidence of the importance of the issue, last year a decision was made to move away from the in-tank precipitation process. While this reduces the direct relevance of the research to SRP tank operations, important applications remain for modeling of radiolytic hydrogen mixing in large tanks, modeling of enclosure fires, and modeling of reactor containment response.

Our mixing experiments have two primary components: a series of experiments conducted in Plexiglas tanks studying scaled mixing processes in water and water/salt or water/sugar systems, and a larger experiment in a scaled SRP-tank-geometry cylindrical enclosure using heated air to study mixing under stratified conditions, driven by combined natural and forced convection heat transfer. Substantial progress was made in conducting the water experiments during the past year, and completion of the large tank experiment was also achieved.

The water experiments completed last year have addressed two issues of importance to waste tank operations, as well as more generic problems in enclosure fires. The first involved the study of exchange flows through perforated horizontal partitions. Such exchange flows, driven by buoyancy and fluctuating external pressure, are the primary mechanism bringing ambient air into waste tanks through the many openings in the tank cover, following loss of ventilation. Our experiments, described in references [1] and [2] included with final report, provided fundamental information for modeling exchange flow rates into the tank vapor space.

These experiments also allowed us to simulate the evolution of the vertical density and composition distribution in a stratified volume. The primary question here is how a dense, buoyant plume of air would mix upon entering a tank from the ceiling, and how much dilution would occur before the plume reached the tank liquid, where fuel concentrations would be the highest. The water system provided a useful analog for this process. In addition to employing standard techniques to measure the velocity of the jets entering the bottom volume of the experiment (hot film anemometry) and to visualize the buoyant jets (ink), we developed a new experimental method to measure the vertical density distribution directly, using the deflection of a sheet laser to measure the vertical distribution of the index of refraction, as described in greater detail in the appended copy of reference [2].

Construction of the air experiment in a large cylindrical insulated enclosure with a bottom horizontal isothermal heating plate is complete, and data evaluating the forced convection

augmentation of heat transfer by a purging jet on the isothermal horizontal heating plate have been collected.

The data demonstrate that the heat transfer augmentation is correlated well using the Archimedes number as the correlating dependent variable. As described in the proposal, these experimental results study the mix processes under scaled conditions more closely matching waste tank conditions.

To simulate the complex geometry of the waste tank gas space, the forced convection heat transfer augmentation was also measured in a setup where a number of vertical PVC tubes represent the distributed resistance similar to the vertical cooling tubes penetrating the waste tank volume. From the data collected for this setup it is concluded that introducing the distributed resistance has a relatively little impact on the heat transfer augmentation. More details are given in the journal paper under construction (reference [4]).

In addition to the experimental efforts, the modeling effort has demonstrated the feasibility of the one-dimensional treatment of mixing under stably stratified conditions by buoyant jets.

In the journal paper by Christensen et al [3] (a copy has been included with this final report) we describe the main features of a new Lagrangian model for mixing in large stably stratified enclosures. This new modeling approach eliminates artificial diffusion in strongly convectively dominated flows. The hyperbolic behavior of the system of PDEs which describes the conservation equations requires a numerical method with no artificial diffusion to preserve the very strong gradients that can be present. In the paper we present the rudiments of the model and discuss an important aspect of the discretization error analysis. The new BMIX code is first validated against an analytical model which has been shown to model experimental data very well. Finally, a comparison is presented against experimental data, gathered from a two enclosure exchange flow setup in a Plexiglas water tank. Both comparisons show good agreement and verify the suitability of this new modeling approach and the correctness of the BMIX code. This type of modeling approach can simulate mixing in any stably stratified large enclosure containing a multi-component fluid.

The preliminary version of the numerical tool, the BMIX code, is currently being expanded for added flexibility to accommodate more complex enclosure setups and new buoyant jet models are being added. The new version of the BMIX code is being developed in an object-oriented manner using the programming language C++. Using the object-oriented programming paradigm assures long-term usability and flexibility through re-usability, adaptability and expandability.

The new expanded BMIX code, when completed within the next year, will be able to handle a wider range of applications of the one-dimensional modeling approach for mixing in stably stratified enclosures, ranging from the complex geometrical configuration of the waste tank gas space to mixing in reactor containments and with additional modeling effort to enclosure fire modeling and general indoor air modeling of residential rooms.

The new BMIX version has the potential of becoming an important tool for a number of mixing problems in a wide range of different scientific disciplines.

FUTURE ACTIVITIES

The new state-of-the-art object-oriented version of the BMIX code will be completed during the next year and validated with both Berkeley experimental data and data from other

sources. Once validated, the new version of the BMIX code will be applied to the waste tank gas space and nuclear reactor containments. We might also try to use the BMIX code for other problems, like enclosure fires and indoor air pollutant tracking.

We are at the moment trying to establish cooperation with researchers in other disciplines who might be interested in applying the modeling provided by the BMIX code for problems in their specific areas.

INFORMATION ACCESS

Additional information about this research project can be found at:

http://www.nuc.berkeley.edu/thyd/peterson/tank.html

References:

1. P.F. Peterson and R.E. Gamble, "Scaling for Forced-Convection Augmentation of Heat and Mass Transfer in Large Enclosures by Injected Jets," *Transactions of the American Nuclear Society*, Vol. 78, pp. 265-266, 1998.

2. S.Z. Kuhn, R.D. Bernardis, C. Lee, and P.F. Peterson, "Stratification from Buoyancy-Driven Exchange Flow Through Horizontal Partitions in a Liquid Tank," accepted for publication in Nuclear Engineering and Design, 2000

3. J. Christensen and P.F. Peterson, "A One-Dimensional Lagrangian Model for Large Volume Mixing," accepted for publication in Nuclear Engineering and Design, 2000

4. S.Z. Kuhn and P.F. Peterson, "Forced-convection heat transfer augmentation for large enclosures by injected jets", Journal paper under construction.

5. R.E. Gamble, Thuy T. Nguyen, Bharat S. Shiralkar, P.F. Peterson, Ralph Greif and H. Tabata, "Pressure Suppression Pool Mixing in Passive Advanced BWR Plants", Accepted for publication in Nuclear Engineering and Design, 2000

Ninth International Topical Meeting on Nuclear Reactor Thermal Hydraulics (NURETH-9)
San Francisco, California, October 3 - 8, 1999.

DENSITY STRATIFICATION FROM BUOYANCY-DRIVEN EXCHANGE FLOW THROUGH HORIZONTAL PARTITIONS IN A LIQUID TANK

S.Z. Kuhn, R.D. Bernardis, C.H. Lee, and P.F. Peterson
University of California
Berkeley, CA 94720-1730
kuhn@nuc.berkeley.edu peterson@nuc.berkeley.edu

KEY WORDS

Stratification, Plumes, Exchange Flows, Density Distributions, Sheet Lasers

ABSTRACT

This paper presents experimental study of the transient density stratification from buoyancy-driven and forced-convection flows through horizontal partitions in a liquid tank. When strongly stratified, an enclosure's ambient density distributions can be considered one-dimensional, with negligible horizontal gradients except in narrow regions around buoyant jets. The vertical density distribution was measured by sheet laser light passing through the corner of the tank, using the change of light reflection index associated with the local fluid component concentration and density. The results of these experiments give important information to improve the modeling of transient stratification evolution induced by jets and plumes in large enclosures, as well as the prediction of exchange flow rates through horizontal openings between inter-connected compartments.

1. INTRODUCTION

This research provides information on the evolution of transient vertical density distributions in enclosures, to study the stratification phenomena and the mixing processes in large high-level waste storage tanks, reactor containments, compartment fires, and other applications. In the waste tank application, under normal operating conditions purging and ventilation systems remove any flammable gases generated from the liquid waste and maintain a well-mixed condition in the tanks. Upon failure of the ventilation system, the density-induced stratification can potentially sequester fuel or oxidizer at concentrations significantly higher than average, which can be important in analyzing safety for tank operation.

Much research has been done in the general area of natural convection in enclosures (i.e., Gebhart *et al.*, 1988 ; Jaluria and Cooper, 1989). Brown (1962) was among the first to study natural convection through openings in vertical and horizontal partitions between enclosures with air as the working fluid. Fire-induced flow through openings in vertical walls of an enclosure was first studied and documented by Prahl and Emmons (1975). Mathematical models of the flow were proposed by Steckler et al. (1986). Flow contraction and head losses at the openings were also modeled through the use of a flow

coefficient by invoking Bernoulli's equation. In most of the cases, the effects of variable density, turbulence, viscosity, and thermal diffusion were neglected.

Steckler *et al.* (1986) gave theoretical justification for using brine/water analogy for studying fire-induced flows in enclosures. In these experiments hot and cold air are replaced by fresh water and brine solution, respectively. When viscous and heat transfer effects are small, Steckler *et al.* (1986) showed that analogy between the two flow configurations exists, provided that Reynolds number based on vent height and velocity of the buoyant fluid, and the vent aspect ratio are the same. The brine/water analogy to study buoyancy flows through vents between enclosures has also been implemented by several researchers such as Epstein (1988) and Conover *et al.* (1995). They used the analogy to study the special case where the externally applied pressure across the vent is zero. Tan and Jaluria (1992) and Jaluria et al. (1993) have studied cases where the vent flow is governed by both pressure and density differential across the vent.

Epstein (1988) and Epstein and Kenton (1989) extended the work from a single opening to multiple openings through a horizontal partition. A density-driven exchange flow was obtained by using brine water above the partition and fresh water below the partition. The density of the brine water in the upper compartment was determined by means of a hydrometer. In these experiments, the volumetric exchange flow rate from the upper compartment to the lower compartment or vice versa was calculated as

$$Q = \frac{-V_H\left(d\rho_H / dt\right)}{\left(\rho_H - \rho_{L,0}\right) - \frac{V_H}{V_L}\left(\rho_{H,0} - \rho_H\right)} \tag{1}$$

where V_H and V_L are the volumes in the upper and the lower compartments, ρ_H is the density measured at the liquid surface by the hygrometer in the upper compartment at time *t*, and $\rho_{L,0}$ and $\rho_{H,0}$ are the densities in the lower and upper compartments at zero time. Based on the mass balance, Equation 1 is only valid for well mixed conditions in the upper and lower compartments, whereas in Epstein's experiment there existed vertical density stratification, and the separation of mixed and unmixed regions in both compartments (identified by the present experiments).

In the present experimental investigation, a Plexiglas tank with a horizontal partition in the middle was constructed to simulate the exchange flow through two openings, by filling the upper and lower compartments with salt/sugar water and pure water, respectively. Experiments were carried out to study the natural convection flow that occurs after removing plugs from the openings. The density difference dictates the buoyancy-driven down flow of the heavier fluid from the upper compartment to the lower compartment. Using liquid to represent buoyancy-driven gas exchange flow between compartments is valid, as long as molecular diffusion and viscosity are not important factors in strongly buoyancy-driven flow.

Figure 1 shows a representative density distribution in the lower compartment, with a distinct separation between unmixed and mixed stratified regions. It shows how Eq.(1) can produce errors. This is illustrated by considering the mixing processes occurring in the bottom volume. Note that the dense plume of salt/sugar water falls to the bottom of the tank, entraining the ambient fluid. At early times the highly-diluted salt/sugar water accumulates in a layer at the bottom of the tank. As the clear water is gradually entrained in the falling plume and transported to the bottom of the volume to be mixed with salt/sugar water, the interface between the diluted salt/sugar water and the clear water moves upward

with time. Before the interface reaches the level close to the openings, the densities of the upward and downward exchange flows through the partitions are those of pure water in the lower compartment and initial heavy salt/sugar water in the upper compartment. This mixing process corresponds qualitatively with the mixing and dilution that may occur in inerted waste tanks after loss of ventilation, due to exchange flows with denser outside air through openings in the tank cover.

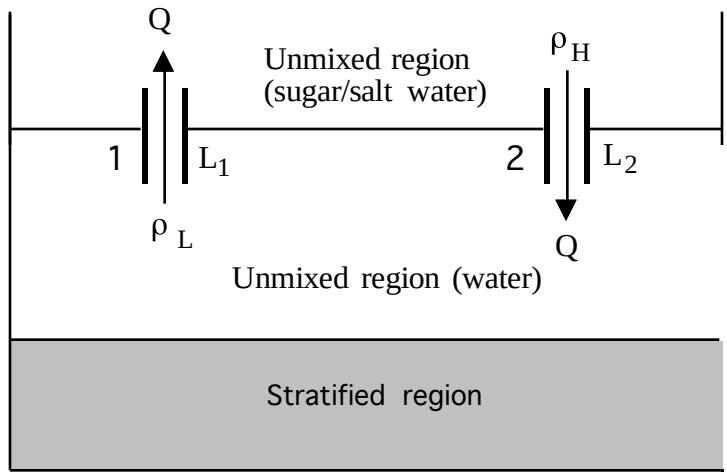

Figure 1 Density distribution by buoyancy-driven exchange flow

2. EXPERIMENTAL APPARATUS

As shown in Figure 1, the experimental apparatus consists of a Plexiglas rectangular tank fabricated with the interior region 0.578-m long, 0.289-m wide and 0.600-m high. A horizontal Plexiglas partition plate, located 0.289 m above the bottom of the tank, divided the tank into an upper compartment and a lower compartment. There were 3 set of openings on the horizontal partition, which hold chimneys with a height of 3/8" and 5/8", and an aspect ratio L/D of 1.6, 3.2, and 6.67. Figure 2 shows the configuration of the openings on the partition, and Table 1 gives the size and location of each chimney set. Two hot-film probes, used to measure the exchange flow rate, were installed below the chimneys. The hot-film probes were calibrated for each solution with different densities and temperatures.

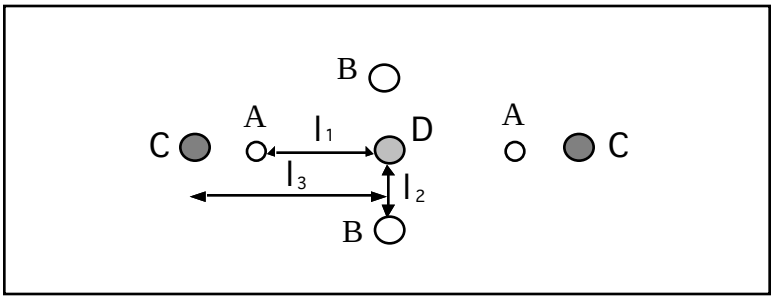

Figure 2 Configuration of openings on the horizontal partition

Table 1 Size of chimney and aspect ratio

Opening	I.D. (in)	Length L (in)	L/D	From Center (cm)
A	3/8	2.5	6.67	l_1=9.7
B	5/8	1	1.6	l_2=6.4
C	5/8	2	3.2	l_3=14.5
D	5/8	2	3.2	0

From the literature, the exchange flow within any opening of a multiple opening system can be bidirectional if the unidirectional flow established throughout the system is not high enough to capture the opposing flow in the opening. To obtain a strictly unidirectional flow pattern from the beginning, some "purging" or " flooding" velocity is required to prevent countercurrent flow within the opening. In the present experiment, the partition plate was set up to allow a very small elevation difference between the two openings to achieve unidirectional upward flow in one opening and downward flow in the other. Flow visualization demonstrated that only unidirectional flow occurred, and such a partition arrangement has negligible impact on the ambient flow stratification.

The vertical density variation was determined by implementing a light deflection technique, using the change in the index of refraction that occurs with salt and sugar concentration. A sheet laser was formed using a 20-mW helium-neon laser and optical lenses. Figure 3 illustrates the light trajectory through the corner of the tank and the reflected laser image on the grid paper. While the technique only measured the liquid density in the corner of the tank, under stratified conditions the density distributions become one-dimensional in the vertical direction with negligible horizontal gradients, except in narrow regions around the buoyant jets.

After traveling through the tank, the laser light hits a white target screen marked by grid lines with horizontal interval of 0.635 cm and vertical one of 1.3 cm, which can achieve a resolution of approximately 1/4 cm for the horizontal displacement of the laser image (see Figure 3). As density changes, the index of refraction of the stratified ambient fluid changes as well, and consequently the density curve on the target screen shifts. The density curves on the target screen were recorded by a high resolution digital camera. The deflected light curves on the target screen were calibrated at several density levels for salt water and sugar water. The higher the density, the larger the displacement of the line as shown in Figure 4. The values of the displacement for different solution were plotted as a function of the density for salt/sugar water. The data shows a linear dependence between the displacement and density, and for the same density the displacement of sugar solution is larger than that for salt solution. In the present data reduction linear functions were used to fit the data for both sugar and salt water solutions, respectively.

In addition to the laser technique, flow visualization was also performed by putting dye material into the heavier solution in the upper compartment before the testing. This, by video recording, helped identify the flow pattern through the openings (unidirectional or bidirectional, and stable or unstable), the ambient-flow stratification phenomena, and the moving interface between the mixed and unmixed regions. For unidirectional flow through two openings, flow visualization has demonstrated the horizontal spreading of the heavier solution and the formation of stratified layer in the bottom compartment. For bidirectional flow through single opening, unstable flow was identified after it leaves from the chimney opening.

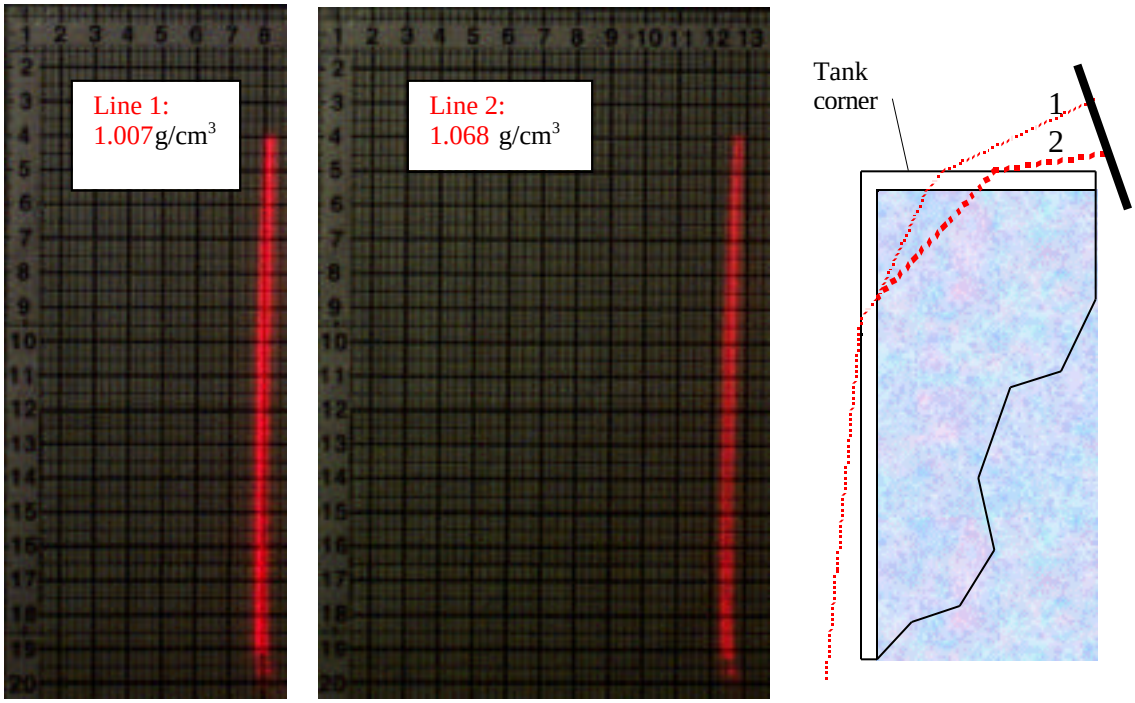

Figure 3 Dependence of index of refraction on solution density

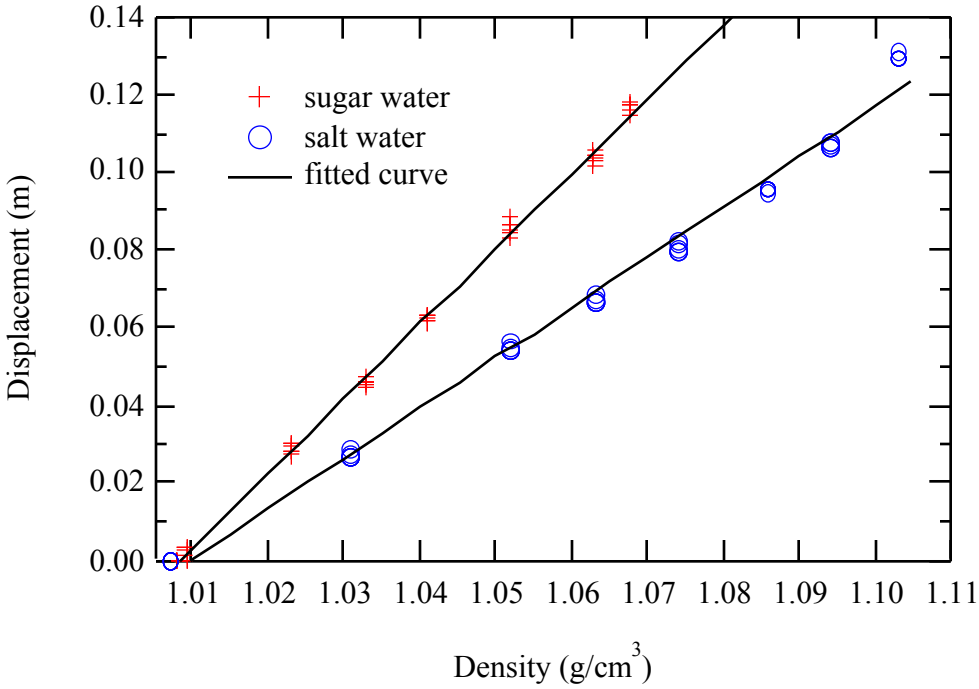

Figure 4 Calibration of displacement versus solution density

3. EXPERIMENTAL RESULTS

3.1 Test Matrix

Experiments were performed using the above technique to measure the density distribution in the lower compartment. The lower compartment was initially filled with pure water while upper compartment was filled with sugar water at density level from 1.05 and 1.109 g/cm^3, and salt water from 1.10 to 1.207 g/cm^3. Twelve experiments were carried out to study the density stratification process under buoyancy-driven unidirectional flow without dye material, another two experiments under constant injected flow, and two more experiments for the bidirectional flow through single opening D. Table 2 shows a detailed test matrix.

Table 2 Test Matrix

Solution	Initial Density (g/cm^3) / Opening	Nomenclature	Note
Sugar-Water	1.109 / A 1.076 / A 1.107 / B 1.077 / B 1.05 / C 1.086 / C	suw 1.109 / A suw 1.076 / A suw 1.107 / B suw 1.077 / B suw 1.05 / C suw 1.086/ C	unidirectional flow
Salt-Water	1.197 / A 1.105 / A 1.207 / B 1.104 / B 1.10 / C 1.19 / C	saw 1.197 / A saw 1.105 / A saw 1.207 / B saw 1.104 / B saw 1.10 / C saw 1.19 / C	unidirectional flow
Injected Salt-Water	1.16 / A	saw 1.16 / AF	fixed flow rate =7.38 cm^3/s
	1.14 / A	saw 1.14 / AF	fixed flow rate =11.19 cm^3/s
Salt-Water	1.10 / D 1.20 / D	saw 1.10 / D saw 1.20 / D	bidirectional flow through one hole

3.2 Flow Visualization

Experiments were performed with dye material for the purpose of visualizing the downward flow pattern and the formation of stratified mixing layer. With sugar water at initial density of 1.069 g/cm^3 in the upper compartment, Figure 5 shows images captured at various times from 1 to 173 sec after the start of flow. It illustrates the development of the mixing layer in the lower compartment. As the downward plume reaches the bottom, it spreads horizontally. Because the chimney is not in a symmetric position, the mixed solution reaches the right wall earlier than the left wall.

1 sec

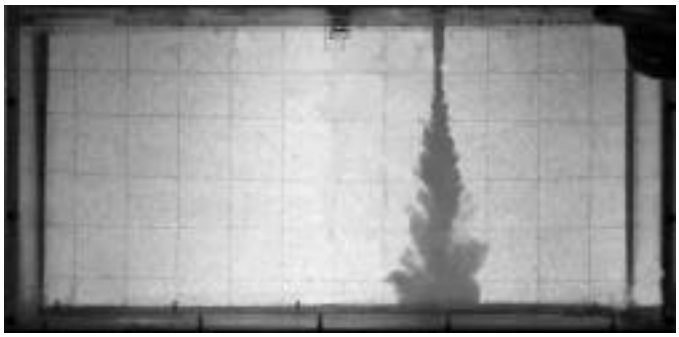

19 sec

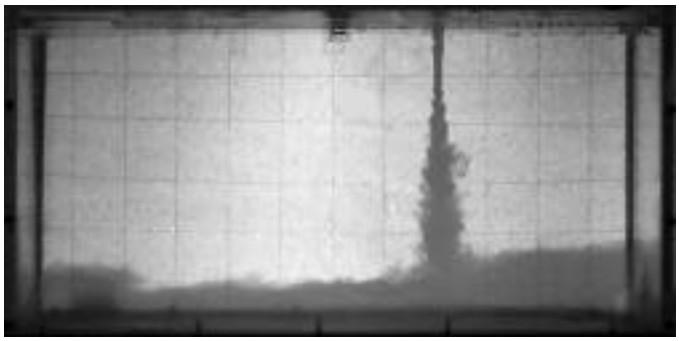

43 sec

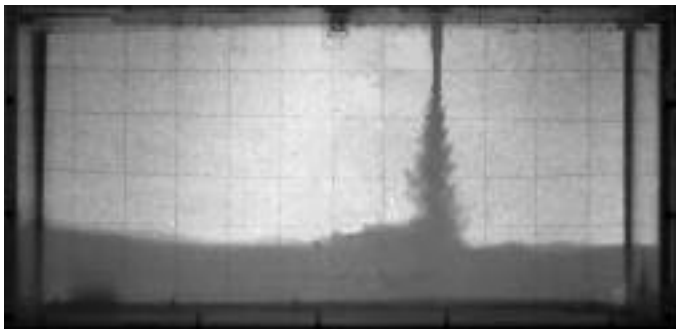

173 sec

Figure 5 Flow visualization of downward plume for sugar water at initial density of 1.069 g/cm^3 in the upper compartment.

After 9 sec more of the heavier fluid accumulates on the right side, forming a thicker layer than that on the left side. Such strong horizontal spreading causes gravity waves in the interface between the unmixed layer (transparent) and the mixed region. As the clear water is gradually entrained in the falling plume and transported to the bottom, the interface between the mixed stratified region and unmixed clear water region above moves upward with time. After 34 sec the interface became flatter, and after 173 sec a rather smooth interface was formed. It is found that the assumption of the density distributions to be considered one-dimensional does not apply to the first transient phase of the experiment due to the effects of gravity waves. It is also demonstrated by flow visualization that before the interface reaches the level close to the openings, the densities of the upward and downward exchange flows through the partitions are those of pure water in the lower compartment and initial heavy solution in the upper compartment.

Flow visualization was also performed with higher sugar water density of 1.103 g/cm^3. The increased flow rate (the initial flow rate of about 13.5 cm^3/sec compared with 11.5 cm^3/sec in previous case) causes a stronger gravity wave in the fluid near the bottom, and the interface becomes even more unstable in the initial transient phase. In this case the interface move upward faster than the previous one.

Another interesting experiment is to study bidirectional flow through a single chimney. For the tests through opening D with aspect ratio L/D of 3.2, the countercurrent flow within the chimney appeared to comprise of packets of upward water and downward sugar/salt solution with chaotic motion, identified as the "turbulent diffusion" region by Epstein (1988). It was found that flow interaction significantly reduces the flow rate, compared with that for unidirectional flow at same initial density difference. Figure 6 shows the flow pattern of downward flow from the opening. The pattern is unstable and turbulent for most cases, which causes the mixed region to be less stratified and the interface much smoother at the early stage than that in unidirectional flow with a well-formed downward plume pattern.

Figure 6 unstable bidirectional flow exiting from chimney

3.3 Stratification and Density Distribution

Using the data processed from the captured sheet laser light on screen paper, Figures 7 and 8 show the curves of density distribution in the lower compartment at different times for *suw1.086/C* and *saw1.19/C*. The density in the lower compartment increases with time, and the interface between the diluted sugar/salt water and clear water moves upward. When the interface reaches the opening of chimney, the interface stops moving, and the unmixed region of clear water above the chimney in the lower compartment remains almost the same. For the most part of the region the deflected laser light is clear on the target screen with good resolution for data processing, except the regions near the interface and tank bottom.

In Figures 7 and 8, a sharp density variation can be seen within a very thin layer near the moving interface, ranging from approximately 0.5 to 3 cm. Due to the large density variation in this region, the laser light is so dispersed that it makes the deflected light unclear between the mixed and unmixed layers on the target screen. Also illustrated by Figure 5, the image near the bottom is blurred because of the strong horizontal spreading of the plume at the initial transient phase. As the injected momentum gradually reduced with decreasing flow rate, the laser image near the bottom layer becomes more clear.

In Figure 9 , data are processed for constant injected flow rate (instead of density-driven exchange flow) for the run *saw1.16/AF*. The flow pattern of injected plume and shape of density variation are , in general, similar to *suw1.086/C* and *saw1.19/C* for natural convection. Due to constant injected flow rate, the curve shows strong stratification even after a longer period, compared with relatively flat curves in the previous cases with decreasing volume flow rate.

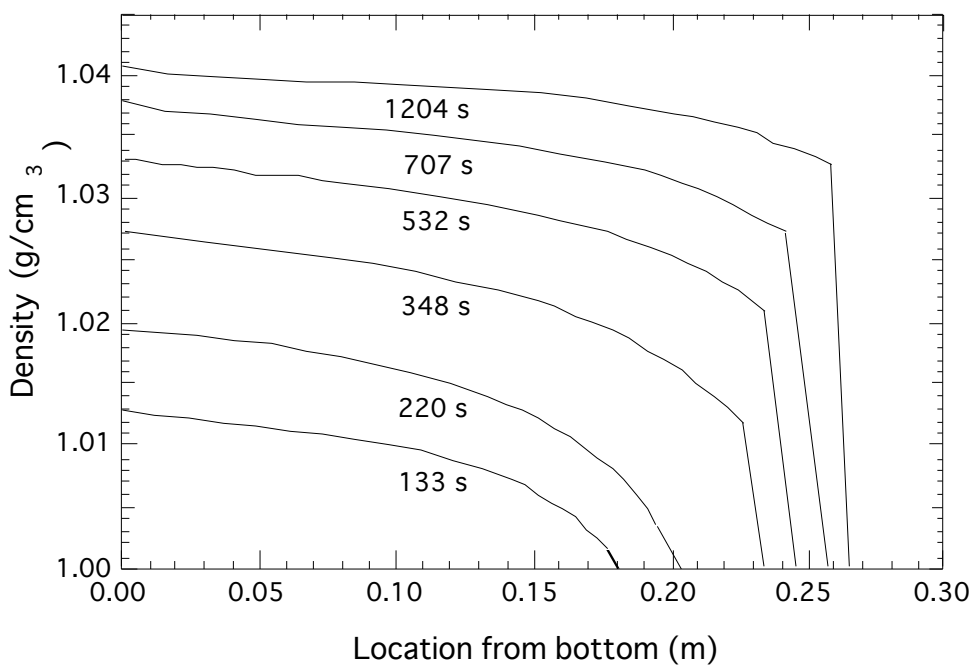

Figure 7 Density distribution for sugar water with initial condition of density 1.086 g/cm^3 in the upper compartment (run*suw1.086/C*)

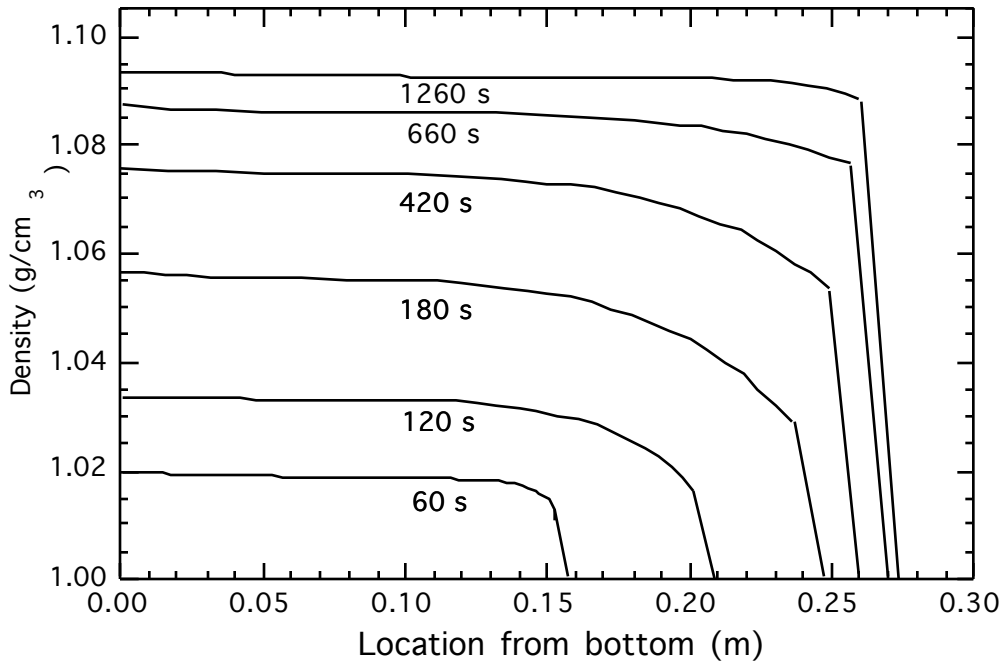

Figure 8 Density distribution for salt water with initial condition of density 1.19 g/cm^3 in the upper compartment (run *saw1.19/C*)

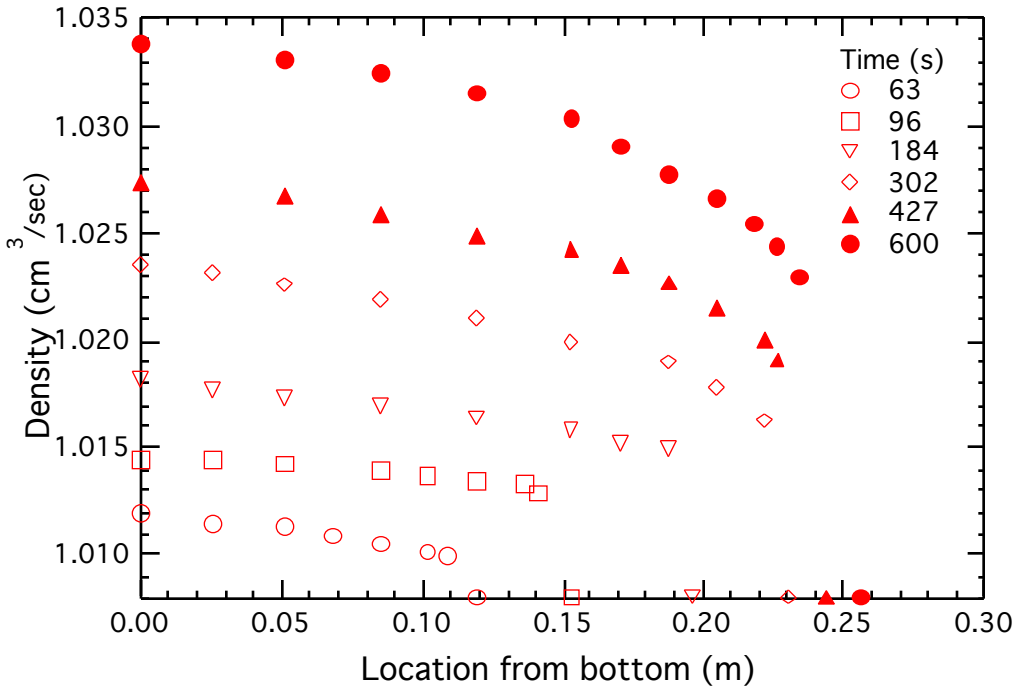

Figure 9 Density distribution under constant injected salt water at a flow rate of 11.19 cm^3/sec and density of 1.14 g/cm^3 (run *saw1.14/AF*)

3.3 Buoyancy Driven Exchange Flow through Two Openings

Prior to the interface moving to the level close to the opening as shown in Figure 5, clear water flows through the left chimney forming an upward plume whereas the heavier solution flows through the right chimney forming an downward plume. Instead of using Eq. (1), mass balances on the upper and lower compartments give

$$V_H\left(\frac{d\rho_H}{dt}\right) = -Q_u\rho_{H,0} + Q_u\rho_{L,0} \tag{2}$$

$$V_L\left(\frac{d\rho_L}{dt}\right) = -Q_u\rho_{L,0} + Q_u\rho_{H,0} \tag{3}$$

If the variation of mean density in the upper or lower compartment is known, the above equations can be an alternative to obtain the flow rate through the opening, besides using the hot-film probe for direct measurement. For the data processing in the present experiment, the first step is to calculate the mean density in the lower compartment by integrating the density curves at various times. Then the mean density can be evaluated as a function of time. Thus the exchange flow rates through the openings can be calculated by Eq. (3). The results were found to agree well with the measurement by the hot-film probes, except for the data in the initial from the early transient startup, at which time the delay for forming the stratified layer was not accounted for by the equation. Figure 10 shows the results for the unidirectional flow rate for four salt water runs through opening A and B. Flow rate with higher density difference has a higher initial startup flow rate, but also has a higher decreasing rate.

For bidirectional flow through a single opening, the above method can also be applied to evaluate the exchange flow rate, which nevertheless is totally beyond the measuring capability of the hot-film probe or other techniques.

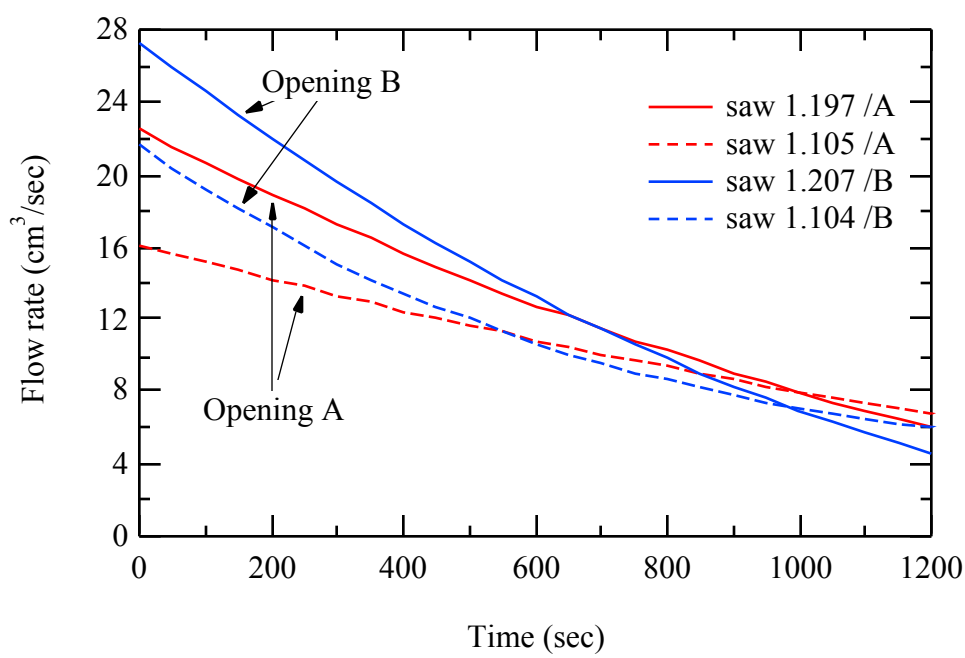

Figure 10 Exchanged flow rate for salt-water experiments

An simple expression to study the startup unidirectional flow rate through two openings can also be obtained by applying the Bernoulli equation. As illustrated in Figure 1, the equation for upward flow through opening 1 can be written by

$$P_{L,1} - P_{H,1} = \frac{1}{2}\rho_L u_1^2 + \frac{K}{2}\rho_L u_1^2 + \rho_L g L_1 \tag{4}$$

where P_L and P_H are the pressure beneath and above the chimney opening, L the axial length of openings, and K the entrance flow loss coefficient. The Bernoulli equation for downward flow through opening 2 is given by

$$P_{H,2} - P_{L,2} = \frac{1}{2}\rho_H u_2^2 + \frac{K}{2}\rho_H u_2^2 - \rho_H g L_2 \tag{5}$$

Assuming no net volumetric flow to each compartment, it gives

$$Q_u = A_1 u_1 = A_2 u_2 \tag{6}$$

where A_1 and A_2 are the flow areas of the two openings. Since both chimneys have the same length, and are at the same horizontal level, $P_{L\,1} = P_{L\,2}$ and $P_{H\,1} = P_{H,2}$. Assuming that the entrance flow loss coefficient K equals 0.5, the exchange flow rate through the openings can be obtained by combining Eqs. (4), (5), and (6), giving

$$Q_u = 1.15\left[\frac{A_1^2 g \Delta\rho L}{\rho_L + \rho_H (A_1/A_2)^2}\right]^{1/2} \tag{7}$$

A comparison of the initial startup flow rate calculated by Eq. (7) and that derived from experimental data is given in Figure 10. The calculated results agree roughly well with those from experimental data.

In the experiment by Epstein (1988) to study the buoyancy-driven exchange flow, the data were found to be 30 percent lower than the theoretical functional form of Eq. (7). The author contributed the reduction of flow rate to additional contractions and other possible loss, and replaced the coefficient 1.15 with 0.805. In the present study, we found that the theoretically derived coefficient agrees well with our experimental data for both sugar and salt water solution. Further study has found that the difference might be caused from Epstein's measuring method which did not account for density difference between the mixed and unmixed regions, and the resulting incorrect formulation used to calculate volumetric flow rate.

In all their experiments for single and multiple openings (Epstein, 1988), the mean density of the brine-filled upper compartment was measured at regular intervals. This was accomplished by resealing the opening and measuring the submergence of the hydrometer. A subsequent hydrometer reading was taken after mechanically stirring the brine solution, and this information was used to correct for any stratification in the upper compartment. It is noted that Eq. (7) is based on the assumption that the solution in both the upper and lower compartment is well mixed. Based on the present data, this theoretical formulation will overestimate the flow rate for plumes into stratified environment, if the mean density

difference $\Delta\rho$ is used in the calculation. It might explain why Epstein's data tends to be lower than the prediction by this formulation.

Furthermore, the stirring procedure only corrected the density variation in the upper compartment, while the density stratification and the separation of the mixed and unmixed regions remained in the lower compartment. If lower compartment remains stratified, upward flow through the opening is only clear water, which makes the well-mixed formulation of Eq.(1) invalid to calculate the flow rate.

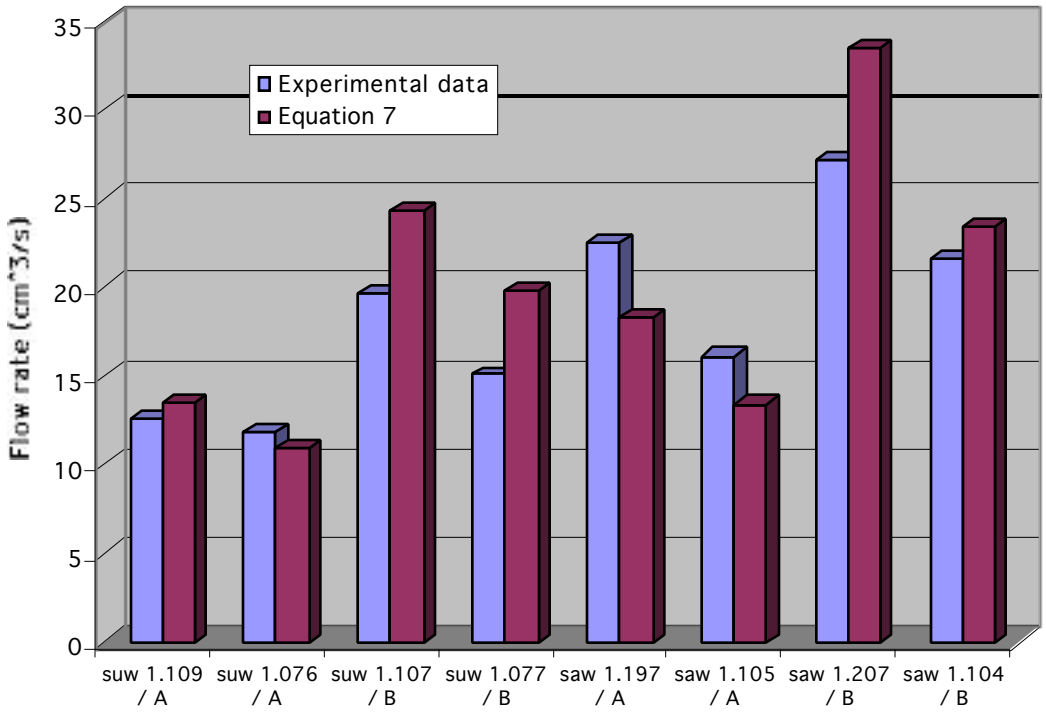

Figure 10 Comparison of initial exchange flow rates

4. CONCLUSIONS

In the past several decades, much research has been done to evaluate buoyancy-driven exchange flows through openings between interconnected compartments, which must be understood to assess the movement of toxic gases and smoke through buildings during fires, and in other applications such as reactor containment analysis. As described earlier, previous results by Epstein (1988, 1989) were not sufficient due to the method used to evaluate the exchange flow rate. The new technique using light deflection method to measure the density distribution in a scaled water-solution tank is the first of its kind to provide essential data to validate the models and empirical correlations. Reasonable agreement has been found with the comparison of the present experimental data and the numerical models by Christensen and Peterson (1999).

References

Brown, W., 1962. Natural Convection through Rectangular Openings in Partitions - Two Horizontal Partitions, *Int. Journal of Heat and Mass Transfer* 5, 869-878.

Christensen, J, and Peterson, P.F., 1999. A One-Dimensional Lagrangian Model for Large-Volume Mixing, Ninth International Topical Meeting on Nuclear Reactor Thermal Hydraulics, San Francisco, California, October 3 - 8.

Conover, T.A., Kumar, R., Kapat, J.S., 1995. Buoyant Pulsating Exchange Flow Through a Vent, *Journal of Transfer* 117, 641-648.

Epstein, M., 1988. Buoyancy-Driven Exchange Flow Through Small Openings in Horizontal Partitions, *Journal of Heat and Mass Transfer* 110, 885-893.

Epstein, M., Kenton, M.A., 1989. Combined Natural Convection and Forced Flow Through Small Openings in a Horizontal Partition, with Special Reference to Flows in Multicompartment Enclosures, *Journal of Heat and Mass Transfer* 111, 980-987.

Gebhart, B., Jaluria, Y., Mahajan, R.L., Sammakia, B., 1988. Buoyancy-Induced Flows and Transport, Hemisphere, New York.

Jaluria, Y., Cooper, L.Y., 1989. Negatively Buoyant Wall Flows Generated in Enclosure Fires, Prog. Energy Combust. Sci., Vol. 15, pp. 159-182.

Jaluria, Y., Lee, S.H., Mercier, G.P., Tan, Q., 1993. Visualization of Transport Across a Horizontal Bent Due to Density and Pressure Differences, Visualization of Heat Transfer Processes, ASME HTD Vol. 252, pp. 65-81.

Prahl,J., Emmons, H.W., 1975. Fire Induced Flow Thorough an Opening, *Combustion and Flame,* Vol. 25, pp. 369-385.

Steckler, K.D., Baum, H.R., Quintiere, J.G., 1986. Salt Water Modeling of Fire Induced Flows in a Multiroom Enclosure, 21st Symposium on Combustion, Pittsburgh, PA, pp. 143-149.

Tan, Q., Jaluria, J., 1991. Flow Through Horizontal Vents as Related to Compartment Fire Environments, NIST-GCR-92-607, Rutgers University Report to NIST, U.S. National Institute of Standards and Technology, Gaithersburg, MD.

NOMENCLATURE

A flow area of opening
D diameter of circular opening
g acceleration due to gravity
L axial length of opening
Q flow rate
t time
V_H Volume of upper compartment
V_L Volume of lower compartment
$\Delta\rho$ density difference = $\rho_H - \rho_L$
ρ density
P pressure

Subscripts

H upper compartment
L lower compartment
0 pertains to initial conditions
u unidirectional

Ninth International Topical Meeting on Nuclear Reactor Thermal Hydraulics (NURETH-9)
San Francisco, California, October 3 - 8, 1999.

A One-Dimensional Lagrangian Model for Large-Volume Mixing

Jakob Christensen and Per F. Peterson
Department of Nuclear Engineering
University of California
Berkeley, CA 94720-1730
jakobchr@jakobchr.com peterson@nuc.berkeley.edu

KEY WORDS

Containment Mixing, Stratification, Lagrangian Methods, Multi-Zone Models, Discretization Error

ABSTRACT

In this paper we describe the main features of a new Lagrangian model for mixing in large stably stratified enclosures. This new modeling approach eliminates artificial diffusion in strongly convectively dominated flows. The hyperbolic behavior of the system of PDEs requires a numerical method with no artificial diffusion to preserve the very strong gradients that can be present. We present the rudiments of the model and discuss an important aspect of the discretization error analysis. The new `BMIX` code is first validated against an analytical model which has been shown to model experimental data very well. Finally, a comparison is presented against experimental data, gathered from a two enclosure exchange flow setup. Both comparisons show good agreement and verify the suitability of this new modeling approach and the correctness of the `BMIX` code. The computer code can simulate mixing in any stably stratified large enclosure containing a multi-component fluid provided it is nearly incompressible.

1 INTRODUCTION

Mixing processes in large enclosures under stably stratified conditions are important in many applications. From smaller rooms in houses and high-rises experiencing heating and natural ventilation to mixing processes in the ocean due to discharge of both natural and man-made sources, mixing under stratified conditions can be the primary mechanism by which the time-wise evolution of the fluid state is controlled. In between these two length-scale extremes of the "enclosure" size we find other important applications such as multi-compartment modeling of fires in complex building structures, mixing in waste tanks containing liquid high-level radioactive waste, and modeling the long term response of the reactor containment and suppression pool of a nuclear power station under accident conditions.

In the past, stratification in large volumes has been modeled by either lumped or 2-zone models. Both models, and the lumped model in particular, fail to model the physics of the mixing processes. In the lumped model the fundamental assumption is that the volume is homogeneously mixed, which can introduce substantial error when large gradients exist in the stratified ambient. Introducing several artificial control volumes within the large lumped volume has been attempted, but this introduces flows between control volumes which are non-physical (Murata and Stamps [1996]).

Somewhat better agreement can be attained by the 2-zone models (Peacock et al. [1993]), however, they also fail to model the detailed physics of the mixing processes. In many situations, dependent on the complexity of plumes and openings in the enclosure, the flow field is not well described as two distinct, uniformly mixed layers, but may instead only have a distinct non-uniform distribution of species and energy. This is typically seen in the long term behavior in stratification experiments (see Section 5, for instance).

This paper is divided into four main sections (introduction and conclusion excluded) which, in chronological order, describe the `BMIX` code, compares the numerically evaluated first front for an experiment with one thermal plume to an exact analytical solution, validates the numerical temperature profiles against an approximate analytical model and finally compares numerical results to a series of experimental data from a two compartment flow exchange experiment.

2 DESCRIPTION OF THE `BMIX`[1] CODE

The modeling of mixing and stratification in a large stratified enclosure consists of two main parts. These two parts arise naturally by considering conservation equations for the fluid contained within the buoyant jets and the fluid in the ambient volume (the volume outside the buoyant jets). The conservation equations for the buoyant jets couple to the ambient conservation equations because fluid is exchanged between the two.

Peterson [1994] provides the derivation of the 1-D Eulerian conservation equations for the ambient and lists the underlying assumptions.

The 1-D approximation assumes that the buoyant jets occupy a small fraction of the total volume and the momentum injected into the enclosure is below a threshold value where the enclosure stratifies in a stable manner (homogeneous mixing prevented). With these assumptions a detailed analysis of the buoyant jets becomes unnecessary and they can be treated as quasi-steady with transport within them being instantaneous. Therefore, to model the buoyant jets integral solutions describing the entrainment rate are sufficient.

The 1-D Eulerian conservation equations for an incompressible multi-component fluid ($\rho = \mathrm{const}$) can then be written, using the Boussinesq approximation, as (total mass, momentum, energy and species mass)

$$\frac{\partial Q_{\mathrm{sf}}}{\partial z} = \sum_{\ell=1}^{L} Q'_{\mathrm{entr},\ell} \tag{1}$$

$$\frac{\partial p}{\partial z} = -\rho g \tag{2}$$

$$A_c \frac{\partial h}{\partial t} + \frac{\partial}{\partial z}\left\{ h Q_{\mathrm{sf}} - \frac{A_c}{\rho} k \frac{\partial T_{\mathrm{sf}}}{\partial z} \right\} = \sum_{\ell=1}^{L} (h Q'_{\mathrm{entr}})_\ell \tag{3}$$

$$A_c \frac{\partial \chi_i}{\partial t} + \frac{\partial}{\partial z}\left\{ \chi_i Q_{\mathrm{sf}} - A_c \mathcal{D} \frac{\partial \chi_i}{\partial z} \right\} = \sum_{\ell=1}^{L} (\chi_i Q'_{\mathrm{entr}})_\ell \qquad \text{for } i = \{1, 2, \ldots, (I-1)\} \tag{4}$$

[1]Further information on the `BMIX` code can be found on-line at: `http://www.jakobchr.com`

where

A_c	is the horizontal cross-sectional area of the enclosure $[\mathrm{m}^2]$ at elevation z,
ρ	the total density of the stratified ambient fluid [kg/m^3] defined by $$\rho \triangleq \sum_{i=1}^{I} \rho_i,$$
Q_{sf}	the volumetric flow rate (in z-direction) of the stratified ambient fluid [m^3/s],
Q'_{entr}	the volumetric flow rate per unit length of fluid entrained[2] by a buoyant jet [m^2/s],
L	the number of buoyant jets in the enclosure [—],
p	the pressure [Pa],
g	the gravitational acceleration [m/s^2],
h	the mixture specific enthalpy [J/kg],
T_{sf}	the temperature of the stratified ambient fluid [K],
k	the thermal conductivity of the mixture [W/(m·K)],
χ_i	the mass fraction of species i [—], and
$\mathcal{D}$	the mass diffusion coefficient [m^2/s].

The conservation equations given by (1)-(4) serve as the starting point for the numerical method presented in this paper.

Under stably stratified conditions the solution to the conservation equations can exhibit strong gradients (what are later described as "fronts") that have to be preserved when solving the discrete counterpart to the continuous conservation equations. The Eulerian conservation equations consist of a set of convection-diffusion partial differential equations (PDEs), or in mathematical terms hyperbolic-parabolic PDEs. In many practical cases the flow field is convectively dominated (strongly hyperbolic) but diffusion may become important for very weak buoyant jets. Here the term "jet" implies a pure source of momentum (neutral buoyancy) and "plume" a pure source of buoyancy (ideally zero momentum) and, therefore, a buoyant jet can be anything in between the two extremes.

Numerical methods traditionally used to solve the conservation equations in general have great difficulty in preserving strong gradients in hyperbolicly dominated flows. The traditional discretization procedures inherently introduce extra ("false") diffusion terms which do not exist in the original differential equation. Typically these extra diffusion terms put severe limitations on the maximal size of the computational cell ($\Delta t \cdot \Delta z$) for the computed solution to be reasonably accurate.

Therefore, we present an alternative to the traditional numerical methods that

- eliminates "false diffusion" from the discretized equations,

[2]Note that in these equations, at the discharge elevation of the buoyant jets the entrainment is negative representing a source of fluid.

- gives physically acceptable solutions even for coarse computational grids,
- has favorable stability requirements, i.e. a very lax stability requirement,
- and requires low computational cost.

A Lagrangian approach was adopted to eliminate numerical diffusion. The Lagrangian formulation tracks the position of constant mass fluid "layers". In practice, we divide the enclosure into a user-specified number of horizontal control volumes and the conservation equations, without the diffusion terms, are then used to calculate the new positions, compositions and enthalpies of the control volumes for each time step. We refer to this step as the pure Lagrangian step. Next we correct the composition and energy according to the diffusion terms in the conservation equations.

Choosing a Lagrangian method also has its costs mostly due to a more complicated implementation, because we have to track the position of every control volume. If high accuracy is desired it is necessary to track their position even within a time step. In general, having a moving computational grid implies more bookkeeping and makes the implementation of virtually all aspects of the code less automatic compared to a standard finite difference method (FDM).

One example of the complication is the necessity of grid management. At each time step L new control volumes are created and so both the number of control volumes and the computational cost increase linearly with time. For a production type of code this is clearly not feasible and some kind of truncation error based intelligent grid management is necessary. However, due to the nature of the computations done in this paper we have, for accuracy reasons, not employed any form for grid management.

The discrete Lagrangian conservation equations (mass, species mass, and energy) are given below[3]

$$V_k^{j+1} - V_k^j = \Delta t \left\{ -\sum_{\ell=1}^{L} Q_{k,\ell}^j + A_{k+1}^j \sum_{i=1}^{I} \dot{V}''^{j}_{i,k+1} - A_k^j \sum_{i=1}^{I} \dot{V}''^{j}_{i,k} + S_k^j - \hat{S}_k^j \right\} \tag{5}$$

$$\begin{aligned} \overline{\chi}_{i,k}^{j+1} V_k^{j+1} - \overline{\chi}_{i,k}^j V_k^j \quad = \quad & \Delta t \left\{ -\overline{\chi}_{i,k}^j \sum_{\ell=1}^{P} Q_{k,\ell}^j + A_{k+1}^j \dot{V}''^{j}_{i,k+1} - A_k^j \dot{V}''^{j}_{i,k} \right. \\ & \left. + S_{i,k}^j - \hat{S}_{i,k}^j \right\} \quad \text{for } i = \{1, 2, \ldots, (I-1)\} \end{aligned} \tag{6}$$

[3]Since we are considering the incompressible case the pressure distribution can be obtained independently from the other flow state variables and simply consists of the hydrostatic head.

$$
\begin{aligned}
\overline{h}^{j+1}_{k,\text{mix}} V^{j+1}_k - \overline{h}^{j}_{k,\text{mix}} V^{j}_k \quad = \quad & \Delta t \Bigg\{ - \sum_{i=1}^{I} \overline{h}^{j}_{i,k} \overline{\chi}^{j}_{i,k} \sum_{\ell=1}^{P} Q^{j}_{k,\ell} \\
& + A^{j}_{k+1} \sum_{i=1}^{I} \overline{h}^{j}_{i,a_{i,k+1}} \dot{V}''^{j}_{i,k+1} - A^{j}_{k} \sum_{i=1}^{I} \overline{h}^{j}_{i,a_{i,k}} \dot{V}''^{j}_{i,k} \\
& + \frac{1}{\overline{\rho}} \left(A^{j}_{k+1} q''^{j}_{k+1} - A^{j}_{k} q''^{j}_{k} + S^{j}_{h,k} - \hat{S}^{j}_{h,k} \right) \Bigg\}
\end{aligned} \tag{7}
$$

where the superscripts indicate the time level ($t = j\Delta t$), the subscript 'i' corresponds to the ith component of the fluid, subscript 'k' indicates the kth control volume, and subscript 'ℓ' the ℓth buoyant jet. Furthermore, we have that

V	Volume [m^3].
Δt	Time steplength [s].
L	Number of buoyant jets present in the enclosure [—].
$Q_{k,\ell}$	Volumetric flow rate entrained by buoyant jet ℓ within control volume k [m^3/s].
A	Horizontal cross-sectional area [m^2].
$\dot{V}''$	Volumetric flow rate per unit area due to molecular diffusion [m^3/(m$^2\cdot$ s)].
S,$\hat{S}$	Volume source and sink, respectively [m^3/s].
$\overline{\chi}$	Volume averaged mass fraction [—].
$\overline{h}_{\text{mix}}$	Volume averaged mixture enthalpy [J/kg].
$\overline{\rho}$	Volume averaged total density [kg/m^3].
q''	Heat flux due to heat diffusion [W/m^2].
S_h,$\hat{S}_h$	Source and sink respectively of energy per unit time [W].
Δz	Steplength in the z-direction [m].

The subscript $a_{i,k}$ used in the energy equation, Eq. (7), accounts for the direction of the diffusive mass flux and is defined by

$$
a_{i,k} \triangleq \begin{cases} k & , \quad \left.\frac{\partial \chi_i}{\partial z}\right|_{z=z_k} > 0 \\ k-1 & , \quad \left.\frac{\partial \chi_i}{\partial z}\right|_{z=z_k} \leq 0 \end{cases} \tag{8}
$$

The stability for this set of difference equations is guaranteed provided negative control volumes do not occur at any time (the non-negative requirement). In practice this requirement can be stated as (neglecting mass diffusion)

$$
\Delta t^{j}_{\max} = \min_{k=\{1,2,\ldots,K\}} V^{j}_{k} \left[\sum_{\ell=1}^{L} Q^{j}_{k,\ell} \right]^{-1} \geq \min_{z \in [z_{\text{bot}}; z_{\text{top}}]} A_c(z) \left[\sum_{\ell=1}^{L} Q'_{\text{entr},\ell}{}^{j}(z) \right]^{-1} \tag{9}
$$

From the last expression we identify a very important feature of this proposed Lagrangian numerical method. Using the last slightly tighter stability bound, the maximum allowable time steplength is *independent* on spatial discretization (i.e. δz). In practice we will see a slight dependence on spatial discretization because in effect both the cross-sectional area and entrainment rate are averaged over the finite spatial steplength, but the dependence is negligible except for extremely coarse grids.

Contrast this stability requirement with the Courant-Friedrichs-Levy (CFL) stability criterion encountered for standard finite difference methods. The CFL-condition bounds the ratio $\Delta t/\Delta z$ which means that $\Delta t_{\max}$ is determined by the smallest spatial computational cell (Δz) in the computational domain and increasing spatial resolution (smaller Δz) requires a smaller time steplength. For our proposed Lagrangian method Δz can be chosen independently of Δt.

The stability criterion is so lax that in practice Δt is not limited by (9). Instead the maximum tolerable time steplength is limited by accuracy, i.e. the size of the truncation error limits the time steplength.

3 COMPARISON WITH ANALYTICAL SOLUTION OF THE LOCATION OF THE FIRST FRONT

The `BMIX` code is first validated against a simple analytical solution. The basis of the analytical solution is the plume model by Morton et al. [1956] who made the fundamental assumption that the entrainment velocity v_r is a fraction, α [—], of the buoyant jet average velocity $\overline{w}$. The Morton plume model can treat vertical buoyant jets generated by both thermal expansion and vertically injected fluid (the direction of injection has to match the sign of the buoyancy).

Formally, we may write the volumetric flow rate[4] of the buoyant jet, Q_{p} [m^3/s], as

$$Q_{\mathrm{p}} \triangleq 2\pi \int_0^\infty wr\, dr = \pi \overline{w} b^2 \tag{10}$$

where $\overline{w}$ [m/s] is the average velocity in the z-direction and b [m] the radius of the axisymmetric buoyant jet. In Figure 1 we have depicted the behavior of the axisymmetric buoyant jet as it develops along the direction of flow (z-axis).

From Baines and Turner [1969] we have that

$$b = \frac{6}{5}\alpha z \tag{11}$$

and

$$\overline{w} = \frac{5}{6\alpha}\left(\frac{18}{5\pi}\alpha B\right)^{1/3} z^{-1/3} \tag{12}$$

[4]Note that the flow rate of the buoyant jet is here defined as the flow of ambient fluid which has been entrained and does not account for any flow the buoyant jet may have at the inlet.

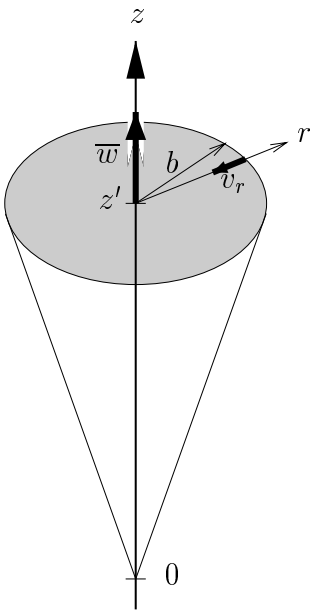

Figure 1 Axisymmetric buoyant jet as it is assumed in the model by Morton et al.

where B [m^4/s^3] is the buoyancy flux (the buoyancy flux is defined by Eq. (19) for a heat source and Eq. (49) for injected fluid), z [m] is the elevation *from the source* and the entrainment constant, α [—], is defined as the fraction of entrainment (inward) velocity to the average velocity $\overline{w}$. In mathematical terms we can write

$$v_r = -\alpha|\overline{w}| \tag{13}$$

where v_r [m/s] is the radial velocity using a cylindrical polar coordinate system (the absolute value of $\overline{w}$ allows for both upward and downward directed buoyant jets). The entrainment constant, α, is empirically determined.

Combining Eqs. (10)-(12) reveals the following expression for the buoyant jet volumetric flow rate

$$Q_{\mathrm{p}} = \frac{6\pi}{5}\alpha^{4/3}\left(\frac{18}{5\pi}\right)^{1/3} B^{1/3} z^{5/3} \tag{14}$$

Another definition of the entrainment constant often occurs in the plume literature. Here the volumetric flow rate carried by a buoyant jet, Q_{p} [m^3/s], is defined as (Peterson [1994])

$$Q_{\mathrm{p}} = k_\mu B^{1/3} z^{5/3} \tag{15}$$

giving a volumetric entrainment rate per unit length, Q'_{entr} [m^2/s],

$$Q'_{\mathrm{entr}} \equiv \frac{d}{dz}Q_{\mathrm{p}} = \frac{5}{3}k_\mu B^{1/3} z^{2/3} \tag{16}$$

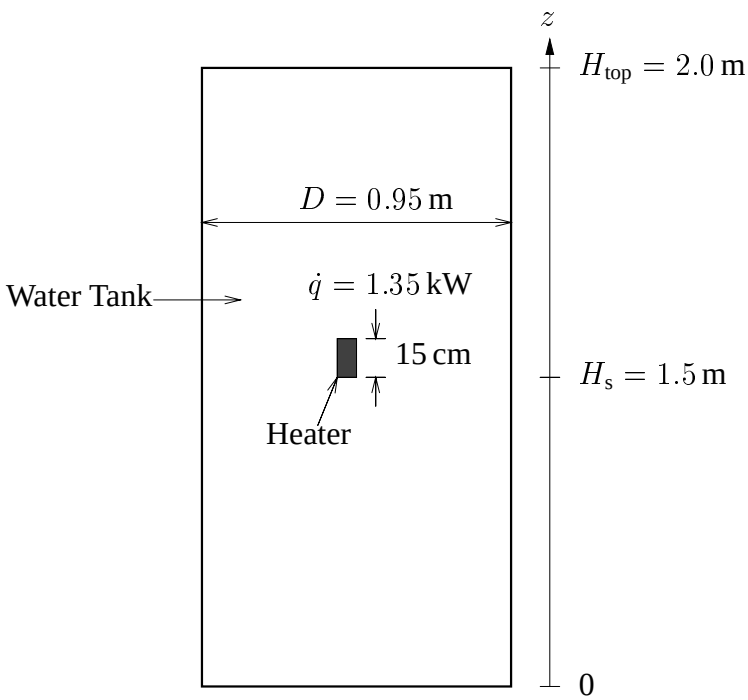

Figure 2 Thermal stratification experiment in cylindrical water tank.

where k_μ [—] is Taylor's entrainment constant.

Comparing the two expressions for the volumetric flow rate of the buoyant jet, Eqs. (15) and (14), we obtain the following equation for the relationship between the two entrainment constants α and k_μ:

$$\alpha = \left[\frac{5}{6\pi}\left(\frac{18}{5\pi}\right)^{-1/3} k_\mu\right]^{3/4} \simeq 0.3572 k_\mu^{3/4} \tag{17}$$

This expression relating the two entrainment constants, α and k_μ, is useful as we use both in this paper.

3.1 Description of analytical test case

The analytical test case matches an earlier experiment (Peterson [1994]) that submerged an electrical heater into a cylindrical tank. The heat produces an upward directed vertical plume which penetrates all the way to the water surface at the top of the cylindrical tank. After the plume reaches the top of the tank it spreads out and forms a layer which is warmer than the fluid below. The transient evolution of the vertical temperature distribution was measured using a number of thermo-couples. Figure 2 illustrates the geometry of the experiment.

For the comparison against the analytical solution $H_{\text{s}} = 0.5\,\text{m}$ (i.e. $1.5\,\text{m}$ depth) is used so that the front of heated water takes longer to get close to the heater. Furthermore, an ideal buoyancy source at elevation H_{s} was assumed. This is in general a poor assumption

(Baines and Turner [1969]) which must be corrected for when comparing against experimental data[5]. For the experiment

$$\begin{aligned} A_c &= \frac{\pi}{4}D^2 = 0.709\,\mathrm{m}^2 \\ H_{\text{eff}} &= H_{\text{top}} - H_{\text{s}} = 1.5\,\mathrm{m} \end{aligned} \tag{18}$$

where A_c [m^2] is the cross-sectional area of the tank and H_{eff} [m] is the *effective* height defined as the difference between the discharge elevation and the source elevation.

Furthermore, the buoyancy flux, B [m^4/s^3], for a heat source can be calculated as (corresponding to water at 20°C)

$$B = \frac{g\beta\dot{q}}{\rho_{\text{av}}c_p} = 6.7 \cdot 10^{-7}\,\frac{\mathrm{m}^4}{\mathrm{s}^3} \tag{19}$$

where

g	gravitational acceleration [m/s^2].
β	constant of thermal expansion [1/K].
$\dot{q}$	heat addition rate [W].
ρ_{av}	total density of the ambient fluid [kg/m^3].
c_p	specific heat at constant pressure [J/(kg · K)].

3.2 Numerical results, validation and error analysis

In order to carry out a simulation of the water tank setup we have to specify the entrainment constant α (or k_μ). In previous modeling at Berkeley the entrainment constant was chosen as (Peterson [1994])

$$k_\mu = 0.15 \tag{20}$$

Now in order to calculate the propagation of the first front analytically by expressions given by Baines and Turner [1969] we have to calculate the entrainment constant α. Using Eq. (17) we obtain

$$\alpha \simeq 0.0861 \tag{21}$$

The position of the first front, z_{k_0} [m], is defined as the elevation *relative to the source* where heating first occurs. The exact analytical expression for the location of the

[5]The heater used in this experimental setup is 15 cm long which has to be compared to an active height of the enclosure of 50 cm. Therefore, it would seem likely that the numerical calculation has to be corrected for the imperfect source. In fact it would be very likely that the numerical results will be very sensitive to the placement of what we could call the *virtual ideal source.*

first front, z_{k_0} [m], can be written as (Baines and Turner [1969], Worster and Huppert [1983])

$$z_{k_0} = H_{\text{eff}} \left[1 + \frac{1}{5} \left(\frac{18}{5} \right)^{1/3} \tau \right]^{-3/2} \tag{22}$$

where τ [—] is a dimensionless time defined by

$$\tau \triangleq 4\pi^{2/3} \alpha^{4/3} H_{\text{eff}}^{2/3} A_c^{-1} B^{1/3} t \tag{23}$$

Using the data for the experimental setup given in Section 3.1 we obtain

$$z_{k_0} = 1.5\,\text{m} \left[1 + 0.30652 \frac{t}{189.977\,\text{s}} \right]^{-3/2} \tag{24}$$

Figure 3 compares the position of the first front calculated by the numerical simulation to the analytical expression, Eq. (24).

The numerical solution used a time steplength of $\Delta t = 0.5\,\text{s}$ and set the thermal diffusion to zero as it is assumed in Baines and Turner [1969] and Worster and Huppert [1983]. We used a single control volume as the initial[6] computational grid and to preserve maximum accuracy no grid management was employed, i.e. all control volumes created were tracked to the end of the simulation (merging of control volumes was disabled).

Since there is no apparent difference in Figure 3 between the two values of z_{k_0} we have also depicted the difference, or error, $E_{z_{k_0}}$ [m], in Figure 4.

Understanding the origin of the discretization error associated with any numerical method is important because it both enables an assessment of the accuracy of the numerical results and, perhaps more importantly, is a prerequisite for adaptive grid management, i.e. adjustment of mesh sizes according to the solution. In our case we want to select the maximum time steplength which satisfies some user specified accuracy requirement. Based on accurate information on the discretization error this kind of grid management strategy ensures optimal usage of CPU time and, hence, renders the fastest and most efficient numerical method.

Most of the discretization error in our Lagrangian method arises from the fact that the first front CV during one time step. Since the entrainment calculation assumes that the CV is at a fixed position during the time step we are making an error which depends on

1. The distance, s_{k_0} [m], that the first front CV travels during one time step.
2. The functional form of the entrainment vs. elevation, i.e. $Q'_\ell(z)$.

[6] As we show later (see Section 4) one control volume is sufficient when discretizing the initially homogeneous enclosure.

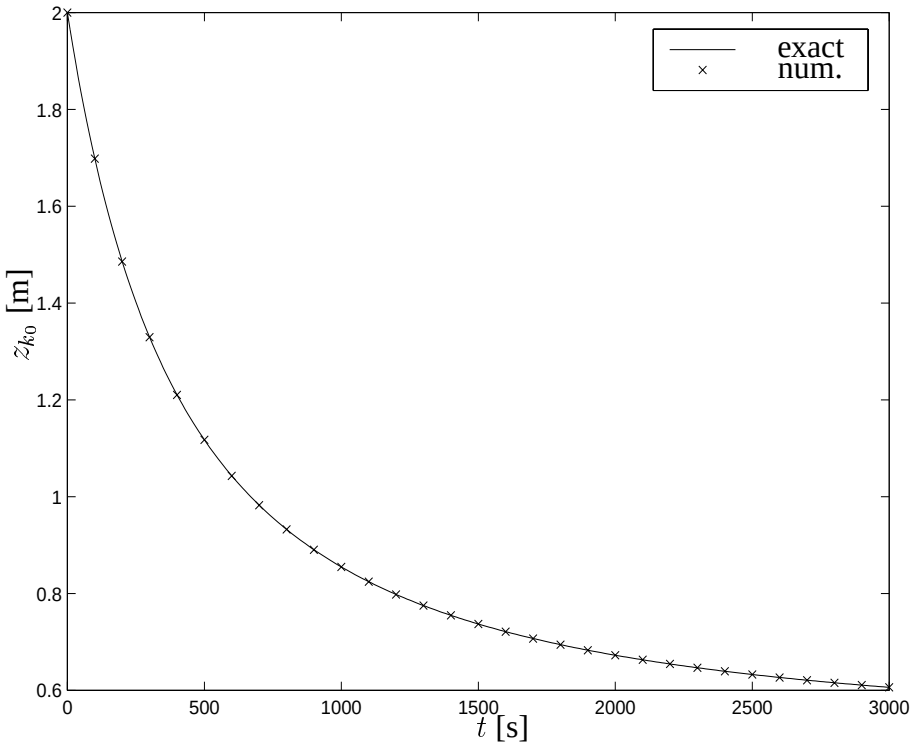

Figure 3 Comparison of the numerically and analytically calculated location of the first front.

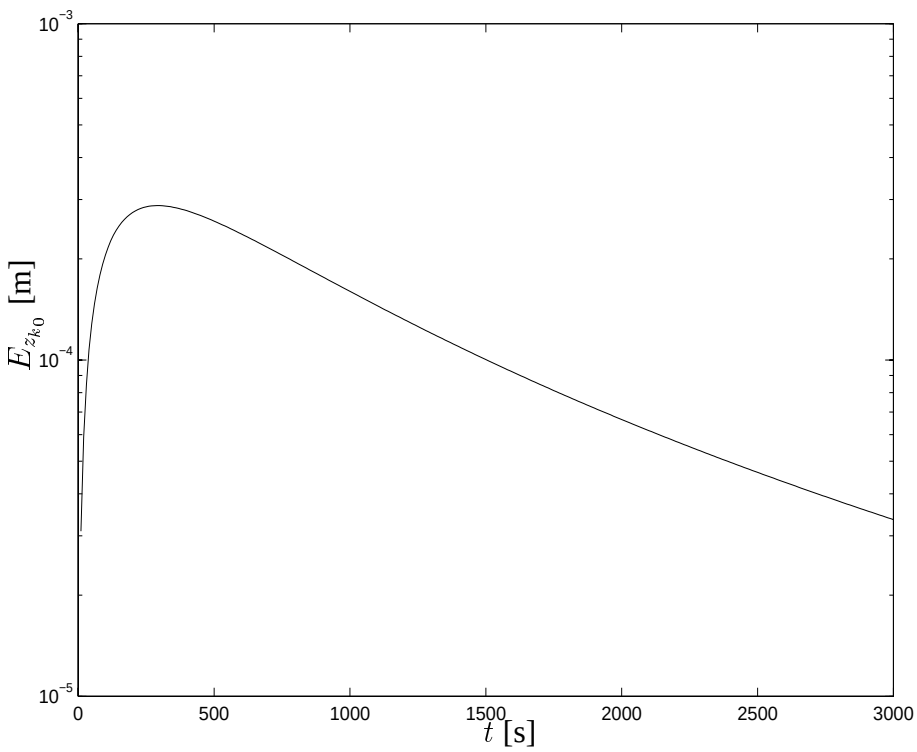

Figure 4 Error in the numerically calculated first front position.

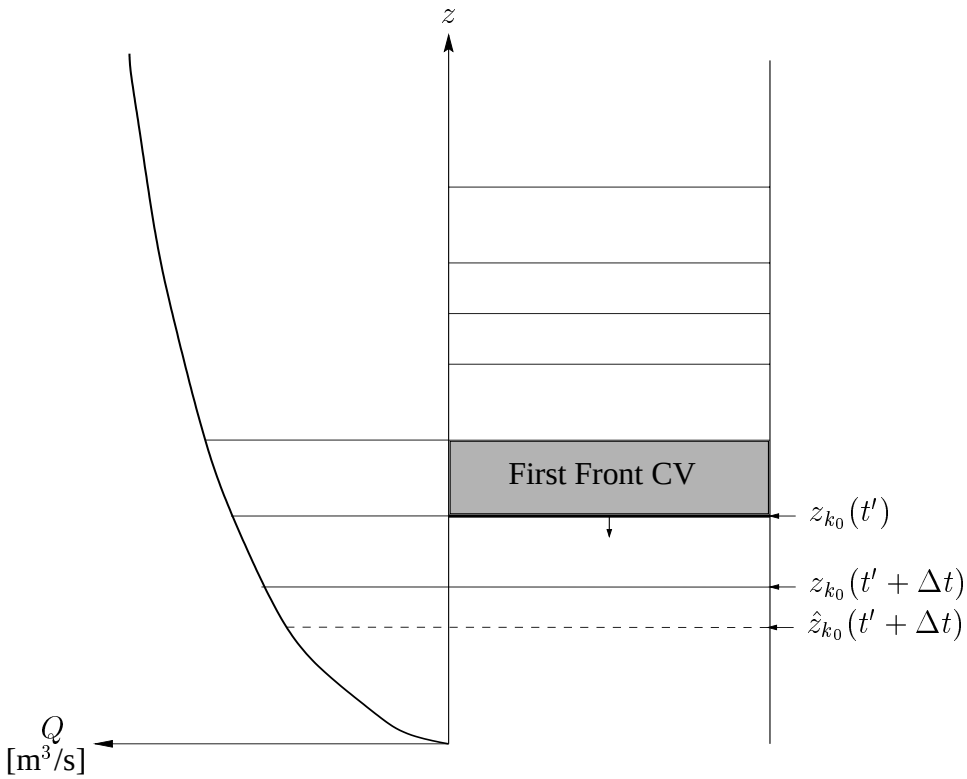

Figure 5 Error arising from the movement of the first front during one time step.

The origin of the discretization error is easily grasped when looking at Figure 5 which shows the first front as it moves during one time step. We have depicted both the exact value of the first front position, $z_{k_0}(t' + \Delta t)$, and the numerically calculated first front location, $\hat{z}_{k_0}(t' + \Delta t)$, at the end of the time step. The way the entrainment computation is set up we always overpredict the total entrained volume, i.e. the numerically calculated first front position will be at a lower elevation compared to the exact location.

The movement of the first front is controlled by the total entrainment below it. The velocity at the first front (identical to the velocity *of* the first front), w_{k_0} [m/s], is given by

$$w_{k_0} = -\frac{1}{A_c} Q_{\text{entr}}(z_{k_0}) \tag{25}$$

The exact total entrained volume below the first front during one time step (from t' to $t' + \Delta t$), $V_{\text{entr,tot}}$ [m^3], is given by

$$V_{\text{entr,tot}} = \int_{t'}^{t'+\Delta t} Q_{\text{entr}}(z_{k_0}(\tilde{t}))d\tilde{t} \tag{26}$$

In the BMIX code we assume the first front does not move within one time step, i.e. we approximate $V_{\mathrm{entr,tot}}$ by

$$V_{\mathrm{entr,tot}} \simeq Q_{\mathrm{entr}}(z_{k_0}(t'))\Delta t \equiv \Delta t \int_{z_{\mathrm{bot}}}^{z_{k_0}(t')} Q'_{\mathrm{entr}}(z)\, dz \tag{27}$$

In this test case we can calculate $V_{\mathrm{entr,tot}}$ exactly using the functional forms of Q_{entr} and z_{k_0}. Using Eqs. (24) and (15) we obtain

$$V_{\mathrm{entr,tot}} = k_\mu B^{1/3}(1.5\,\mathrm{m})^{5/3} \int_{t'}^{t'+\Delta t} \left[1 + 0.30652\frac{t}{189.977\,\mathrm{s}}\right]^{-5/2} dt \tag{28}$$

Evaluating the integral and combining the constants in front of the integral yields

$$V_{\mathrm{entr,tot}} = -H_{\mathrm{eff}} A_c \left[\left[1 + 0.30652\frac{t}{189.977\,\mathrm{s}}\right]^{-3/2}\right]_{t'}^{t'+\Delta t} \tag{29}$$

which makes sense because for $t' = 0\,\mathrm{s}$ and $\Delta t \to \infty$ we entrain all liquid ($A_c H_{\mathrm{eff}}$), i.e. for $t \to \infty$ the front is at the source.

To verify the expression for the exact entrainment below the first front we conducted a numerical experiment with an initial grid of one control volume. Since the upper boundary of this CV will coincide with the first front we correct the entrainment below the first front by applying Eq. (29) to the first CV.

We carried out this numerical experiment with a time steplength of $\Delta t = 100\,\mathrm{s}$ which would normally give a maximum error in the position of the first front of order 10^{-1} m. The error with the corrected entrainment rate is depicted in Figure 6.

With this exact entrainment rate below the first front the error drops from of order 10^{-1} m to of order 10^{-12} m. The accuracy of the numerical solution is limited by the number of significant digits in the constants in the analytical expressions. We can, therefore, conclude that the location of the first front is predicted exactly when we use the exact entrainment below the first front.

In practice we do not know the exact location of the first front and we are not able to calculate the exact volume entrained below the first front. To address ways of obtaining a second order correct entrainment calculation let us look at the Taylor expansion about time $t = t'$ of the general expression of the entrainment, Eq. (26), given by

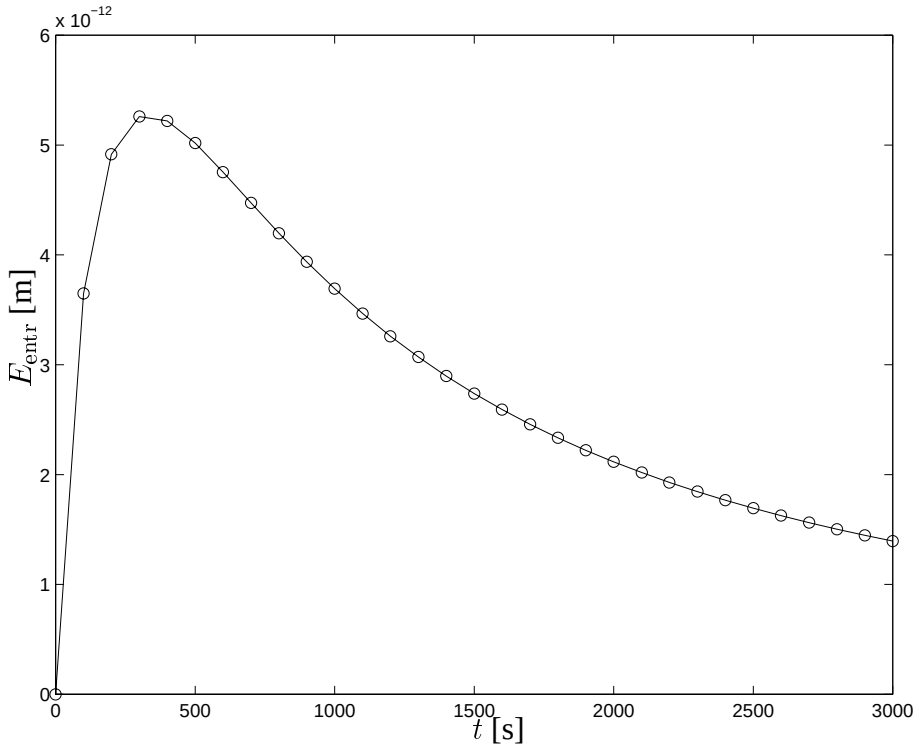

Figure 6 Error in the numerically calculated first front position using a exact entrainment below the first front.

$$
\begin{aligned}
V_{\rm entr,tot} &= Q_{\rm entr}(z_{k_0}(t'))\Delta t + \frac{1}{2}\left.\frac{dQ_{\rm entr}}{dz}\right|_{z_{k_0}(t')} w_{k_0}(t')\Delta t^2 + \mathcal{O}(\Delta t^3) \\
&= Q_{\rm entr}(z_{k_0}(t'))\Delta t - \frac{1}{2}Q'_{\rm entr}(z_{k_0}(t'))\frac{Q_{\rm entr}(z_{k_0}(t'))}{A_c(z_{k_0}(t'))}\Delta t^2 + \mathcal{O}(\Delta t^3)
\end{aligned}
\tag{30}
$$

We would have to adjust the entrainment calculation by an amount given by the second term to achieve a second order correct entrainment calculation. To mimic what we would do in practice we will not utilize the exact expression for the location of the first front (Eq. (24)) but instead use the numerically evaluated first front location denoted by $\hat{z}_{k_0}$. Using this approximation and the entrainment functions, Eqs. (15) and (16), we can write the first order correction (the second term in Eq. (30)) as

$$
\begin{aligned}
-\frac{1}{2}Q'_{\rm entr}(z_{k_0}(t'))\frac{Q_{\rm entr}(z_{k_0}(t'))}{A_c(z_{k_0}(t'))}\Delta t^2 &\simeq -\frac{1}{2}\frac{5}{3}k_\mu B^{1/3}[\hat{z}_{k_0}(t')]^{2/3}\frac{k_\mu B^{1/3}[\hat{z}_{k_0}(t')]^{5/3}}{A_c(\hat{z}_{k_0}(t'))}\Delta t^2 \\
&= -\frac{5}{6}k_\mu^2 B^{2/3}[\hat{z}_{k_0}(t')]^{7/3}\frac{1}{A_c(\hat{z}_{k_0}(t'))}\Delta t^2
\end{aligned}
\tag{31}
$$

The error in the volume entrained below the first front, $E_{\rm entr,tot}$ [m^3], propagates to an error in the first front, $E_{z_{k_0}}$ [m]. The error in the first front can be calculated in terms of the

position of the first fronts at two time levels by noting that (for $w_{k_0} < 0$)

$$V_{\text{entr,tot}} = \int_{z_{k_0}(t'+\Delta t)}^{z_{k_0}(t')} A_c(z)dz \tag{32}$$

and

$$\hat{V}_{\text{entr,tot}} \triangleq Q_{\text{entr}}(z_{k_0}(t'))\Delta t = \int_{\hat{z}_{k_0}(t'+\Delta t)}^{z_{k_0}(t')} A_c(z)dz \tag{33}$$

where the $\hat{}$ indicates numerically evaluated quantities. Subtracting the two equations above we obtain

$$E_{\text{entr,tot}} \triangleq V_{\text{entr,tot}} - \hat{V}_{\text{entr,tot}} = \int_{z_{k_0}(t'+\Delta t)}^{\hat{z}_{k_0}(t'+\Delta t)} A_c(z)dz \tag{34}$$

In this test case A_c is constant with z and the error in the first front, $E_{z_{k_0}}$ [m], is given by

$$E_{z_{k_0}} = \frac{1}{A_c} E_{\text{entr,tot}} \tag{35}$$

We will now investigate how the error in the first front improves with the second order correct entrainment calculation. We conduct a numerical experiment where we start out with a single CV and then correct the entrainment at every time step with the term given by the last expression in (31).

In Figure 7 we compare the error in the first front obtained with the second order correct entrainment to the error with no correction (first order correct entrainment calculation).

The reduction in truncation error really pays off especially as the accuracy requirement is tightened. For a first front position accuracy requirement of 10^{-3} we would have to use a time steplength of 1.25 s with the first order method whereas with the second order correct entrainment calculation a time steplength of 20 s suffices, i.e. we get a 16 times reduction in time steps with this simple correction.

4 COMPARISON OF APPROXIMATE ANALYTICAL SOLUTION TO THE NUMERICAL SOLUTION

In Section 3.2 we compared numerical results to an analytical solution for the location of the first front. In this section we will compare approximate analytical solutions for

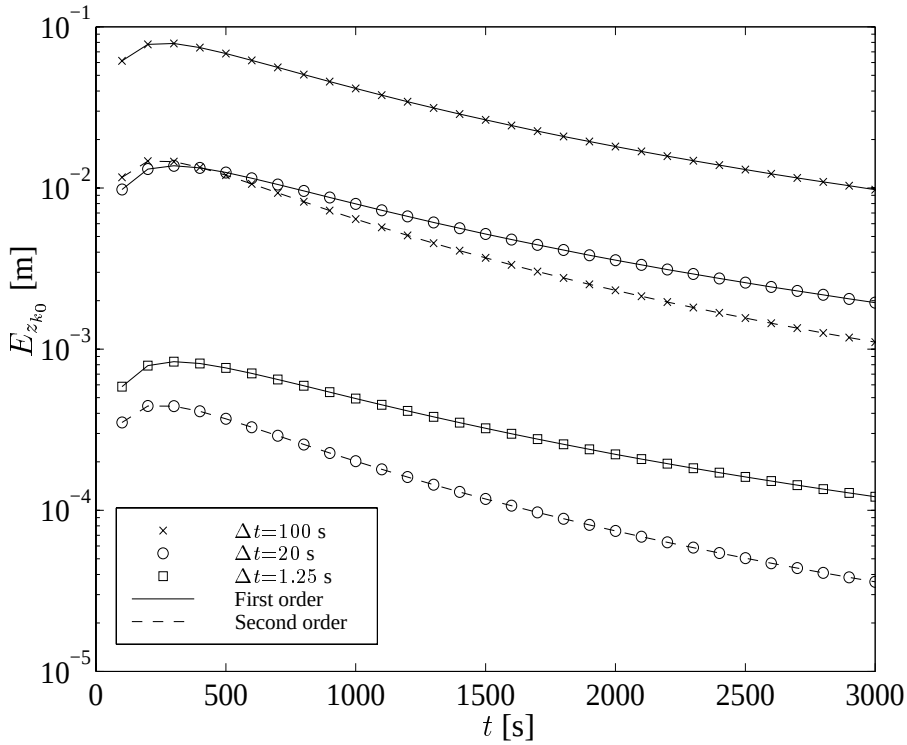

Figure 7 Comparison of the first front error with first and second order correct entrainment calculation.

the temperature distributions with the numerical counterpart for the same test case used in Section 3.

An analytical solution suitable for code validational purposes can be found in Worster and Huppert [1983]. This model is capable of simulating a single plume in a large enclosure and, therefore, provides a convenient and simple test case that is sufficiently complicated to test the major part of the code. The model of Worster and Huppert [1983] differs from our model in that the behavior of the plume is described accurately, in terms of differential equations of mass and momentum. These two conservation equations are coupled to the ambient through a differential equation which describes the exchange of buoyancy between the plume and ambient. Therefore, Worster and Huppert's formulation only conserves the buoyancy in the ambient which is different from our more detailed modeling of the ambient (conservation of mass, species and energy).

Since they are modeling the same problem as described in Section 3.1, a comparison of our model to theirs provides a way to validate our new model and code.

Since the model mentioned in Worster and Huppert consists of a set of coupled non-linear PDEs, no analytical solution can be found to the full set of equations. However, Worster and Huppert show that making certain simplifying assumptions they are able to come up with an *approximate* analytical solution. They show that the approximate solution is within on the order of 1% of a full (numerical) solution of their conservation equations. Worster and Huppert's approximate solution will briefly be stated below.

The non-dimensional buoyancy of the ambient, δ_{buo} [—], is defined by

$$\delta_{\mathrm{buo}} \triangleq 4\pi^{2/3}\alpha^{4/3}H_{\text{eff}}^{5/3}B^{-2/3}\Delta_{\text{amb}} \tag{36}$$

where Δ_{amb} [m/s^2] is the buoyancy of the ambient defined by

$$\Delta_{\text{amb}} \triangleq g\frac{\rho_{\text{amb}} - \rho_{\text{ref}}}{\rho_{\text{ref}}} \tag{37}$$

where ρ_{ref} [kg/m^3] is a reference density and ρ_{amb} [kg/m^3] is the density of the ambient.

The approximate solution for δ_{buo} is given as

$$\delta_{\mathrm{buo}} = f^{2/3}\delta_{\mathrm{buo},\infty} - C \tag{38}$$

where

$$\begin{aligned}
f(\tau) &\triangleq \frac{1-\eta_{k_0}^{5/3}}{1-\eta_{k_0}} \\
\delta_{\mathrm{buo},\infty} &\triangleq 5\left(\frac{5}{18}\right)^{1/3}\eta^{-2/3}\left\{1-\frac{10}{39}\eta-\frac{155}{8112}\eta^2+\cdots\right\} \\
C &\triangleq 5\left(\frac{5}{18}\right)^{1/3}\left\{\frac{\eta_{k_0}^{-2/3}-1}{1-\eta_{k_0}}+3f^{2/3}\left[\frac{1-\eta_{k_0}^{1/3}}{1-\eta_{k_0}}-\frac{5}{78}\frac{1-\eta_{k_0}^{4/3}}{1-\eta_{k_0}}\right.\right. \\
&\qquad \left.\left.-\frac{155}{56784}\frac{1-\eta_{k_0}^{7/3}}{1-\eta_{k_0}}+\cdots\right]\right\}
\end{aligned} \tag{39}$$

where η_{k_0} [—] is the dimensionless position of the first front defined by

$$\eta_{k_0} \triangleq \frac{z_{k_0}}{H_{\text{eff}}} \tag{40}$$

and η [—] is the dimensionless elevational coordinate defined by

$$\eta \triangleq \frac{z}{H_{\text{eff}}} \tag{41}$$

Since we are interested in the temperature distribution in the ambient not the density distribution we introduce the coefficient of thermal expansion, β [1/K],

$$\frac{\partial\rho}{\partial T} = -\rho\beta \tag{42}$$

Assuming a constant thermal expansion coefficient we can write Eq. (42) as

$$\frac{\rho - \rho_{\text{ref}}}{T - T_{\text{ref}}} = -\rho_{\text{ref}}\beta_{\text{ref}} \tag{43}$$

where the subscript 'ref' indicates that the properties should be evaluated at some reference state (eg. $(p_{\text{ref}}, T_{\text{ref}})$). Using Eq. (43) we can write

$$-\frac{1}{g}\Delta_{\text{amb}} = -\frac{\rho_{\text{amb}} - \rho_{\text{ref}}}{\rho_{\text{ref}}}\beta_{\text{ref}}(T_{\text{amb}} - T_{\text{ref}}) \tag{44}$$

which means that we can write the temperature in the ambient, T_{amb} [°C], as

$$T_{\text{amb}} = \frac{-\delta_{\text{buo}}}{4\pi^{2/3}\alpha^{4/3}H_{\text{eff}}^{5/3}B^{-2/3}g\beta_{\text{ref}}} + T_{\text{ref}} \tag{45}$$

Figure 8 plots the simulated temperature distribution in the environment for 5 time instances. The results were obtained by running the `BMIX` code with the input data given in Section 3.1 using a time steplength of $\Delta t = 0.5\,\text{s}$.

Figure 9 compares the analytical *approximate* solution to the one obtained from the numerical simulation. The two solutions are essentially identical noting that the analytical solution is an approximate solution to a slightly different model.

Any numerical method introduces a discretization error in the solution. In the remainder of this section we will demonstrate that the discretization error in the computed solution is negligible.

Using the standard finite difference method on a fixed (stationary) computational grid it is easy to halve the size of each computational cell in the discretized (z, t) domain to obtain discretization error estimates. In our case the situation is complicated by the fact that our *computational grid is itself dynamic*. In fact, the computational grid evolves depending on the solution, because the movement and entrainment of the individual computational cell depend on the solution.

To illustrate the dynamic behavior of the computational grid Figure 10 shows the computational grid for three time instances. The time steplength was chosen to a value of $\Delta t = 20\,\text{s}$ and the initial computational grid corresponds to 30 uniform control volumes, i.e. $K = 30$. The reason that we show the grid for a relatively large time steplength is that otherwise we would end up with even smaller CVs as time evolves. This would make it hard to distinguish the CVs since in this computation we do not employ CV merging to manage the CV population. Also, even though the time steplength is large, the computed solution is still accurate. For every time step, a new CV is added at the discharge level of the plume (here the top of the enclosure). The size of the CV added varies linearly with Δt since the total entrained volumetric flow rate is given and time independent[7]. Therefore, the fineness of the computational grid in the z-direction is directly proportional to Δt.

[7] In general the total entrainment volumetric flow rate need not be constant since the discharge elevation might change with time.

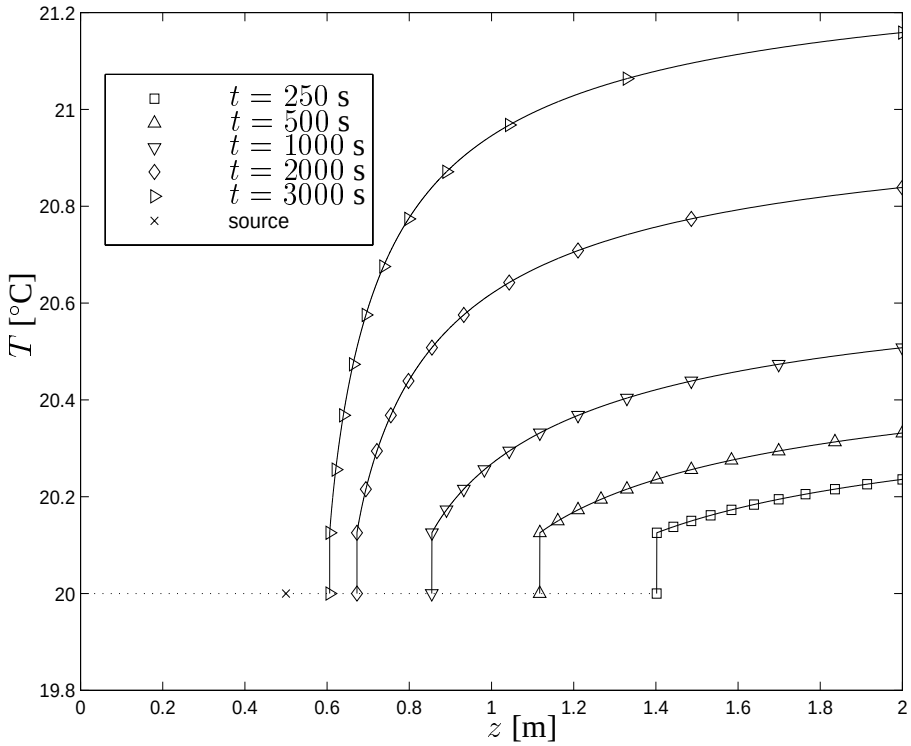

Figure 8 Temperature distribution for five time instances.

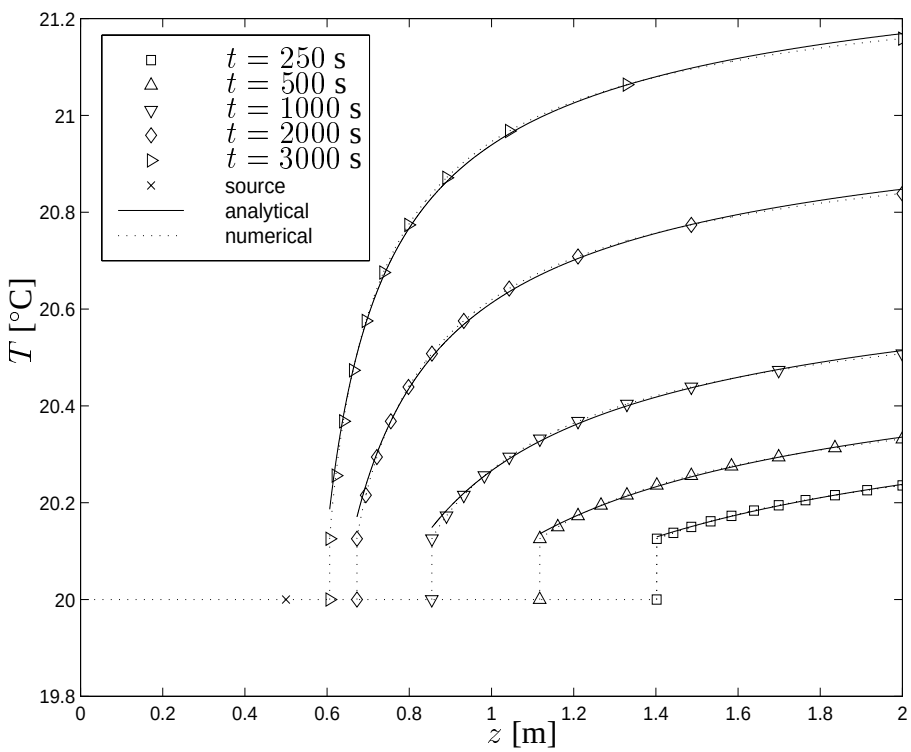

Figure 9 Comparison of the analytical and numerical temperature distribution for five time instances.

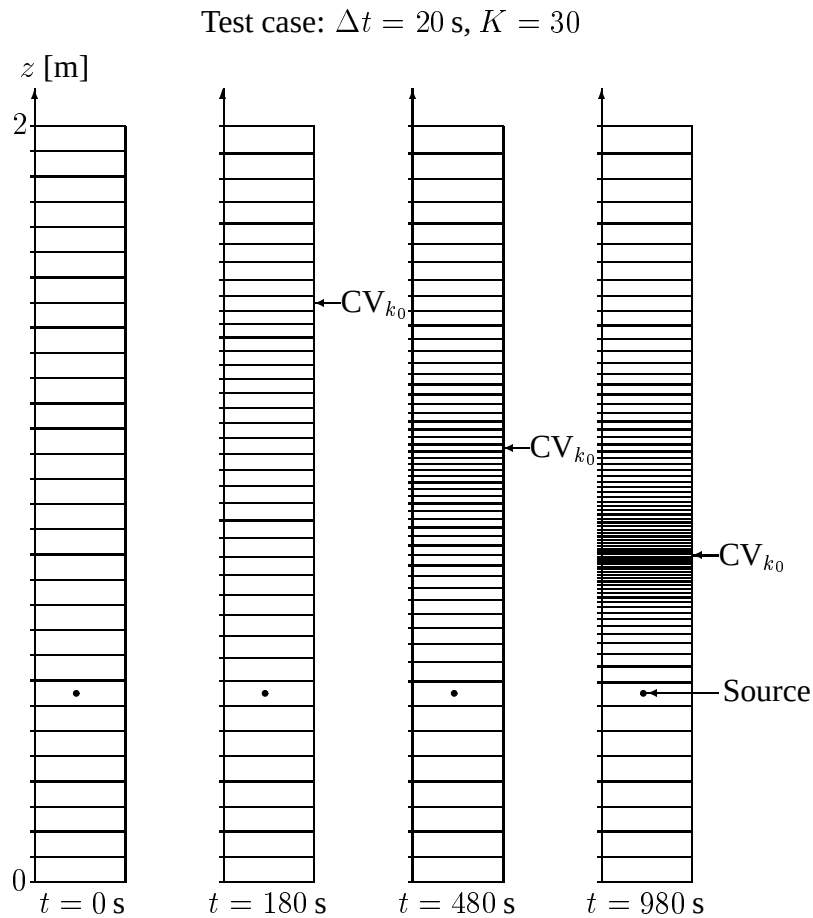

Figure 10 Example of the evolution of the computational grid with time.

Therefore, to study the effect of discretization errors in the solution we consider only the time steplength, Δt. Comparing two solutions for different Δt is complicated by the fact that the computational grid evolves differently for different time steplengths so the solution "points" in one grid do not match those in a grid with a different time steplength.

Let us denote the solution at some $t = T$ computed using some time steplength, Δt, by $\underline{u}_{\Delta t}(T)$. In order to compare $\underline{u}_{\Delta t}(T)$ with $\underline{u}_{\Delta t'}(T)$ (where $\Delta t'$ is a multiple of Δt, say) we will interpolate both solutions using cubic splines and we will denote the (continuous) functions of elevation (z) obtained in this way by $\hat{u}_{\Delta t}(T, z)$ and $\hat{u}_{\Delta t'}(T, z)$. We will define the difference between the two solutions in terms of the ∞-norm,

$$E_{\Delta t}(T) \triangleq \|\hat{u}_{\Delta t}(T, z) - \hat{u}_{\Delta t'}(T, z)\|_\infty \tag{46}$$

where the infinity norm is defined by

$$\|\cdot\|_\infty \triangleq \max|\cdot| \tag{47}$$

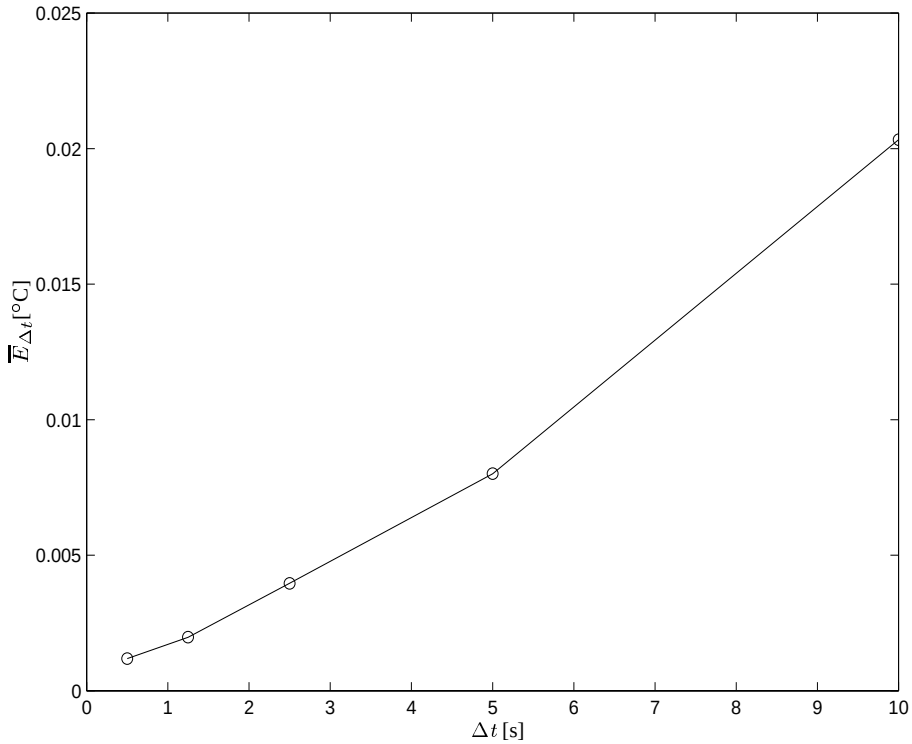

Figure 11 Error estimate for the temperature distribution.

i.e. in our case we need to find

$$E_{\Delta t}(T) = \max_{z \in [0\,\mathrm{m};2\,\mathrm{m}]} |\hat{u}_{\Delta t}(T,z) - \hat{u}_{\Delta t'}(T,z)| \tag{48}$$

Note that interpolation errors occur with every form of interpolation. In the case with cubic splines it can be shown that the interpolation error is of order $\mathcal{O}(H^2)$ where H is the maximum spacing between all the interpolated points. However, this second order behavior is only felt close to the end points of the spline. In the interior of the interpolated interval the error behaves like $\mathcal{O}(H^4)$ (Nielsen [1992]). In our case the interpolation error is small close to the end points since close to the first front the size of the computational cells is very small and close to the top of the enclosure the curvature of the solution is small. Therefore, the error associated with the interpolation process can be completely neglected.

In Figure 11 we have depicted the error estimate given by Eq. (48) with $\Delta t' = 2\Delta t$ for the temperature distribution. As we can see the truncation errors are negligible for a time steplength of $\Delta t = 0.5$ s and even for a time steplength of 20 s the numerical solution is very accurate. This is also seen in Figure 12 where we have compared solutions at $t = 3000$ s obtained with time steplengths of 0.5 s and 20 s, respectively. The difference between the two solutions is hardly noticeable which confirms the high accuracy at even large time steplengths.

In the test case the steplength in the z-direction in the initial grid has absolutely no effect on the error of the computed solution. This is easy to see in the figure of the computational grid for the three time instances (see Figure 10). This means that we would

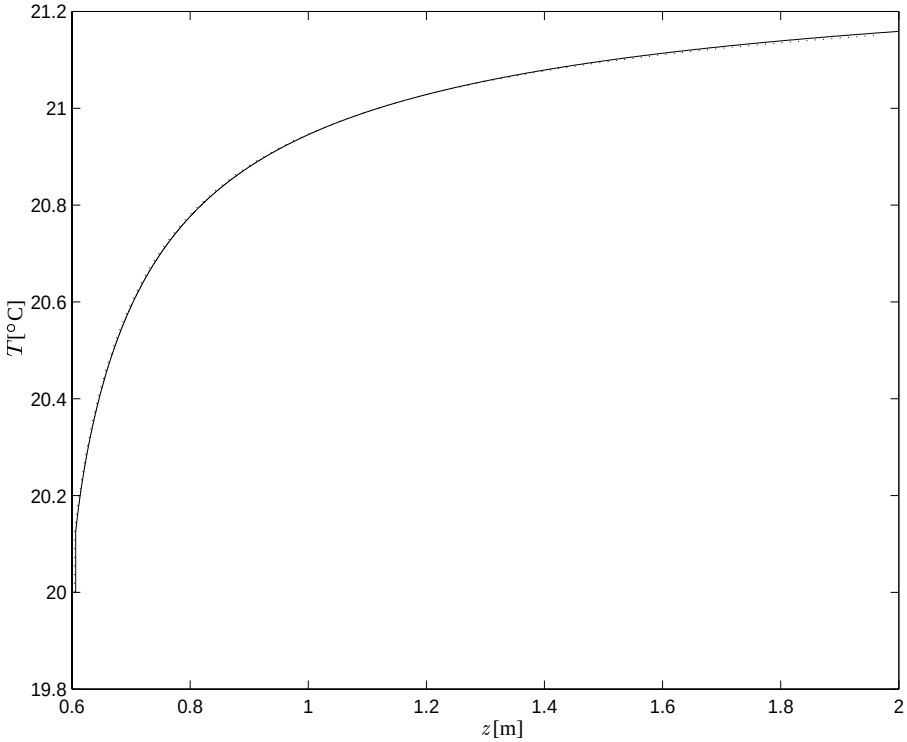

Figure 12 Comparison of coarse grid ($\Delta t = 20$ s) and fine grid ($\Delta t = 0.5$ s) solutions at $t = 3000$ s.

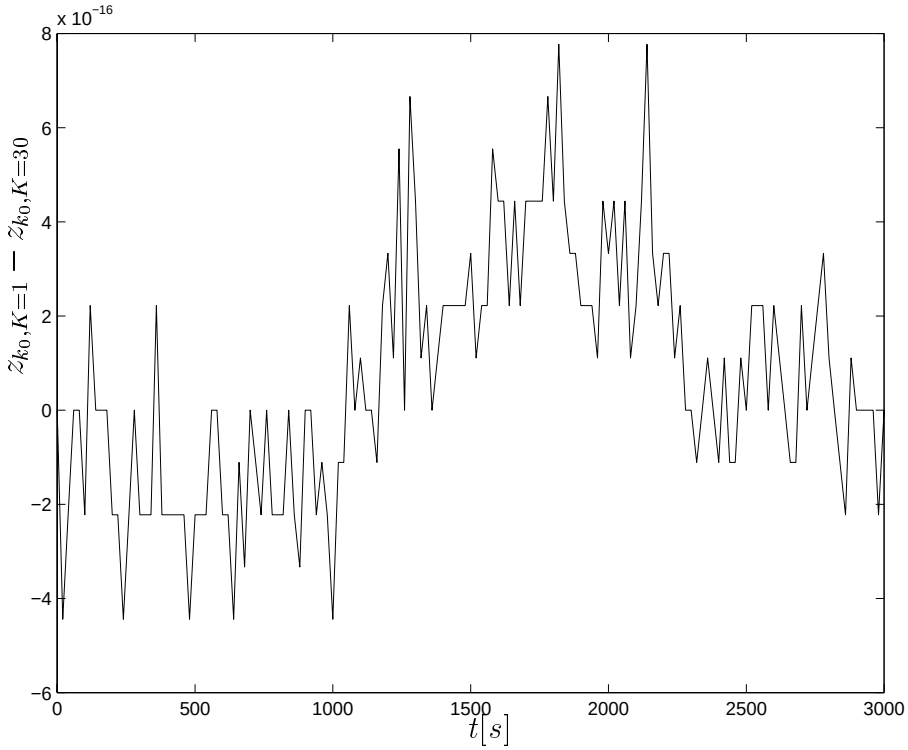

Figure 13 Difference in solution for two different initial grids.

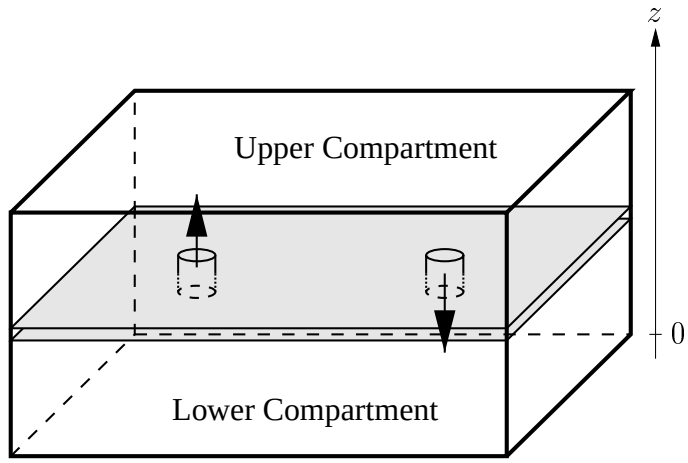

Figure 14 Schematic illustration of flow exchange experimental setup.

in fact obtain the same results if we were to start out with just one CV in the initial grid. This statement was checked by running the code with the same time steplength ($\Delta t = 20$ s) but with $K = 1$ instead of 30. The difference between the calculated first front location for the two different initial grids is depicted in Figure 13. The statement is confirmed by the numerical experiment—the error is within machine precision. This statement is only true when we have a homogeneous enclosure initially (uniform properties) such that no discretization error occurs when discretizing the continuous domain initial conditions.

5 VALIDATION OF `BMIX` CODE AGAINST EXPERIMENTAL DATA

In this section the `BMIX` code is validated against three series of flow exchange experiments. All the experiments were conducted using a square tank (dimensions 0.578 m long, 0.289 m wide, and 0.600 m high) with two equal sized horizontal compartments as depicted in Figure 14. Flow from one compartment to the other were accomplished by two openings symmetrically placed on the two halves of the horizontal plate that separated the compartments. In order to stabilize the flow through the openings, two pipes or chimneys were placed in the openings. The two chimneys had an inner diameter of 1.52 cm and a length of 5.2 cm each penetrating 2.6 cm into the lower compartment. High density fluid (sugar or salt water) was placed in the top compartment and pure water in the bottom compartment. When the experiment was started by simultaneously pulling two plugs blocking the two openings, the heavy fluid flowed down through one opening and the light fluid flowed up through the other to produce an equilibrium state. Measurements of the flow rate through the openings were performed by a hot wire probe, and the density profile in the bottom compartment measured using a sheet laser (Kuhn et al. [1999]).

The entrainment rate per unit length of the downward buoyant jet was modeled using Eq. (16). The buoyancy flux for injected fluid, B_{in} [m^4/s^3], is given by

$$B_{\text{in}} = gQ_{\text{in}} \frac{\rho_{\text{amb}} - \rho_{\text{in}}}{\rho_{\text{amb}}} \tag{49}$$

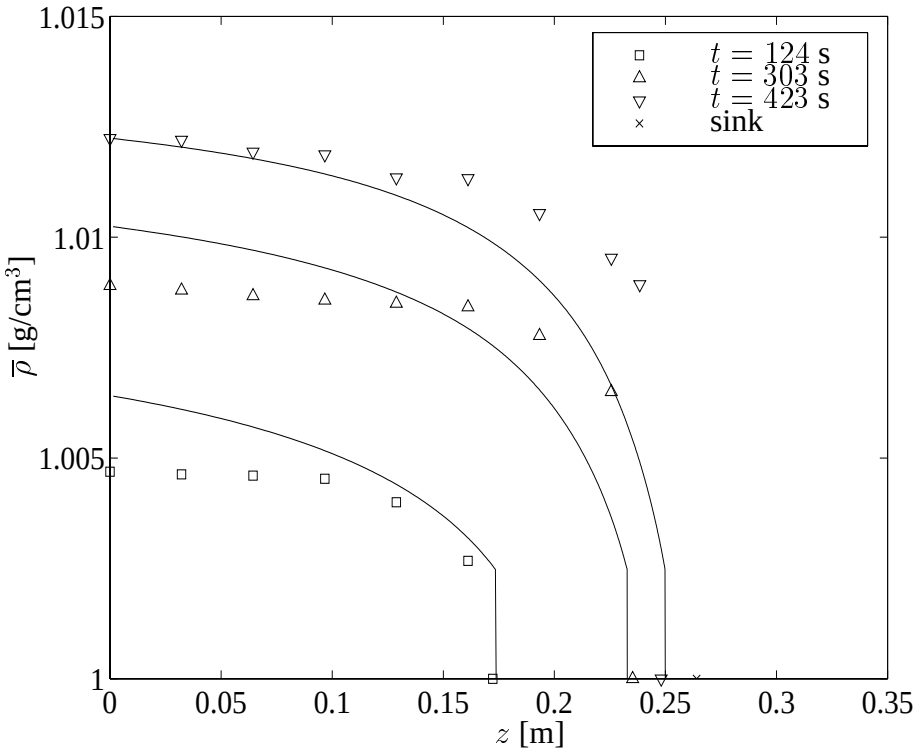

Figure 15 Comparison of the numerical model with exchange flow experimental sugar water data for $\rho^0_{\text{upper}} = 1.05 \cdot 10^3$ kg/m^3.

5.1 First series of experiments—both flow rate and density measured

During the first series of experiments both the flow rate injected into the lower compartment and the density profile for the lower compartment were measured.

Using the measured flow rates we know the volume and mass of injected fluid and since the fluid is incompressible the volumetric flow rate out balances the inlet flow rate. In the `BMIX` code the discrete time flow rate measurements were fitted with a natural cubic spline to facilitate flow rate evaluation. After choosing the entrainment constant (α) all the necessary data are available to simulate the experiment. Note that since this experiment is isothermal there is no need to compute the enthalpies, i.e. the energy conservation equation (7) is disabled in this computer simulation.

In Figures 15 and 16 we have a comparison between simulations and two sets of experimental data for initial upper compartment sugar water densities of $\rho^0_{\text{upper}} = 1.05 \cdot 10^3\,\text{kg/m}^3$ and $\rho^0_{\text{upper}} = 1.086 \cdot 10^3$ kg/m^3 respectively.

Both simulations use a time steplength of $1\,\text{s}$ (giving negligible truncation errors) and entrainment constants of $\alpha = 0.1148$ for the 1.05 density case and $\alpha = 0.082$ for the 1.086 density case. The choices of entrainment constants are consistent with the experimental observation that lower velocity buoyant jets have higher entrainment rates compared to higher velocity, more jet-like buoyant jets.

Several factors complicate the modeling of the experiments. The simulated results

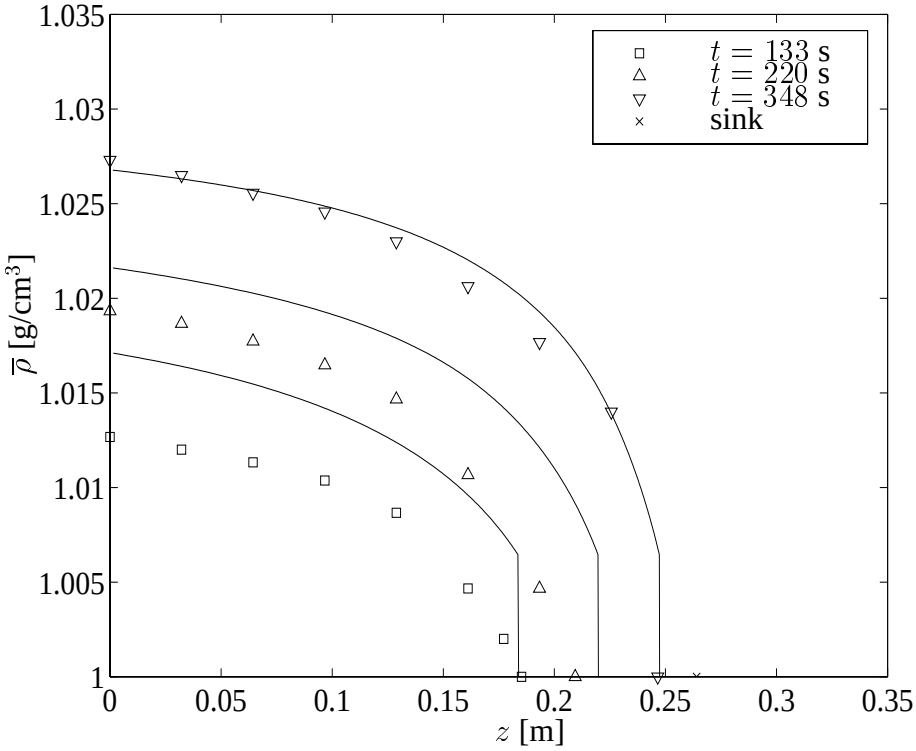

Figure 16 Comparison of the numerical model with exchange flow experimental sugar water data for $\rho^0_{\text{upper}} = 1.086 \cdot 10^3\,\text{kg/m}^3$.

show high sensitivity to the measured flow rate. The relatively high uncertainty of the hot wire probe velocity measurement therefore limits the comparison. Also, since the driving potential for flow diminishes with time, the characteristics of the buoyant jet change with time which makes it more difficult to model the buoyant jet with just one fixed entrainment constant, α.

Furthermore, even for a steady flow rate the entrainment rate per unit length varies with position along the buoyant jet especially near the inlet. As the buoyant jet enters the enclosure it is usually fully or mostly laminar but in most real life applications and experiments the velocity of the buoyant jet is high enough to transform the initially laminar buoyant jet to a fully developed turbulent buoyant jet. Predicting the length of and especially the entrainment within the transition regime are very difficult tasks because, as it is verified by many experients, these characteristics are highly dependent on fluid properties upstream of the inlet (i.e. how the buoyant jet was generated), especially the turbulence characteristics upstream play an important role.

As a result, as the first front moves closer and closer to the sink (at the same elevation as the inlet of the buoyant jet) the prediction of the first front position becomes very uncertain because the entrainment into the buoyant jet from the unchanged fluid layer between the sink and the first front position is difficult to predict. At this time just a small error in the position of the first front or the flow rate will cause the first front to move up to the sink and heavy fluid will ultimately be ejected which of course is not physically possible. This is why we have only modeled the experiment until the first front is within approximately $2\,\text{cm}$ of the sink.

The experimental data for the 1.05 density case (see Figure 15) are predicted reasonably well throughout the experiment. The early density profile is clearly overpredicted as it is for both experiments and the last density profile is underpredicted. Generally the experimental profiles are flatter indicating a more uniform density than predicted.

The most important phenomenon that explains the disagreement early in the experiment is the transit time for fluid to travel from the exit of the plume to the far corner of the enclosure where the density profile is measured. The fluid exiting has to travel horizontally about 43 cm in order to reach the point where the density is measured. This length is larger than the vertical direction the buoyant jet travels (about 30 cm) and since the horizontal velocity of fluid exiting is considerably less than the vertical velocity in the buoyant jet this delay and build-up of dense fluid near the plume exit become important in the high-flow regime seen initially in the experiment.

The reason that the last density profile in Figure 15 is underpredicted is found in the uncertainty in the flow rate measurement because at 7 minutes into the experiment the density gradient within the enclosure is fully stabilized and is, to a very good approximation, 1-D.

For the 1.086 density case (see Figure 16) the shape of the density profiles is predicted much better. We should note that the experimental flow rate used in the simulation has been reduced by 5 percent. This was supported by systematic density mismatch in the long term and since the flow rate measurement is relatively uncertain we found this a reasonable correction. The overprediction early in the experiment is clearly worse compared to the 1.05 density case. The reason for this is that in this case the flow rate is higher and the transit time and build-up of heavy fluid close to the exit of the buoyant jet become more important. However, the prediction of the long time density profile is excellent.

In this case we have two physical processes which affect the degree of stability of the density distributions. First of all having a higher density difference between the injected and initial lower compartment fluid tends to enhance stable stratification and this would tend to improve the agreement between the experiment and computation. This is confirmed by noting that the *shape* of the 1.086 density experimental curves fit the model curves to an excellent degree and much better than for the 1.05 density case. The second effect is that of turbulent mixing. Since we are studying flow exchange, increasing the initial density difference between the two compartments will increase the driving potential for flow. This will in turn increase the flow rate and thereby increase turbulent mixing especially in the initial phase (first couple of minutes) of the experiment. The fact that the experimental density at the first front is much lower than predicted for the 1.086 density case is due to turbulent mixing in the high flow regime at early times.

Because the steepness of the front in the simulated results is preserved throughout we conclude that molecular diffusion is negligible in this experiment, which is not surprising considering the time scale of the convective flow of around 10 minutes.

5.2 Second series of experiments—only density measured

In the next series of experiments the plate separating the two compartments in the water tank was re-fitted such that the lower compartment inner height was 0.29 m (De Bernardis [1999]). Furthermore, in this series of experiments the flow rate was not measured.

In order to simulate the experiments we have to specify the flow rate. Since we do

not have direct measurements of the flow rate for these experiments we have to calculate the flow rate indirectly from the density measurements. We will do this by considering the control volume formulation of the mass conservation equation for the whole of the lower compartment which can be written as

$$\frac{\partial}{\partial t}\int\limits_{V_{\mathrm{tot,lower}}} \rho_{\mathrm{lower}}\, dV = Q_{\mathrm{in}}(\rho^0_{\mathrm{upper}} - \rho^0_{\mathrm{lower}}) \tag{50}$$

where ρ^0_{lower} and ρ^0_{upper} are the initial densities of the upper and lower compartments, respectively.

Since the cross-sectional area of the tank is constant we can write the above equation as

$$A_c\frac{\partial}{\partial t}\int\limits_{z_{\mathrm{bot}}}^{z_{\mathrm{top}}} \rho_{\mathrm{lower}}(z,t)\, dz = Q_{\mathrm{in}}(t)(\rho^0_{\mathrm{upper}} - \rho^0_{\mathrm{lower}}) \tag{51}$$

Assuming we have two density measurements, one at $t = t_0$ and one at $t = t_0 + \Delta t$ we can approximate the LHS of Eq. (51) using

$$\begin{aligned} A_c\frac{\partial}{\partial t}\int\limits_{z_{\mathrm{bot}}}^{z_{\mathrm{top}}} \rho_{\mathrm{lower}}(z,t)\, dz\Bigg|_{t=t_0+\frac{\Delta t}{2}} &= \frac{A_c}{\Delta t}\int\limits_{z_{\mathrm{bot}}}^{z_{\mathrm{top}}} \{\rho_{\mathrm{lower}}(z,t_0+\Delta t) \\ &\qquad - \rho_{\mathrm{lower}}(z,t_0)\}\; dz + \mathcal{O}(\Delta t^2) \end{aligned} \tag{52}$$

Using this second order correct approximation, Eq. (52), and isolating the flow rate from Eq. (51) we obtain the following expression for the *calculated* injected flow rate, Q_{in} [m^3/s], based on two measured density profiles

$$\begin{aligned} Q_{\mathrm{in}}\left(t_0 + \frac{\Delta t}{2}\right) &\simeq \frac{1}{\rho^0_{\mathrm{upper}} - \rho^0_{\mathrm{lower}}}\frac{A_c}{\Delta t}\int\limits_{z_{\mathrm{bot}}}^{z_{\mathrm{top}}} \{\rho_{\mathrm{meas,lower}}(z,t_0+\Delta t) \\ &\qquad - \rho_{\mathrm{meas,lower}}(z,t_0)\}\; dz \end{aligned} \tag{53}$$

where the subscript ‘meas’ indicates an experimentally measured value.

It is important to note that this type of validation is not as strong as when we have an independent measurement of the flow rate because the information we want to validate is used to generate input data for the `BMIX` code. This kind of validation can, nevertheless, compare the shape of the density profiles and the position of the first front.

In Figures 17-22 we show both the calculated flow rates and comparisons between the experimental data and the numerical model.

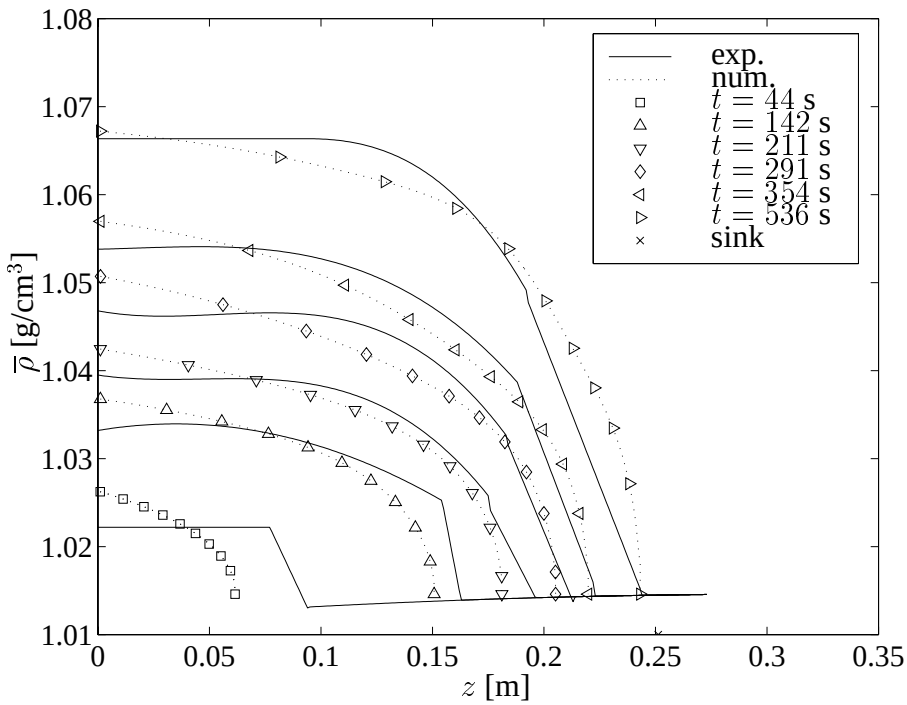

Figure 17 Comparison of the numerical model with experimental data for salt water with $\rho^0_{\text{upper}} = 1.197 \cdot 10^3\ \text{kg/m}^3$.

The calculated flow rates were fitted by a cubic spline. Because we have very few data points we need to introduce artificial data points for two experiments to prevent the spline from performing strong and unrealistic oscillations. This is typical for cubic splines when we try to fit few data points which show oscillatory behavior (from a signal processing perspective we have tried to sample an oscillatory signal with too few point and therefore loose the ability to predict (reconstruct the continuous time signal) the signal).

The two first experiments were made with salt water and initial upper compartment densities of $\rho^0_{\text{upper}} = 1.197 \cdot 10^3\ \text{kg/m}^3$ and $\rho^0_{\text{upper}} = 1.105 \cdot 10^3\ \text{kg/m}^3$, respectively. The entrainment constants used to simulate the two experiments are $\alpha = 0.066$ and $\alpha = 0.073$. A time steplength of $1\,\text{s}$ was used giving negligible truncation errors.

From the figures we see that the density profiles are predicted very well in both cases except for the density profiles in the very beginning of the experiments. This is natural because the buoyant jet needs time to reach a quasi steady-state in terms of entrainment. This also explains the poor prediction of the first front in the beginning of the experiments. The entrainment characteristics are different in the beginning compared to the overall entrainment constant we have used to predict all of the data.

As we have noted before, the experimental density profiles tend to be a bit flatter than predicted.

The last experiment in this series is with sugar water of density $\rho^0_{\text{upper}} = 1.109 \cdot 10^3\ \text{kg/m}^3$. The calculated flow rate exhibits the same double-humped characteristics as

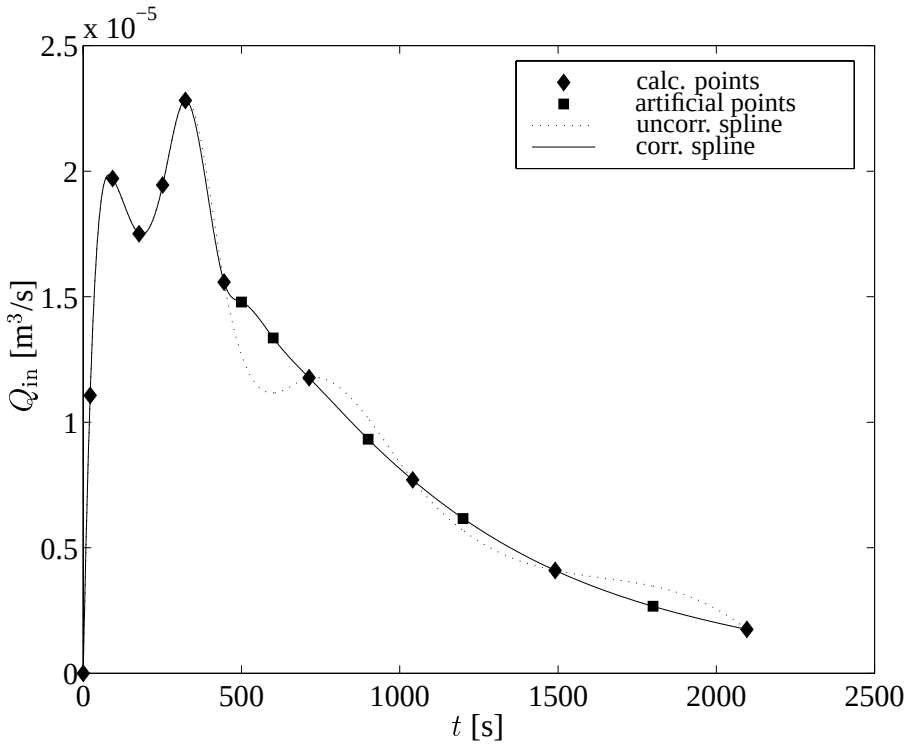

Figure 18 Calculated flow rate for salt water experimental data for $\rho^0_{\text{upper}} = 1.197 \cdot 10^3\,\text{kg/m}^3$.

the high density salt water case (see Figure 18). The flow rate for sugar water is lower compared to salt water with the same density because the flow loss through the chimney is higher due to the higher viscosity of sugar water. The prediction for this case is good but a little worse than for the salt water experiments possibly due to leaking.

One of the problems with these data sets is leaking. Leaking through the sealing of the horizontal plate causes high density fluid to flow down along the side of the tank. We believe that the presence of high density fluid from leaks at the location where the laser light penetrates the tank increase the uncertainty of the density measurement and that this is the cause for the unstable density profile seen initially in the experiments. This would also explain why we see an increase in the density of the fluid above the first front in the last experiment (see Figure 21).

5.3 Third series of experiments—known fixed flow rate

In the third series of experiments the flow rate is kept at a known fixed value using forced injection and controlling the flow rate using a rotometer (Kuhn [1999]).

In the first experiment, salt water with a density of $\rho_{\text{in}} = 1.16 \cdot 10^3\,\text{kg/m}^3$ is injected into fresh water in the lower compartment at a constant flow rate of $Q_{\text{in}} = 7.38 \cdot 10^{-6}\,\text{kg/s}$. In the simulation the time steplength was $1\,\text{s}$ to eliminate the importance of truncation errors and the entrainment constant was $\alpha = 0.124$. The entrainment constant for this experiment is considerably higher than for the flow exchange experiments described in Sections 5.1-5.2. The higher entrainment in this case is most likely caused by the different turbulence

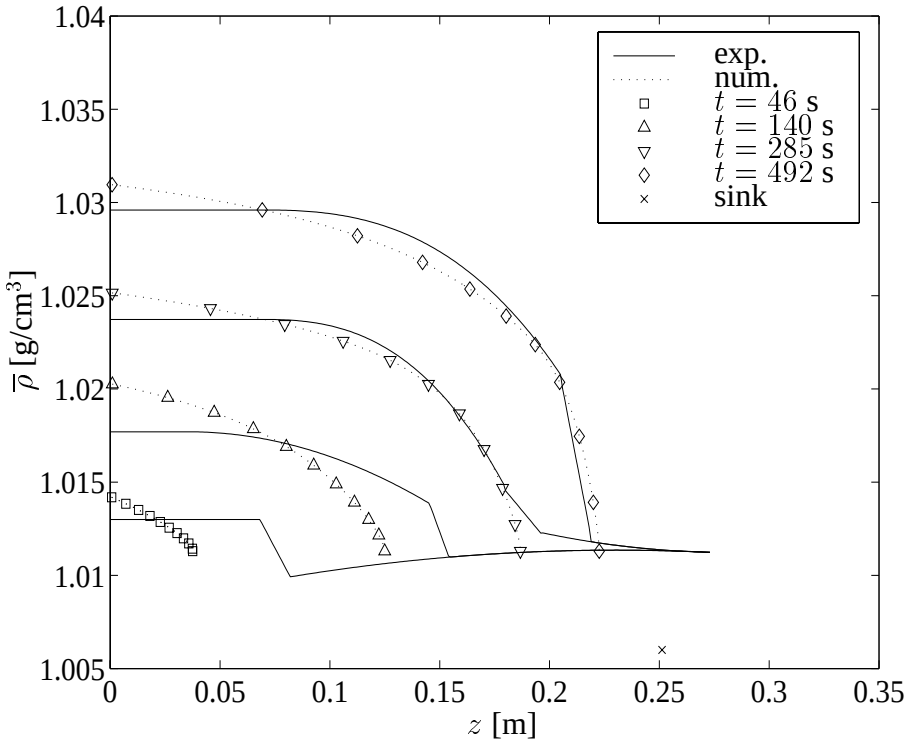

Figure 19 Comparison of the numerical model with experimental data for salt water with $\rho^0_{\text{upper}} = 1.105 \cdot 10^3$ kg/m^3.

characteristics associated with the generation of this flow (hose, rotometer, valve, etc.) and once again underlines the importance of buoyant jet generation on the entrainment characteristics.

In Figure 23 the experimental data for the first low flow case are compared to the numerical simulation. The agreement is excellent especially in the long term. For this case, however, the prediction of the movement of the first front is not as good as for the previous experiments. The difficulties in predicting the first front location may be fluctuating entrainment characteristics of the buoyant jet.

In Figure 24 we compare the numerical simulation with experimental data obtained at the higher flow rate $11.19 \cdot 10^{-6}\,\mathrm{m}^3/\mathrm{s}$. Again a $1\,\mathrm{s}$ time steplength was used and the entrainment constant was $\alpha = 0.1897$. The comparison shows good agreement between the numerical solution and experimental data and in the longer term the agreement is excellent. Also here the experimental data show a slightly flatter density profile than what is numerically predicted. We also note a slight mismatch in time integrated injected mass which can only be due to a slight ($\simeq 2\%$) flow rate measurement error.

6 CONCLUSIONS

In this paper we have introduced a Lagrangian method for modeling mixing processes in stably stratified large enclosures. The new `BMIX` code can accommodate any number of control volumes (multi-zone modeling) and eliminates artificial diffusion that would otherwise destroy the strong gradients that can be present in the flow field.

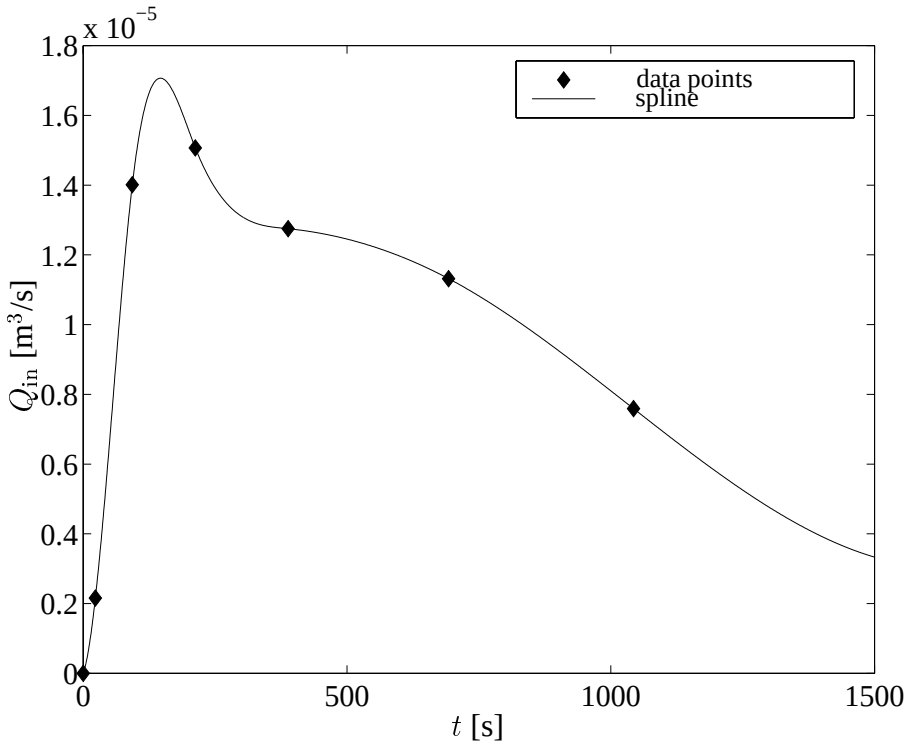

Figure 20 Calculated flow rate for salt water experimental data for $\rho^0_{\text{upper}} = 1.105 \cdot 10^3\,\text{kg/m}^3$.

The BMIX code represents the most detailed 1-D description possible but is still very computational efficient because the numerical model has a very lax stability criterion and in general require a relatively low number of zones to capture the flow field accurately.

Since this new numerical method is fundamentally different from standard finite difference methods used extensively in computational fluid dynamics we show the most important contribution to the total truncation error, the entrainment into a moving control volume, associated with this numerical scheme. It is demonstrated that correcting to first order the entrainment calculation for the movement of the control volume will make this method even more computational efficient because the time steplength can be increased considerably for the same accuracy requirement.

We first validated the correctness of the BMIX code against an analytical model for a single plume put forward by Worster and Huppert [1983]. The comparison shows excellent agreement and verified the correctness of the implementation.

Lastly we validated the BMIX model against three series of experimental data from a flow exchange experiment. The agreement between experimental data and the model is reasonably good especially for the long term density distribution in the enclosure.

NOMENCLATURE

$\triangleq$	Indicates a definition.
α	Entrainment constant [—].

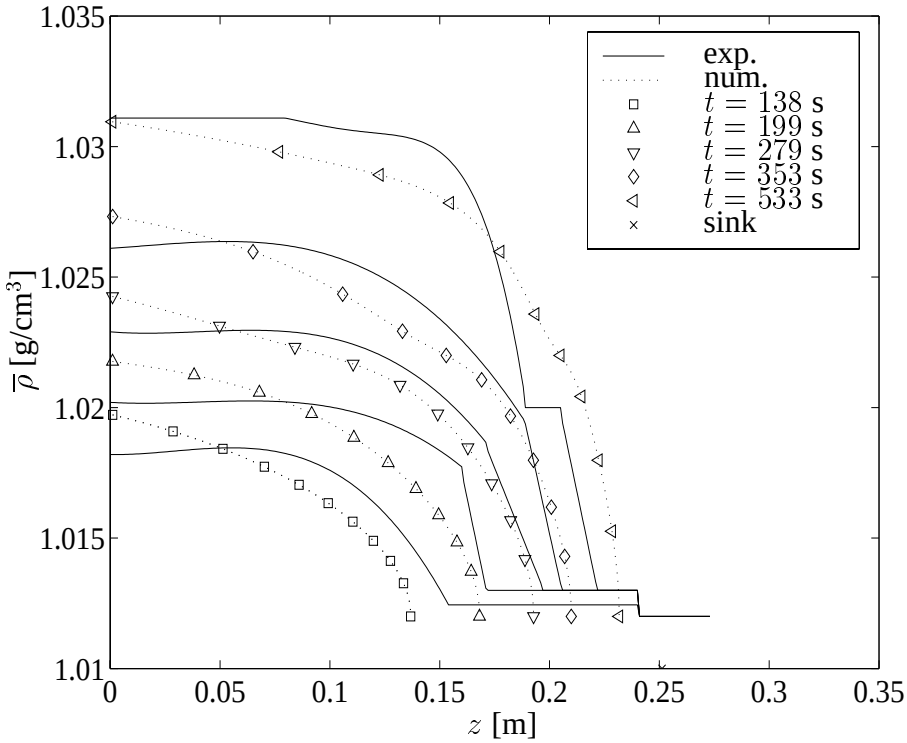

Figure 21 Comparison of the numerical model with experimental data for sugar water with $\rho^0_{\text{upper}} = 1.109 \cdot 10^3$ kg/m^3.

β	Constant of thermal expansion [1/K].
$\overline{\chi}$	Volume averaged mass fraction [—].
δ_{buo}	Non-dimensional buoyancy of the ambient [—].
Δ_{amb}	Buoyancy of the ambient [m/s^2].
η	Non-dimensional elevational coordinate [—].
ρ	Mass density [kg/m^3].
$\overline{\rho}$	Volume averaged total density [kg/m^3].
τ	Dimensionless time [—].
A	Surface area, horizontal cross-sectional area [m^2].
b	Radius of the axisymmetric buoyant jet [m].
B	Buoyancy flux [m^4/s^3].
c	Specific heat [J/(kg · K)].
C	Error constant for entrainment error [m·s], non-dimensional function in Worster and Huppert's approximate solution [—].
corr	Corrected.
CV	Control Volume.
D	Tank diameter [m].
$\mathcal{D}$	Mass diffusion coefficient [m^2/s].
E	Error. Error estimate.
exp	Experimental.

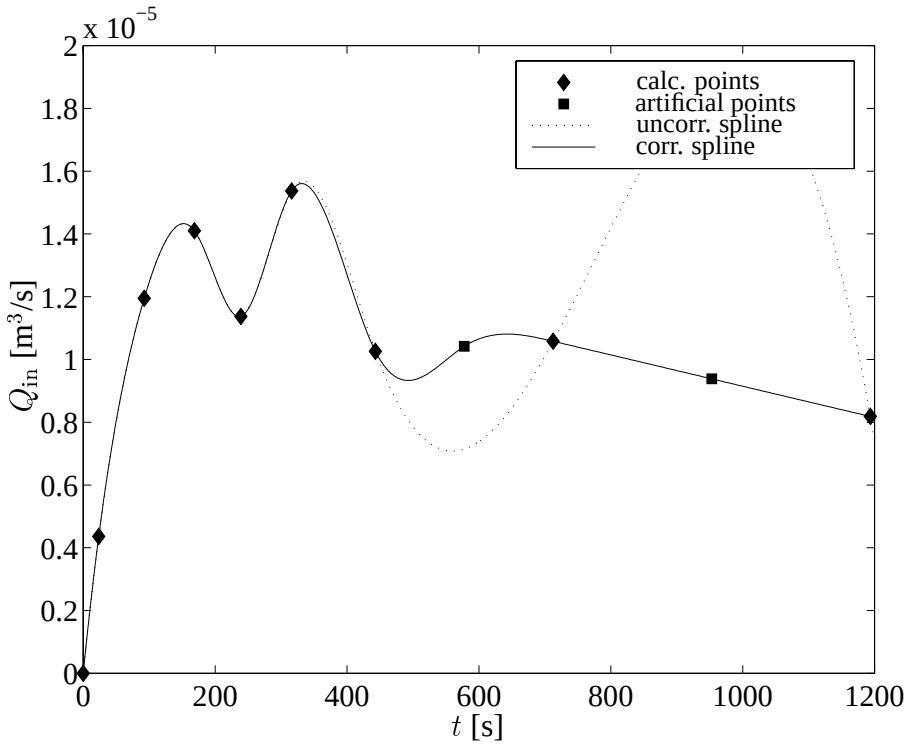

Figure 22 Calculated flow rate for sugar water experimental data for $\rho^0_{\text{upper}} = 1.109 \cdot 10^3\,\text{kg/m}^3$.

f	Non-dimensional function in the approximate solution of Worster and Huppert [1983].
g	Gravitational acceleration [m/s^2].
h	Enthalpy [J/kg].
$\overline{h}_{\text{mix}}$	Volume averaged mixture enthalpy [J/kg].
H	Height [m].
I	Total number of components in fluid [—].
k	Thermal conductivity [W/(m·K)].
k_μ	Taylor's entrainment constant [—].
K	Total number of control volumes in the enclosure [—].
L	Number of buoyant jets present in the enclosure [—].
LHS	Left Hand Side.
num	Numerical.
$\mathcal{O}(x^n)$	Function which satisfies $\lim_{x\to 0} \frac{\mathcal{O}(x^n)}{x^n} = 0$.
p	Pressure [Pa].
PDE	Partial Differential Equation.
$\dot{q}$	Heat addition rate [W].
q''	Heat flux due to heat diffusion [W/m^2].
Q	Volumetric flow rate [m^3/s].

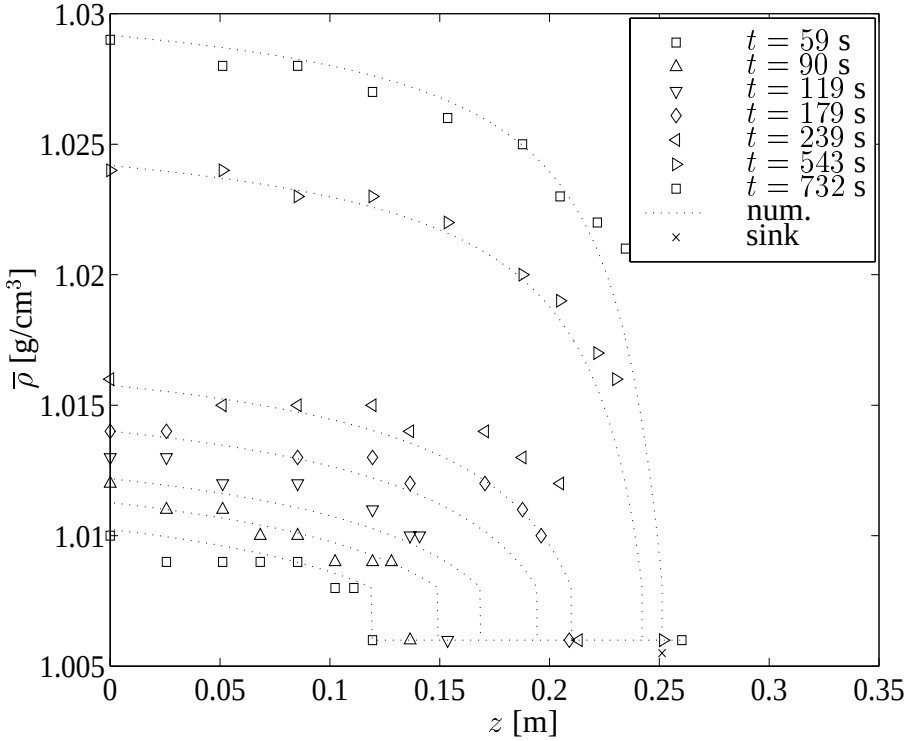

Figure 23 Comparison of the numerical model with experimental data points for fixed flow rate with $Q_{\text{in}} = 7.38 \cdot 10^{-6}$ kg/s.

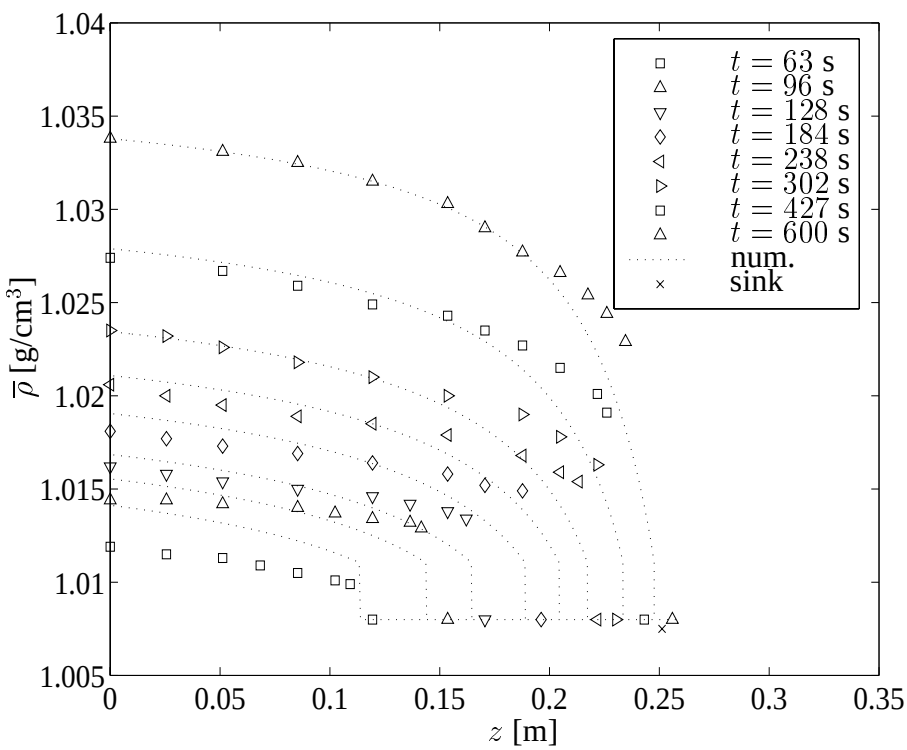

Figure 24 Comparison of the numerical model with experimental data points for fixed flow rate with $Q_{\text{in}} = 11.19 \cdot 10^{-6}$ kg/s.

$Q_{k,\ell}$	Volumetric flow rate entrained by buoyant jet ℓ within control volume k [m^3/s].
r	Radial coordinate [m].
s_{k_0}	Distance that the first front moves during a time step [m].
S,$\hat{S}$	Volume source and sink, respectively [m^3/s].
S_h,$\hat{S}_h$	Source and sink respectively of energy per unit time [W].
Δt	Time steplength [s].
T	Temperature [K].
$\underline{u}$	Vector of solution values at discrete points.
$\hat{u}$	Continuous function obtained by interpolation of discrete points.
uncorr	Uncorrected.
v	Velocity [m/s].
V	Volume [m^3].
$\dot{V}''$	Volumetric flow rate per unit area due to molecular diffusion [m^3/(m$^2\cdot$ s)].
w	Velocity in the positive z-direction [m/s].
z	Vertical coordinate [m].
Δz	Steplength in the z-direction [m].

Subscripts

0	Indicating (at) some reference value.
Δt	Using a time steplength of Δt.
∞	Steady state value in Worster and Huppert's approximate solution. As in $\|\cdot\|_\infty$ infinity norm.
k_0	At the position of the first front.
amb	Ambient.
av	Average total.
buo	Buoyancy.
c	Cross-sectional.
eff	Effective.
entr	Entrainment.
i	The ith component of the multicomponent fluid.
in	Injected.
k	For control volume number k.
lower	Lower compartment.
ℓ	ℓth buoyant jet.
max	Maximum.
p	Buoyant jet. Constant pressure.
r	Radial direction.
ref	Reference.
s	Source.
sf	Stratified ambient fluid.

top	Top of enclosure.
upper	Upper compartment.

Superscripts

Ψ'	'Ψ' per unit length.
Ψ''	'Ψ' per unit area.
$\dot{\Psi}$	'Ψ' per unit time.
$\overline{\Psi}$	Average value of Ψ.
$\hat{\Psi}$	Numerically evaluated Ψ, i.e. the value is distorted by numerical error.
$\tilde{\Psi}$	A value of Ψ which is somehow different from Ψ.
j	At time level j, i.e. at time $t = j\Delta t$. Specifically, 0 indicates an initial condition.

ACKNOWLEDGMENTS

Funding for this research was provided by the United States Department of Energy (US-DOE) under contract # FG07-96ER14731.

The first author gratefully acknowledges funds provided by Jytte and Gunnar Christensen for a high-end linux workstation which was used for this work.

Typeset with LaTeX 2_ε using the NURETH-9 class provided by Frank Moehle at ETH, Zurich.

REFERENCES

W.D. Baines and J.S. Turner. Turbulent buoyant convection from a source in a confined region. *Journal of Fluid Mechanics*, Vol. 37:pp 51–80, 1969.

Jakob Christensen. 1-D Steady-State Neutronics Thermal-Hydraulics Model of a SBWR. Master's thesis, Department of Fluid Mechanics, Technical University of Denmark, Lyngby., August 1995. 229 pages. On-line version see `http://www.jakobchr.com`.

Rocco De Bernardis. Selected topics for modeling of mixing in stratified volumes. Master's thesis, Department of Nuclear Engineering, University of California, Berkeley, 1999.

J. Floyd and L. Wolf. Comparison of measured data from the HDR-T51 gas fire tests to predictions made by CFAST. In *Second International Conference on Fire Research and Engineering, Gaithersburg, MD*, August 3-8 1997. Available on-line: http://flame.cfr.nist.gov/bfrlpubs/firedoctoc.html.

A.E. Germeles. Forced plumes and mixing of liquids in tanks. *Journal of Fluid Mechanics*, Vol. 132:pp 601–623, 1975.

S.Z. Kuhn. Experimental flow exchange data for fixed flow rate using a rotometer, 1999. Department of Nuclear Engineering, Thermal-hydraulics Laboratory, University of California at Berkeley.

S.Z. Kuhn, Choonjoo Lee, and Per F. Peterson. Density stratification from buoyancy-driven exchange flow through horizontal partitions in a liquid tank. In *9th International topical meeting on Nuclear Reactor Thermal hydraulics (NURETH 9)*, October 3-8 1999.

B.R. Morton, G.I. Taylor, and J.S. Turner. Turbulent gravitational convection from maintained and instantaneous sources. *Proc. Roy. Soc. London Ser. A*, Vol. 234:pp 1–23, 1956.

K.K. Murata and D.W. Stamps. Development and assessment of the CONTAIN hybrid flow solver. Technical Report SAND96-2792, Sandia National Laboratory, November 1996.

Hans Bruun Nielsen. Cubic splines. Technical University of Denmark, Institute of Mathematical Modeling, February 1992.

Richard D. Peacock, Glenn P. Forney, Paul A. Reneke, Rebecca M. Portier, and Walter W. Jones. CFAST, the consolidated model of fire growth and smoke transport. Technical Report NIST Technical Note 1299, National Institute of Standards and Technology, February 1993. Available on-line: http://www.bfrl.nist.gov/864/hazard/cfast.html.

Per F. Peterson. Scaling and analysis of mixing in large stratified volumes. *International Journal of Heat Transfer*, Vol. 37:pp 97–106, 1994.

K.E. Washington, K.K. Murata, R.G. Gido, F. Gelbard, N.A. Russell, S.C. Billups, D.E. Carroll, R.O. Griffith, and D.L.Y. Louie. Reference manual for the CONTAIN 1.1 code for containment severe accident analysis. Technical Report NUREG/CR-5715, U.S. Nuclear Regulatory Commission, May 1991.

M.G. Worster and H.E. Huppert. Time-dependent density profiles in a filling box. *Journal of Fluid Mechanics*, Vol. 132:pp 457–466, 1983.

Ninth International Topical Meeting on Nuclear Reactor Thermal Hydraulics (NURETH-9)
San Francisco, California, October 3 - 8, 1999.

Pressure Suppression Pool Mixing in Passive Advanced BWR Plants

Robert E. Gamble, Thuy T. Nguyen and Bharat S. Shiralkar
GE Nuclear Energy
San Jose, CA 95125 U.S.A.
robert.gamble@gene.ge.com

Per F. Peterson[1], Ralph Greif[2]
University of California
Berkeley, CA 94720-1730 U.S.A.
peterson@nuc.berkeley.edu

H. Tabata
Japan Atomic Power Company
1-6-1 Otemachi,Chiyoda-ku,Tokyo100-0004, Japan
hiroaki-tabata@japc.co.jp

KEY WORDS

Pressure Suppression Pools, Transient Stratification and Mixing

ABSTRACT

In the SBWR passive boiling water reactor, the long-term post-accident containment pressure is determined by the combination of noncondensible gas pressure and steam pressure in the wetwell gas space. The suppression pool (SP) surface temperature, which determines the vapor partial pressure, is very important to overall containment performance. Therefore, the thermal stratification of the SP due to blowdown is of primary importance. This work looks at the various phases and phenomena present during the blowdown event and identifies those that are important to thermal stratification, and the scaling necessary to model them in reduced size tests. This is important in determining which of the large body of blowdown to SP data is adequate for application to the stratification problem. The mixing by jets from the main vents is identified as the key phenomena influencing the thermal response of the suppression pool and analytical models are developed to predict the jet influence on thermal stratification. The analytical models are implemented into a system simulation code, TRACG, and used to model thermal stratification behavior in a scaled test facility. The results show good general agreement with the test data. Further development areas have been identified to verify the findings and improve the models.

[1] Department of Nuclear Engineering
[2] Department of Mechanical Engineering

1 INTRODUCTION

The new class of advanced reactors relies on passive safety grade containment systems rather than active ones to reduce cost and improve maintainability and reliability. As a result, phenomena that were previously of little or no importance have become important and some systems have received renewed attention - one being the suppression pool (SP) of passive boiling water reactors where pool surface temperature plays an important part in determining the overall long-term containment pressure.

In the SBWR passive boiling water reactor (Upton et al, 1996), the long-term containment pressure is determined by the combination of non-condensable gas pressure and steam pressure in the wetwell (WW) gas space, the latter governed by the suppression pool surface temperature. While the SBWR does have active safety systems, the safety grade systems are all passive and do not provide active pool mixing. Therefore, the thermal stratification of the SP due to blowdown through the main vents and Safety Relief Valves (SRVs) as well as venting through the PCC vent are of primary importance for licensing calculations. The clearing and subsequent venting of noncondensible gases and steam over a wide range of fluxes and at a variety of submergence depths result in a wide variety of phenomena that can impact the thermal stratification in the suppression pool.

Much work has been done in the past on various aspects of the SP behavior. GE conducted a series of tests that looked at the SP behavior during the blowdown period of a loss-of-coolant accident (LOCA). The tests were performed at the Pressure Suppression Test Facility (PSTF). These tests provided data on SP behavior at a variety of scales – full scale (Varzaly et al, 1978), one third area scale (Varzaly et al, 1977) and one-ninth area scale (Varzaly et al, 1980). These tests are collectively referred to as the PSTF tests. The primary emphasis of these tests was on SP mechanical loading, although some data on thermal behavior was also reported. Although this blowdown is a violent high-energy period tests have shown that a significant amount of stratification can exist at its conclusion.

Later work looked at the effects of the venting of steam and noncondensibles from the Passive Containment Cooling (PCC) condenser used in the decay heat period by the SBWR and ESBWR (Coddington & Andriani, 1995).

This work studies the various phases and phenomena of the blowdown period of a LOCA and identifies those that are important to thermal stratification of the SP. This is a significant departure from much past work since the phenomena important to thermal stratification are different than those important to structural loading, which has been studied exhaustively in the past. The paper identifies the important phenomena and the scaling necessary to model them in reduced size tests. This is important in determining which of the large body of structural loading tests are adequate for application to the stratification problem. Analytical models are developed for the buoyant jet structures that provide the dominant mechanism for pool mixing and stratification. Analytical models for the SP response must be based on our understanding of free jets, however, the actual situation has closely spaced jets and 3-D effects which are important. Therefore,

analytical models provide only qualitative understanding, detailed 3-D modeling is needed for quantitative assessment.

In an effort to evaluate the effectiveness of our analytical models a simplified treatment capturing the main characteristics of the SP behavior is implemented into the TRACG system code and used to predict the behavior of one of the PSTF tests. A simplified set of models is appropriate for application in large control volume system codes like TRAC and RELAP.

2 SUPPRESSION POOL TRANSIENT PHASES AND ANALYSIS

This section reviews the possible causes of stratification in the suppression pool, identifies which ones are important and describes analytical models developed to capture the primary characteristics of the SP thermal behavior.

Fig. 1 shows the containment and main vent system for the SBWR. Fig. 2 shows the behavior of key main vent parameters throughout the phases of the blowdown portion of a LOCA. When a LOCA occurs, steam or high-energy liquid is injected into the drywell (DW) resulting in rapid pressurization of the DW, which in turn causes a rapid

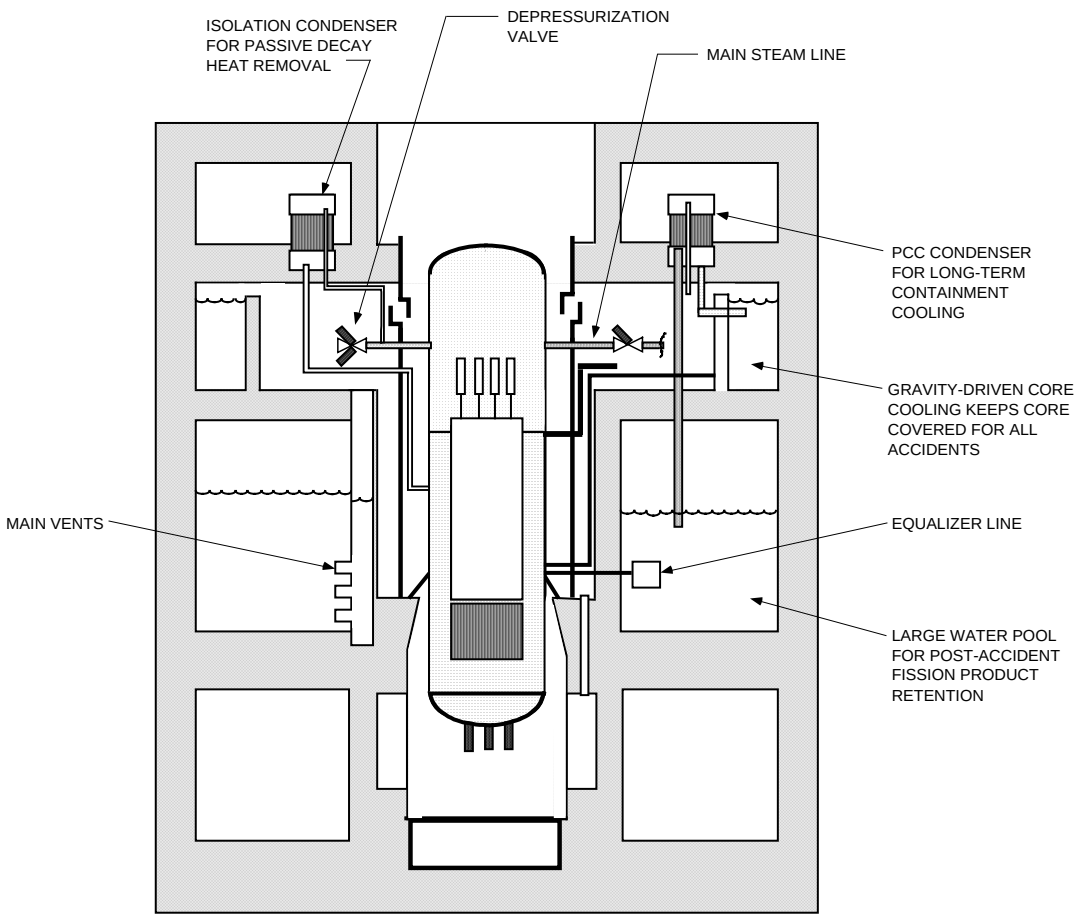

Fig. 1 SBWR Containment and Main Vents

clearing of the main vent system. Initially there is a water level in the vertical portion of the vent as shown in Fig. 1. During the initial blowdown, the liquid is forced from the vents sending jets of water into the suppression pool. Vent clearing time is on the order of 2 seconds. This is followed by an injection of noncondensible gases and steam. The noncondensible concentration decreases rapidly from 100% to less than 10% in approximately 10 sec. Following this there is a longer period of injection of a mixture rich in steam. The steam injection period can last many minutes. The next subsections provide a review of these phases of a LOCA transient and analytical descriptions of the important phenomena present.

2.1 Vent Clearing

The initial clearing of the water in the vents results in transient jets of liquid that traverse the pool. When each jet reaches the far wall it forms a radial wall jet spreading in all directions (Fig. 3). The behavior is complicated by the fact that the jet is transient (a starting jet) and by the fact that adjacent jets may interact with each other. In the SBWR, there are eight to ten sets of main vents circumferentially spaced 36-45 degrees apart, each containing three vertically-stacked vents. The degree to which the jets overlap when they reach the far pool wall depends on the width of the pool. Some fraction of the jet will move up along the wall to the surface of the pool and come back across the pool surface.

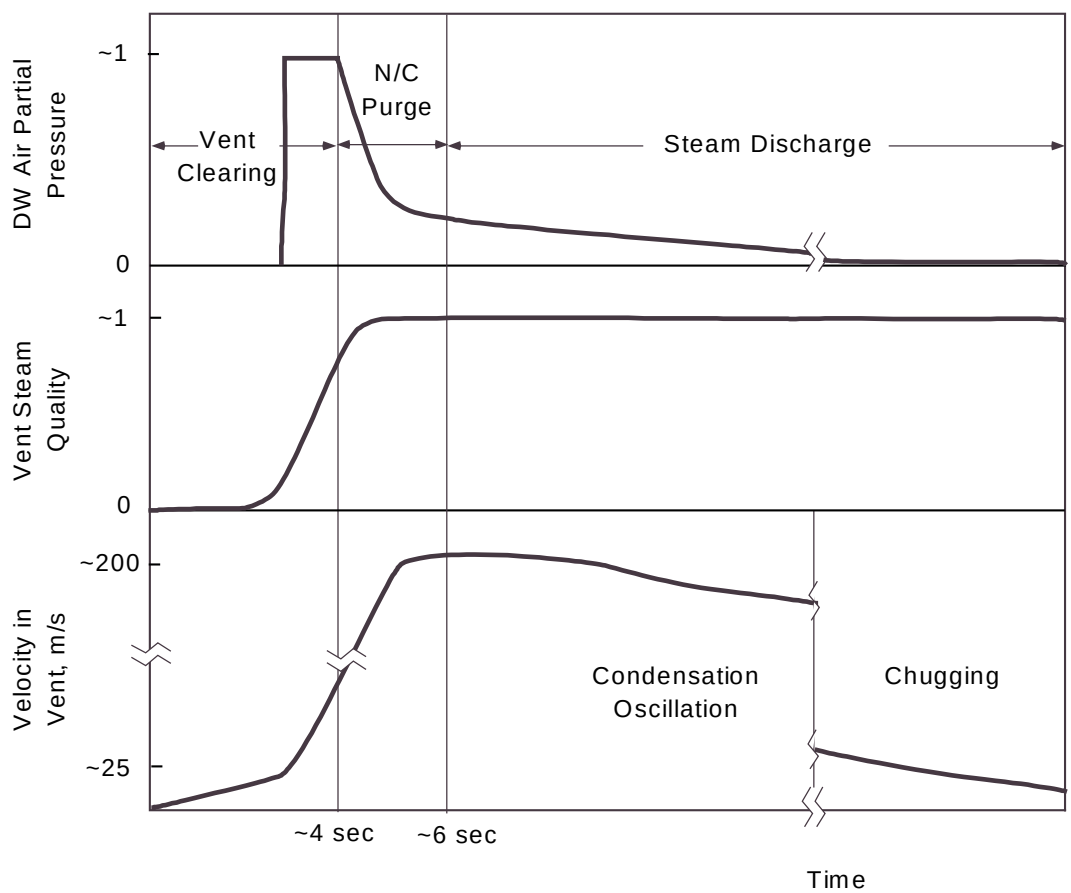

Fig. 2 Characterization of Suppression Pool and Main Vent Behavior

The behavior of jets has been studied extensively and there are very good integral correlations supported by experimental results for their behavior. Below, correlations are used from the literature to estimate the velocity, width and entrainment rates of forced jets.

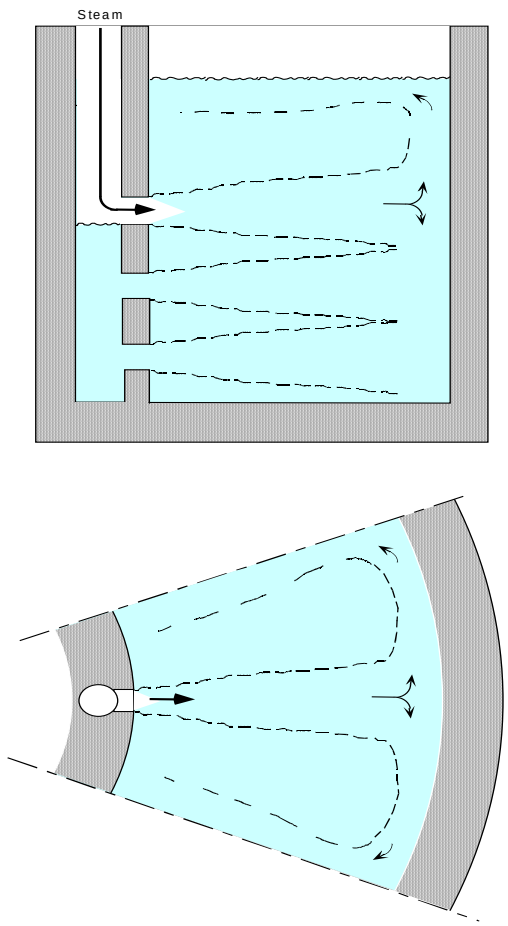

Fig. 3 Jet Trajectory in Suppression Pool

2.1.1 Buoyant Jet Characterization

The jet Reynolds number determines the basic character of the jet

$$\mathrm{Re}_{jet} = \frac{u_o D_o}{\nu} \tag{1}$$

For Reynolds numbers greater than a few thousand, the jet will be turbulent (Rajaratnam, 1976). This is the case for the jets encountered in the SP. Table 1 shows Reynolds numbers for the PSTF test and the SBWR.

If the jet is warmer than the pool or contains steam or noncondensible gases, it will be buoyant. The balance between the buoyancy and inertia will determine whether each jet behaves as a forced jet or a plume. The Richardson number characterizes the transition

$$Ri = \frac{Gr}{\mathrm{Re}^2} = \left(\frac{\rho_a - \rho_{jet}}{\rho_a}\right)\frac{g \cdot D_o}{u_o^{\,2}} \tag{2}$$

where

$$Gr = g\left(\frac{\rho_a - \rho_{jet}}{\rho_a}\right)\frac{D_o^{\,3}}{\nu^2} \tag{3}$$

is the Grashof number.

As the jet moves across the pool and entrains liquid from the pool, the jet maximum velocity and average temperature decrease. The inertia decreases faster than the buoyancy, however, and at some point buoyancy becomes important. The jet transitions to buoyant behavior at a distance

$$x_{trans} = \left(\frac{\pi}{2}\right)^{1/2} \frac{D_o}{Ri^{1/2}} \tag{4}$$

from its discharge point (Gebhart et al, 1988). For the conditions during jet clearing, the Richardson number is much less than 1 and the resulting transition distance is longer than the pool width so that the jet will behave as a forced jet all the way across the pool with very little upward motion due to buoyancy. Table 1 gives the values for the SBWR and test. The next sections describe the details of the transport process for forced jets.

2.1.2 Forced Turbulent Jets

Non-buoyant steady jets are characterized by constant momentum flux along their length. The first portion of a jet is an entry region where the jet velocity and radius vary only slightly. This region extends to approximately four to five jet diameters downstream. Within this region, the shear layer between the fast moving jet and ambient pool fluid is expanding to reach the centerline of the jet (Fig. 4). At a distance of four to five jet diameters the diffusion has reached the centerline and the potential core of the jet has disappeared. In this entrance region the rate of jet expansion is slower than in the fully developed region. The development given by Gauntner et al (1970) for this region can be linearized to get the following relations for the jet centerline and radius

$$u_{\text{centerline}} = u_o \qquad \text{for } x/r_o \le 8.75 \tag{5}$$

$$\frac{r_{1/2}(x)}{r_o} = \left(1 + 0.013\, {}^{x}\!/_{r_o}\right) \tag{6}$$

Here, the end of the entry region has been selected as x/r_o = 8.75 which falls within the range of different experimental data. The results are not very sensitive to this selection. The radius, $r_{1/2}$, is based on the point where the velocity is equal to one half the centerline velocity.

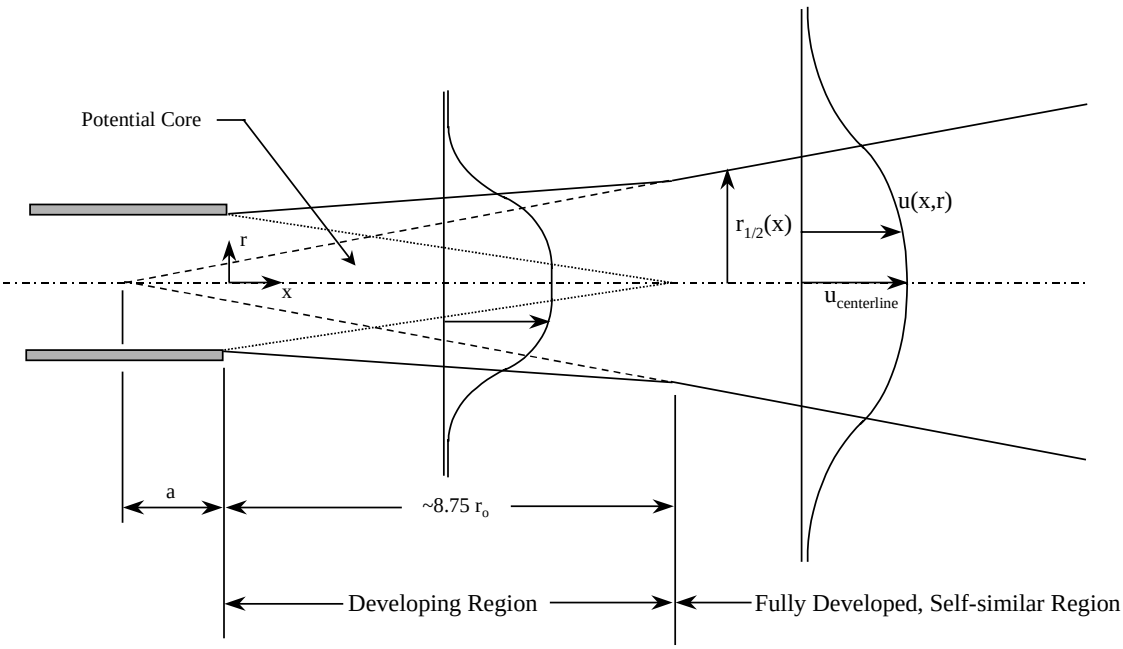

Fig. 4 Developing and Fully Developed Regions of a Jet

Beyond this entry region the jet assumes a self-similar profile. Hinze (1959) has shown that the centerline velocity decays hyperbolically with axial distance in this region. Schlichting (1960) suggests that the jet grows linearly with axial distance in this region with a growth rate or dr/dx = 0.0848 for the jet half width. Matching this with equation (6) at x/r_o = 8.75 yields the relation

$$\frac{r_{1/2}(x)}{r_o} = 0.848\left(4.39 + x/r_o\right) \tag{7}$$

Schlichting also gives the rate of centerline velocity decay as

$$\frac{u_{centerline}(x)}{u_o} = \frac{13.14}{\left(a + x/r_o\right)} \qquad \text{for } x/r_o > 8.75 \tag{8}$$

where a is the distance from the virtual origin to the beginning of the jet and is equal to 4.39 from equation (7). The axial velocity variation with radial distance has been matched well with several different profiles including the Gaussian error curve and cosine curve. The form recommended by Schlichting is used here,

$$\frac{u(x,r)}{u_{centerline}} = \left(\frac{1+\eta^2}{4}\right)^{-2} \tag{9}$$

where $\eta = 15.6\frac{r}{x}$

The entrainment by the jet as it moves across the pool is given by (Peterson, 1994)

$$\frac{Q_e}{Q_o} = 2\sqrt{2}\alpha_t \frac{x}{r_o} \tag{10}$$

where Q_o is the initial flow rate and α_t is Taylor's entrainment coefficient which has a value of about 0.05. The suppression pool has an x/r_o of about sixteen so the entrainment by the jet as it crosses the pool is about $Q_e/Q_o = 2.3$.

These relations are for individual steady jets traveling in an unconfined space. These assumptions are challenged by the geometry of the suppression pool where interactions with walls and other jets occur. For typical conditions in an SBWR blowdown flow, the superposed velocity profile for three vents is shown in Fig. 5. As indicated, there is an overlap between the jets. The cumulative jet looks more like a

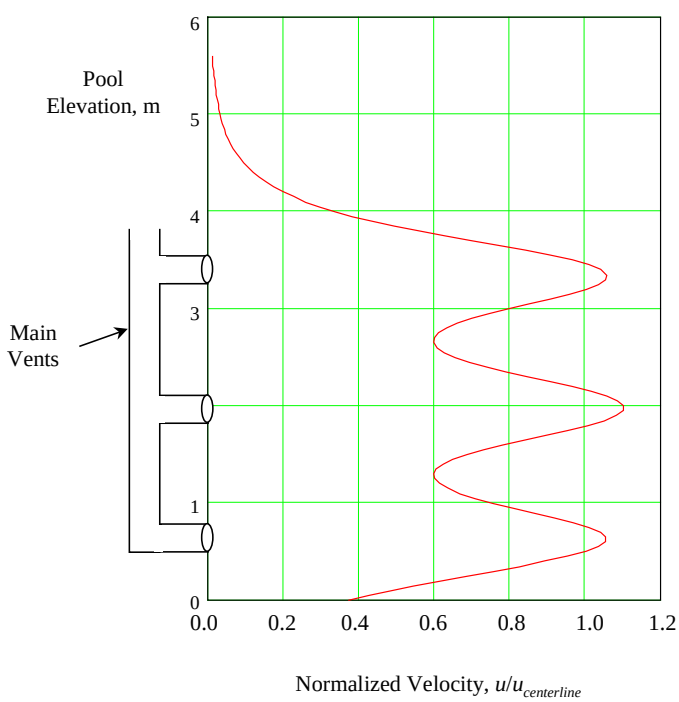

Fig. 5 Horizontal Velocity Profile of Vent Discharge Jets Approaching the Far Wall

rectangular jet. Experiments have shown that in this region for a rectangular jet there is no growth in the vertical direction and the jet expands in the horizontal direction linearly with distance, similar to a plane jet (Sfeir, 1976). This velocity decay is slower than for an axisymmetric jet (proportional to square root of distance rather than linear with distance). There will be some additional smoothing of the velocity profile to reduce the peaks along the centerlines of the original jets so the centerline velocity can be expected to decay at a rate between an axisymmetric jet and a rectangular one. In the current analysis the axisymmetric approximations above are used. Future work is planned to address this further.

When a jet hits the far vertical wall it will expand into a radial jet moving out along the wall in all directions (Poreh et al, 1967) (Fig. 6). This motion will also be limited by the expansion of adjacent jets. The maximum velocity in the wall jet from a perpendicularly impinging round jet is given as (Dodge & Ricker, 1978)

$$\frac{u_r}{u_o} = \frac{3.08}{\left(\frac{z}{r_o}\right)^{1.12}} \qquad \text{for } z > 0.4\,H \tag{11}$$

where u_o is the velocity at the original jet source, H is the distance from the jet source to the wall (i.e. the pool length) and z is the distance along the wall from the impingement stagnation point. Poreh et al (1967) gives a similar relation, although theirs has a slight dependence on the height-to-diameter ratio, H/r_o, not seen in eq (11). Poreh et al also give a relation for the jet thickness as

$$\frac{\delta_r}{H} = 0.098\left(\frac{z}{H}\right)^{0.9} \tag{12}$$

Using the results above for the impinging round jet, the jet maximum velocity and thickness of the radial jet when it reached the surface of the pool, if undisturbed by the surface, would be

$$\frac{u_r(L_{sub})}{u_o} = \frac{3.08}{\left(\frac{L_{sub}}{r_o}\right)^{1.12}} = 0.2 \tag{13}$$

and

$$\frac{\delta_r}{H} = 0.098\left(\frac{L_{sub}}{H}\right)^{0.9} = 0.1 \tag{14}$$

where L_{sub} is the submergence of the jet when it impinges on the wall.

If the jet is very strong when it hits the surface it will cause surface waves that will quickly dissipate the jet energy. This interaction is governed by the impingement Froude number (Jirka & Harleman, 1979)

$$Fr_{imp} = \left[\frac{u^2}{g\frac{\delta_r}{2}} \right]^{1/2} \tag{15}$$

For small surface Froude numbers there are very little surface interactions and the pool surface acts as a wall. For the purposes of this analysis the effects of surface waves are neglected and the surface is assumed to act as a solid wall with no friction.

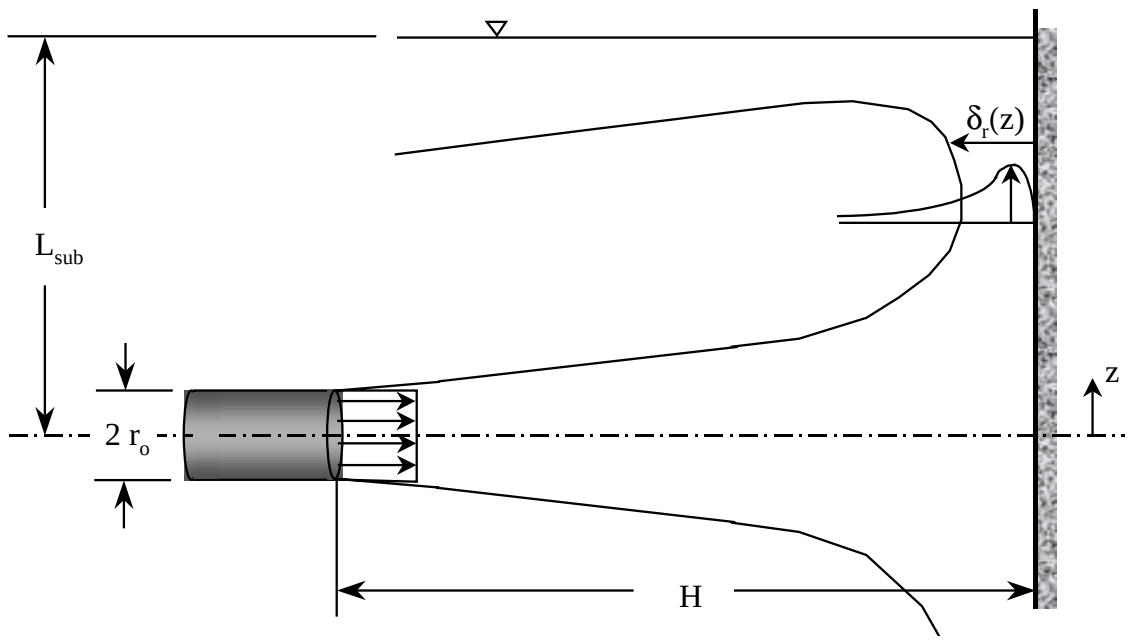

Fig. 6 Impinging Jet

The jet will next spread along the surface of the pool. Jirka and Harleman (1979) show that for forced jets the non-dimensional surface layer thickness, t/L_{sub}, falls in the range 0.15 to 0.18 over almost all conditions. For the dimensions of the SBWR suppression pool, the surface layer thickness will be approximately 0.3m. If the velocity of the surface layer is too high, so that inertia forces substantially exceed buoyancy forces, it will become unstable and expand to a thicker layer (Jirka & Harleman, 1979). Another Froude number characterizes the instability,

$$Fr_{surf} = \frac{u_{surf}}{\sqrt{\beta_{pool}\, g\left(T_{surf} - T_{pool}\right) t_{surf}}} \tag{16}$$

The Froude number for the conditions in the SP indicate that the surface layer will be unstable in which case a hydraulic jump will occur and the surface layer will grow to a thickness of t_{surf}/L_{sub}= 0.7 or t_{surf} = 1.5m. The distance over which this transition occurs is long compared to the pool width. Therefore, the surface layer will be in the transition phase as it moves across the pool. The liquid clears from the vents in approximately 1 second but the effects of the jet moving around the pool may be present for longer.

Therefore a portion of the liquid from the vents will be deposited along the surface of the SP in a 0.3 to 1.5m thick layer. This effect is not important for the SBWR where the vent liquid is very close in temperature to the pool temperature. However, in some of the suppression pool simulation tests considered later, the liquid in the upper portions of the main vents was heated – in some cases to near saturation temperature – as a result of test preconditioning.

For a worst case of saturated liquid in the vents, which occurs during preconditioning in experiments but not in actual reactors, the layer temperature could be 20K above the average SP temperature. So, although this period is brief, it can provide an important part of the energy added to the surface of the pool if the liquid in the vents is initially warmer than the pool.

2.2 Noncondensible/Steam Injection

After the main vents clear, steam and noncondensible gases vent from the DW to the WW through the main vents. The timing and composition of the discharge are geometry and initial condition dependent. Integral system blowdown tests (Grafton and Seely, 1978) indicate an initial discharge with large noncondensible gas concentration that quickly decreases to a flow of predominantly steam as depicted in Fig. 2. In the case of the SBWR, there may be a longer period in which there is a combination of steam and noncondensible discharge from the vents as a result of less complete mixing in the more complicated DW geometry.

The noncondensible gases discharged into the pool are very buoyant. Although they are discharged at a high velocity, the buoyancy forces dominate and the noncondensible gases rise to the surface of the suppression pool causing significant pool swell (Varzaly et al, 1978). The buoyancy source and resulting plume can result in some circulation in the pool, however, in experiments, the noncondensible injection period is brief and results in very little circulation, mostly upward motion of the pool. In experiments, the noncondensibles introduce a negligible amount of energy to the pool since no condensation takes place. The steam injection period, which follows, lasts much longer and adds most of the energy deposited in the pool.

2.3 Steam Discharge Jet

Many researchers have looked at the condensation of steam discharged into pools and many complex models have been developed to predict pressure oscillations and the distance required for complete condensation of the steam (Chun et al, 1996, Weimer et al, 1973, Kudo et al, 1974, Cumo et al, 1978, Tin et al, 1982, Simpson & Chan, 1982, Nariai & Aya, 1986). For our purposes the important result from this work is that the steam is

condensed over a short distance (0.4 to 1.5 times the vent diameter) so that we can look at the liquid exiting the condensation region for its effects on the pool thermal behavior (Fig. 7). The important parameters for us then are the entrainment rate in this region and the momentum of the fluid exiting the region. A simplified analytical approach is described below.

The steam exiting the vent entrains liquid from the surrounding pool (Fig. 7). It is reasonable to assume that the high velocity steam will continue moving horizontally resulting in a mixing region that maintains an approximately constant diameter as shown in the figure.

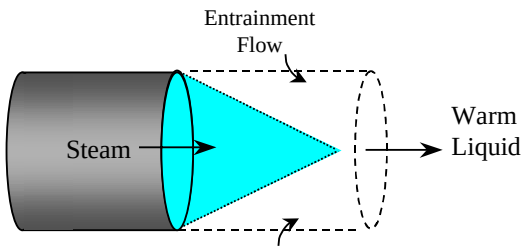

Fig. 7 Steam Jet Condensing at Vent Exit

With the assumption of a constant mixing region diameter, conservation of momentum yields an equation for the velocity of the jet exiting this condensing region

$$u_{liq.jet} = u_{steam}\sqrt{\frac{\rho_{steam}}{\rho_{liq.jet}}} \tag{17}$$

Typical steam and liquid velocities are 150 m/s and 5 m/s, respectively. So there is a large reduction in the velocity. The entrainment ratio of pool flow to steam flow in this condensing process is approximately thirty-to-one so that the velocity and temperature of the steam discharge are reduced substantially.

An energy balance on the mixing region yields a relation for the enthalpy of the liquid exiting the mixing region

$$h_{liq.jet} = \frac{h_{steam}}{\phi} + \left(1 - \frac{1}{\phi}\right)h_{pool} \tag{18}$$

where ϕ is the ratio of flow exiting the mixing region to vent steam flow given by

$$\phi = \frac{\dot{m}_{liq.jet}}{\dot{m}_{steam}} = \sqrt{\frac{\rho_{liq.jet}}{\rho_{steam}}} \tag{19}$$

For typical plant conditions the steam, pool and liquid jet temperatures are:

T_{steam} = 394K

T_{pool} = 296K

$T_{liq.\ jet}$ = 317K

So the liquid is warmer than the pool by approximately 20K.

Thus, for typical conditions, we have a liquid jet entering the pool with a diameter equal to the vent diameter, velocity on the order of 5 m/s and temperature about 20K hotter than the pool. This condition is achieved within 1.5 diameters of the vent exit. The jet will move across the pool and hit the far wall taking mass and energy with it. This is the primary mechanism by which energy is transported around the pool.

The jet behavior is similar to that of the jet from vent clearing described above except that this jet more closely approaches a steady jet. The jets behavior can be predicted with the same relations used above. Pool

As the steam flow through the vents diminishes, buoyancy eventually becomes dominant and the warm liquid rises as a buoyant plume. This occurs at very low steam flows so that the fraction of total energy input during the buoyant phase is quite low. The transition is given by eq. (4) and occurs at a velocity of approximately 1.5 m/s. At low flow velocities and low noncondensible content, chugging can begin to occur.

Fig. 8 shows a flow regime map indicating the conditions for different types of flow to occur (Lahey & Moody, 1993). Chugging will commence at low flows and results in large oscillations in the steam-liquid interface (Fitzimmons et al, 1979). Unlike condensation oscillations, chugging does cause large-scale motion in the pool and can enhance mixing. This work does not address the possible chugging phase of the transient.

3 SCALING

The descriptions above have identified some of the parameters that determine the behavior of jets in the SP. This section identifies some additional parameters that are important to SP behavior and thus should be considered when using scaled test facilities. Numerical values for the scaling parameters are shown in Table 1.

Scaling of test facilities to date (Varzaly et al, 1977 and 1978 and Varzaly et al, 1980) was done using the familiar power-to-volume full height scaling methodology as described by Yadigaroglu (1996). This results in one-to-one time scaling and ensures good top-down scaling of the facilities. As a result, mass and energy additions are proportional to mass and energy capacities of the system volumes. The energy scaling is characterized by the ratio of energy input to pool thermal capacity

$$\frac{\Delta E_{RPV}}{E_{pool\,capacity}} = \frac{\Delta(me)_{RPV}}{m_{pool} c_{p,pool} \Delta T_{ref}} \tag{20}$$

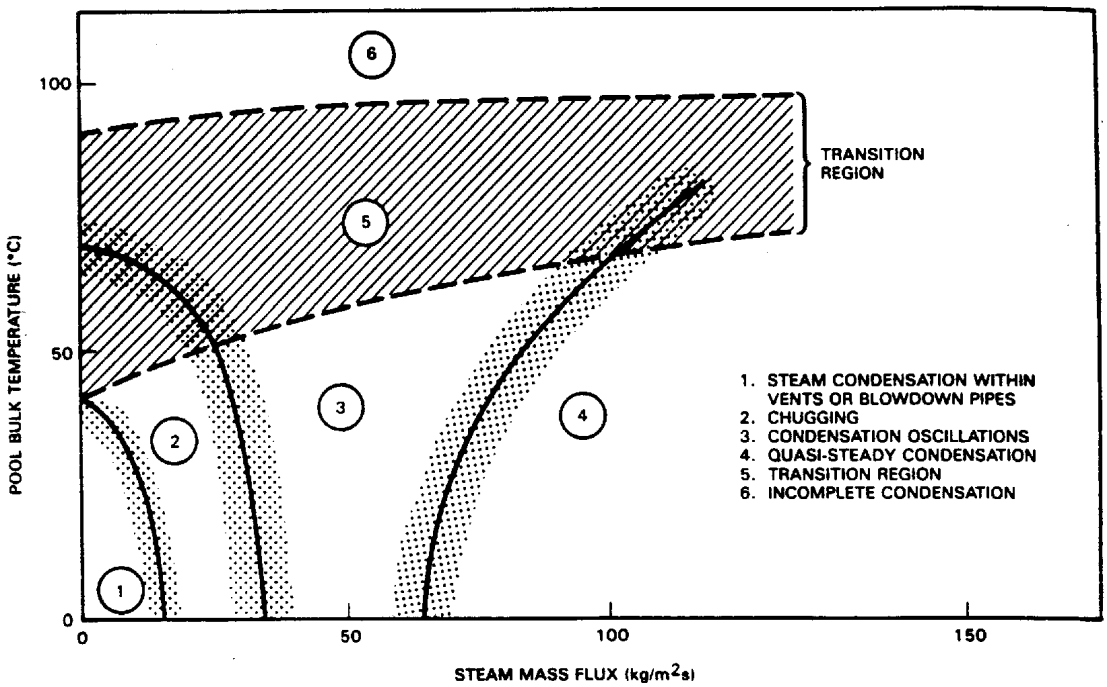

Fig. 8 Flow Regime Map for Pure Steam Discharge

where $\Delta(me)_{RPV}$ is the change in internal energy in the reactor pressure vessel (RPV) during blowdown, m_{pool} and $c_{\text{p,pool}}$ are the mass and specific heat of the suppression pool and ΔT_{ref} is a reference value for the temperature change of the SP (taken as the subcooling). Since the DW acts as a passive surge volume between the RPV and WW the vent mass and energy flow rates are approximately equal to those leaving the RPV and the stored RPV energy discharged is used to represent the energy input to the pool.

The mass scaling is characterized by the ratio of mass injected into the SP to pool mass

$$\frac{\Delta m_{RPV}}{m_{pool}} \tag{21}$$

where again the RPV flow is taken as the flow into the SP. Since the RPV pressures are prototypical, we can neglect them in the scaling and represent the mass flow rate scaling as

$$\frac{\dot{m}_{RPV}}{m_{pool}} \propto \frac{\rho_o A_{choked} u_o}{m_{pool}} \tag{22}$$

where A_{choked} is the critical flow area from the RPV to DW and ρ_o and u_o are reference density and velocities for the choked flow corresponding to the initial RPV pressure. Similarly the rate of energy input into the pool is scaled by

$$\frac{\dot{E}_{RPV}}{E_{pool\,capacity}} = \frac{(\dot{m}h)_{RPV}}{m_{pool} c_{p,pool} \Delta T_{ref}} \tag{23}$$

In addition to the mean values in the pool we are interested in the local temperatures that result from suppression pool stratification. To predict stratification in the pool, the behavior of local phenomena such as jet volumes and flow regime are important. These are characterized by the bottom-up scaling parameters. Many of these were defined in the previous section. Some additional bottom-up parameters are defined below.

The jet to pool volume ratio characterizes how much of the fluid is in the jet versus in the ambient pool region. This can also be an indication of how much interaction the jet will have with other jets and the pool walls. For this purpose the volume of the jet traversing the pool from the vent to the containment wall is used. It is given by,

$$\frac{V_{jet}}{V_{pool}} \tag{24}$$

which will characterize the fraction of the pool that is in the jets. This has an impact on both the residence time in the jet and how well defined the jets are.

The jet transit (or residence) time indicates the time it will take for energy and momentum to be transferred around the pool by the jets. The transit time is given by,

$$\tau_{jet} = \frac{L}{\overline{V}} \tag{25}$$

where L is the length traveled and $\overline{V}$ is the average velocity in the jet. The transit time varies somewhat from one scale to another since the power to volume scaling results in one-to-one scaling of the velocities but the length scale varies with the square root of the facility scale. For reduced geometric scale tests, the transit time is much shorter than for full scale leading to accelerated time scaling for the distribution of energy.

For high Reynolds numbers and low buoyancy the jet will mix the pool well. The pool Richardson number indicates when the inertia in a jet will cause stratification to break down in a pool (Jirka, 1982). This is given by

$$Ri = \frac{Gr}{\mathrm{Re}^2} = \left(\frac{\rho_a - \rho_{jet}}{\rho_a}\right)\frac{g \cdot D_o}{u_o^{\,2}}\left(\frac{H_{sf}}{D_o}\right)^2 \tag{26}$$

where H_{sf} is the depth of the stratified fluid in this case L_{sub}. For Ri less than 0.05 the inertial forces will overcome the buoyancy effects and the pool will become well mixed. However, the time constant to mix the pool can be very long. Therefore stratification may exist for a long time relative to the blowdown period as seen in the tests.

3.1 Scaled Test Facilities

As a part of a Mark III pressure suppression containment confirmatory test program, General Electric performed a series of full and reduced scale integral system tests in the Pressure Suppression Test Facility (PSTF). This test facility as configured for the different test series is described in more detail in Varzaly et al (1977), Varzaly et al (1978) and Varzaly et al (1980). The analysis described above was used to predict the surface temperatures in one of the tests from these test series in an effort to evaluate the effectiveness of the equations in predicting SP surface temperatures.

A schematic typical of the three test setups is shown in Fig. 9. In the PSTF test configuration an electrically heated pressure vessel simulated the RPV. The RPV was connected to another pressure vessel, which simulated the DW, by a blowdown line, which included a critical flow venturi, rupture disc assembly, and a gate valve. The rupture disk in the blowdown pipe simulated the breaking of a main steamline, and the venturi upstream of the rupture disk set the size of the simulated break. The DW vessel was connected via a discharge duct to a set of three Mark III horizontal vents, which discharged into a simulated sector of a Mark III suppression pool. The WW air space was open to the atmosphere, and this was done to simulate the large enclosed WW air space of the Mark III containment configuration.

The scaling parameters described above were evaluated for the SBWR and test facility to assess the applicability of these facilities in predicting the behavior of the SBWR SP. Table 1 presents the results. Despite the fact that they were designed for SP loading, the results indicate that the facility scaling is also good for thermal stratification modeling. The power-to-volume scaling used results in good scaling of both the top-down parameters relating mass and energy inputs to volume storage capacities and the bottom-up parameters defining the behavior of jets. The primary distortion comes from the reduced aspect ratio of the smaller scale experiments. This shows up in the volume and length of the jets relative to the SP volume. As a result the jet residence time is shorter in the small-scale facilities and the transit time for mass and energy moving around the pool through jets will be shorter. Consequently, the transition from a slightly stratified to a well-mixed pool progressed more quickly in the smaller experiments. Since the duration of these blowdown experiments was relatively short the full effect of this is not seen in the test data.

4 APPLICATION USING TRACG

The concepts described in section 2 were implemented into a large system code, TRACG (Andersen et al, 1986) in an effort to predict the stratification in one of the scaled SP tests. The test is a one third scale test in the PSTF designated test, 5807-30 (Varzaly et al, 1977). The test consisted of an eight-degree segment of the suppression pool with three vents aligned vertically as shown in Fig 9. The temperature data available for the test is too coarse to provide direct indication of the small-scale jet structures expected in the SP. However comparisons of the resulting pool temperatures can provide indirect evidence to confirm the behavior of jets within the pool.

Table 1 Scaling Parameter Comparison

Top-Down Parameters	**SBWR**		**1/3 Scale 5807**	
$\Delta E_{RPV}/E_{pool\ capacity}$	0.26		0.16	
$\Delta m_{RPV}/m_{pool}$	0.07		0.045	
$\dot{m}_{RPV} / m_{pool}$, sec^{-1}	0.0007		0.0016	
$\dot{E}_{RPV} / E_{pool\ capacity}$, sec^{-1}	0.0025		0.0014	
V_{jet}/V_{pool}	0.059		0.046	
	Vent Clearing Phase		**Steam/noncondensible Phase**	
Bottom-Up Parameters	**SBWR**	**1/3 Scale 5807**	**SBWR**	**1/3 Scale 5807**
Re_{jet}	5.6E6	3.2E6	3.5E7	4.6E6
τ_{jet}, sec	5.4	1.8	6.9	1.3
Ri_{jet}	-[1]	0.005	0.0046	0.0007
Ri_{pool}	-[1]	0.15	0.045	0.02
Fr_{imp}	1.4	0.85	1.1	1.2
Fr_{surf}	-[1]	4.6	4.6	6.7

[1] Vent liquid is not expected to be heated above SP temperature in SBWR

TRACG does not have the ability to model small flow structures, such as jets and plumes, within its large volume cells. Therefore auxiliary models are introduced to provide a mechanism to keep track of the mass and energy transport that occurs within the jet structures in the SP. When the momentum of entering fluid is weak the fluid will be deposited in the cell directly in front of the discharge pipe. For these periods the standard TRACG model is used. Past experience has shown that in these cases, TRACG can accurately predict the pool temperatures. Chugging only occurs at low mass fluxes so any chugging is modeled by the standard TRACG model, also.

In the PSTF test series the DW contained noncondensible gases in some tests and was purged with steam in others. When the DW has been purged with steam the discharge was clearly steam flow. For tests with noncondensibles in the DW the discharge was initially noncondensible gas and then shifted quickly to steam. Due to the clean cylindrical geometry of the DW vessel in the tests, the noncondensibles cleared rapidly from the DW. This is not true for a plant DW where the geometry is irregular. In actual plants more mixing of steam and noncondensible gases will occur in the DW and some of the noncondensibles will be held up in secluded areas of the DW resulting in a gradual release. Therefore the transition from pure steam to pure vapor will be much slower in an actual plant containment.

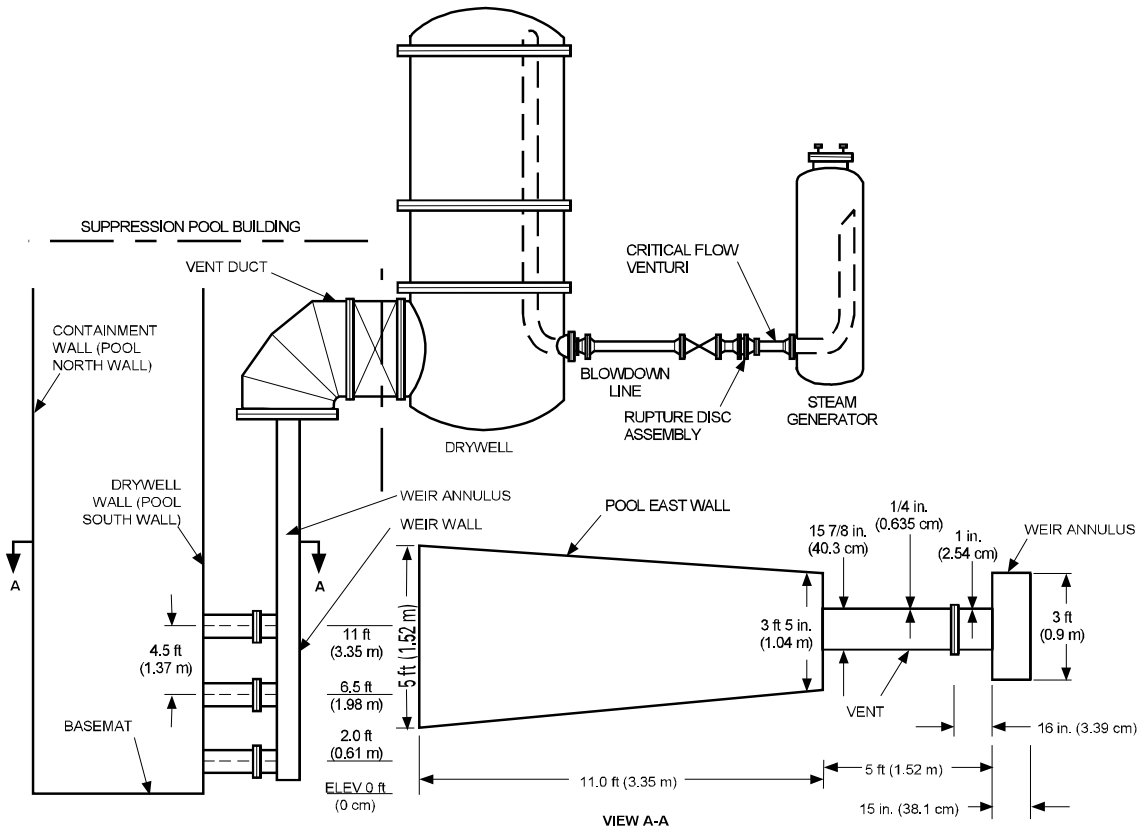

Fig. 9 PSTF Test Facility Configure for Test 5807-29

4.1 Model Implementation

When a strong discharge occurs, a TRACG "control system", controlling distributed sources and sinks, is used to model the transport of mass and energy to different parts of the pool by jets. Fig. 10 shows the locations of the sources and sinks. The control system is set up to provide a simplified version of the jets described in the previous section. Basically, the entrained liquid from a cell is modeled as a "sink". The mass and energy deposited by the jet in a cell is modeled with a "source". The temperature and flow rate of the sources and sinks are set according to the jet models described in Section 2.3.

The jet crossing the cell closest to the discharge, ring 1, entrains fluid from ring 1. The jet then hits the far wall and spreads in the form of a radial jet. The radial jet collides with jets from surrounding vents in the horizontal direction (or walls in the case of the segment tests) and in the vertical direction when the vent above or below is also open. As a result of this interaction it is assumed that half of the radial jet is deposited in the cell opposite the vent discharge, ring 2 of that elevation. The discharged fluid will contain half of the fluid discharged from the vent plus half of the fluid entrained as the jet passed through ring 1. The entrainment is calculated according to equations (10) and (19).

For the top vents (level 3), twenty five percent of the jet is deposited in the cell immediately above the discharge elevation (level 4, ring 2). This represents the remaining fluid broken up by collision with surrounding jets. Again this flow contains

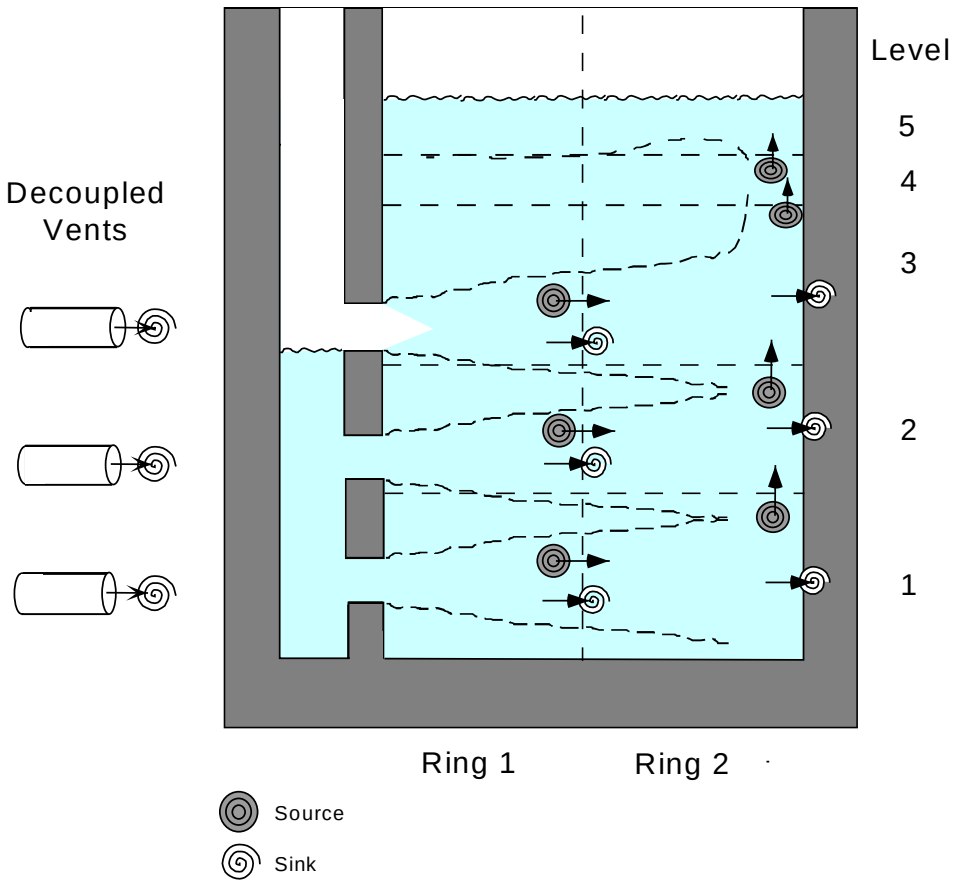

Fig. 10 TRACG Sources and Sinks used to Model Jets in Suppression Pool

vent discharge flow and entrained flow from ring 1. The additional entrainment in ring 2 is neglected because it is negligible compared to the entrainment from ring 1. Recall that the entrainment ratio of the exiting steam jet is approximately 30:1 while the additional entrainment from traversing the entire pool is only about 2.3:1.

The last twenty-five percent of the jet flow travels up along the containment wall in the form of a wall jet and is deposited in the top layer of the pool (level 5, ring 2). The top layer thickness is set to match the expected thickness of the surface layer that moves across the pool (Section 2.1.2).

For the lower two vents the second half of the jet flow is deposited in the ring above the discharge elevation in ring 2 as shown in Fig 10. This represents the remainder of the flow that was halted due to interactions with adjacent jets and structures. For these lower vents the vent above will always be open so there will be no open path to flow up along the wall towards the surface as the top vent flow does.

When the discharge jets become weak the jet model is shut off and the model reverts back to the standard TRACG model. The standard TRACG model deposits all fluid into the cell closest to the discharge. It does not model the effects of jets in the suppression pool. The transition is determined using equation (4). When the transition distance to a

buoyant jet, as calculated by equation (4), is less than the width of ring 1, the jet model is turned off.

4.2 Calculation Results

Test 5807-30 is a one-third-scale test of a large sized steam break. Data is available for the first 40 seconds of the transient. The top horizontal vent remains open throughout this period. The middle and bottom vents close at 16 seconds and 4 seconds respectively. The results obtained with the modified TRACG model are compared against the test data in Figures 11-14.

Fig. 11 shows the temperature profiles in the inner and outer ring of the pool, respectively, at various times. Values are shown both from test data and TRACG predictions. The test data plots are obtained by averaging together thermocouple readings in each region of the pool. The number of thermocouples in each region varies from one to seven. The smooth profile comes from using a smoothing function -- there are no points in between those shown in the curves.

The profiles show that the jet quickly penetrates across the pool and transfers energy to the upper layers of the pool as described in Section 2. The TRACG model implementation shows the same trends but has a time lag in depositing the energy in the

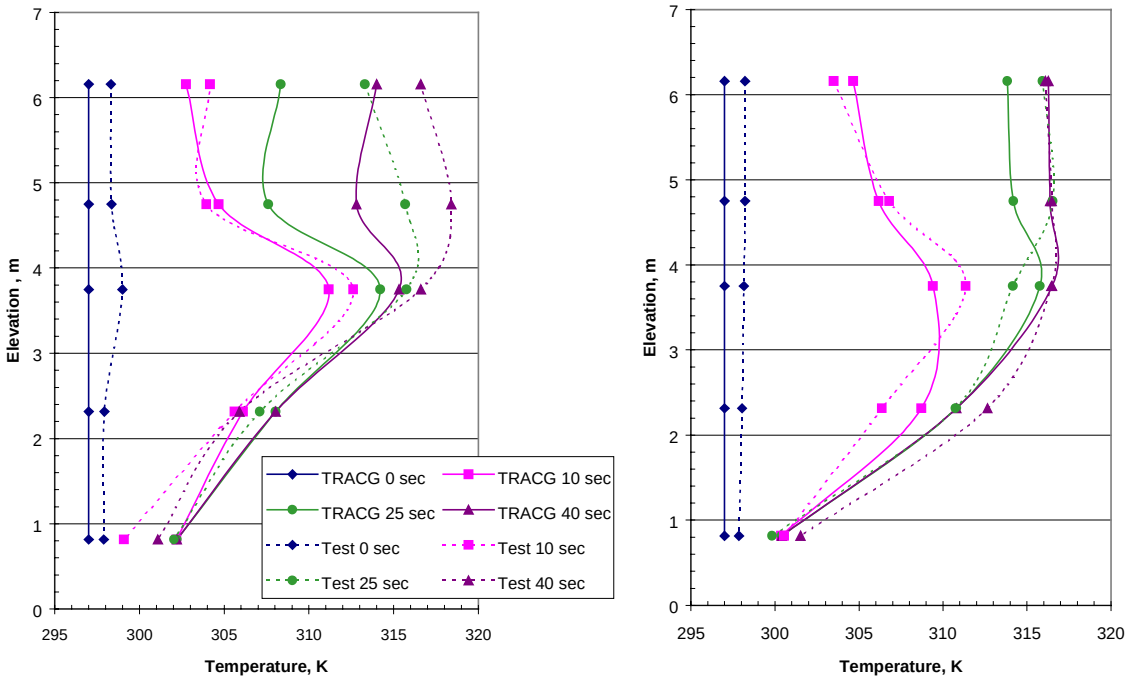

Ring 1 **Ring 2**

Fig. 11 Temperature Profiles Development in Suppression Pool

top two layers, especially in ring 1. This is probably because a jet model to carry the energy back along the surface layer was not implemented. Instead, the jet energy was deposited in ring 2 as described previously.

It appears from the test data that the pool is well mixed in the region above the top vent. However, this is partially an artifact of averaging the thermocouple measurements in each region. Figures 12 and 13 show individual thermocouple readings for the top elevation of the pool. As shown in the ring 1 data there is a significant variation even within one region. The resolution in the TRACG model does not allow these variations to be captured. In the plots, the appropriate thermocouple data is plotted along with the TRACG predictions. A diagram of the suppression pool in each figure indicates the location of the plotted temperatures. Small square and triangle shapes indicate the approximate location of the thermocouples used in the test and the gray region indicates the node plotted for TRACG.

Fig. 14 shows the increase in mixed mean temperature in the entire pool. The values for the test are estimated using the available data. Energy in the pool should be a monotonically increasing function. The oscillations are an indication of the range of uncertainty in the estimation. The error results because each thermocouple temperature is used to represent the temperature for a large portion of the pool where there might be significant temperature variations. The energy input from the TRACG simulation compares well with the energy input estimated from the data.

Test 5807-30 was initiated by purging the DW vessel with steam for an extended period of a few hours. As a result, the fluid in the upper portion of the weir was heated to near saturation temperature. This is indicated by the early temperature peak in the upper levels of the pool that is shown in much of the thermocouple data. The temperatures in the weir region were not available so they had to be estimated using the energy balance

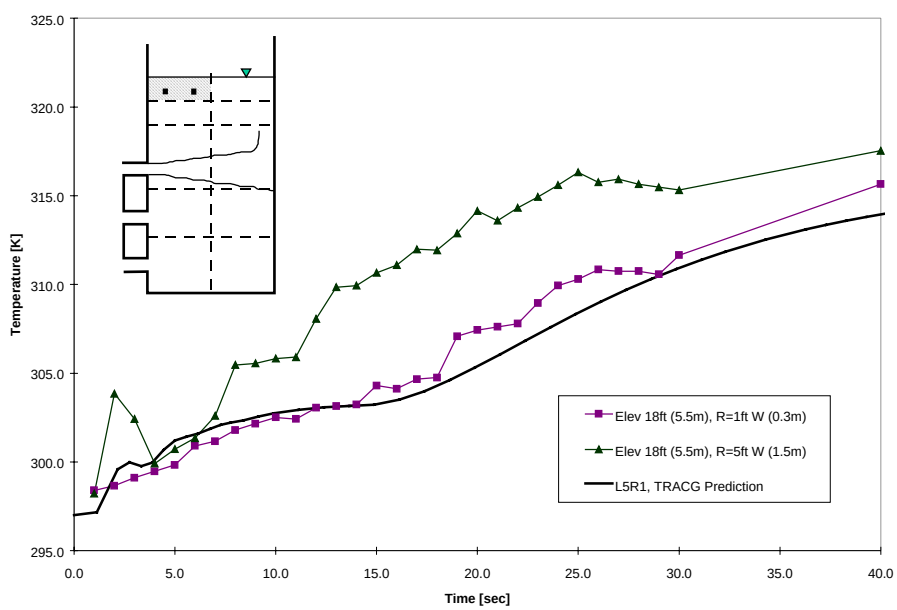

Fig. 12 Test 5807-30, SP Temperatures in Level 5, Ring 1 (Pool Surface)

for the pool. The TRACG weir temperatures were initialized to match the pool energy early in the transient. Once this was done the energy balance for the remainder of the transient matches the data well.

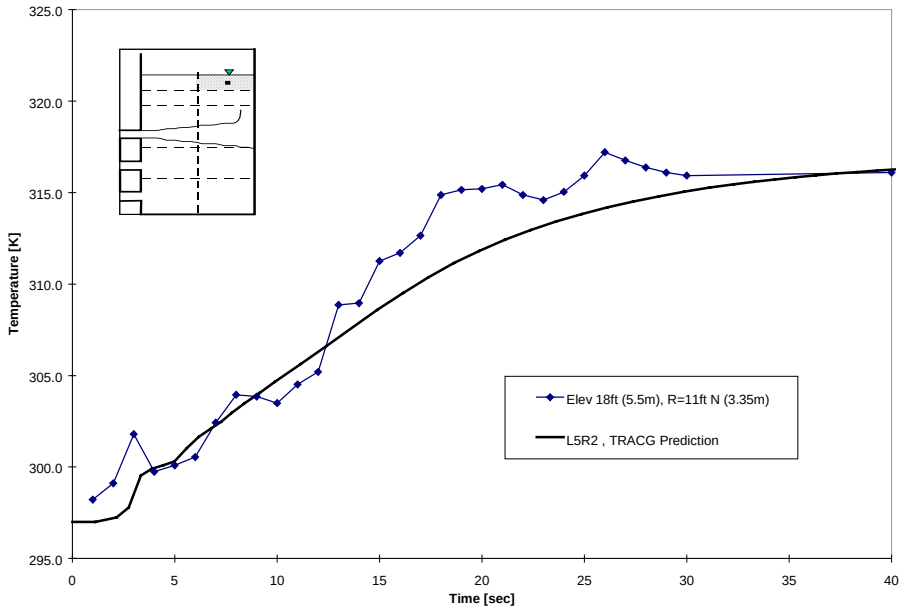

Fig. 13 Test 5807-30, SP Temperatures in Level 5, Ring 2 (Pool Surface)

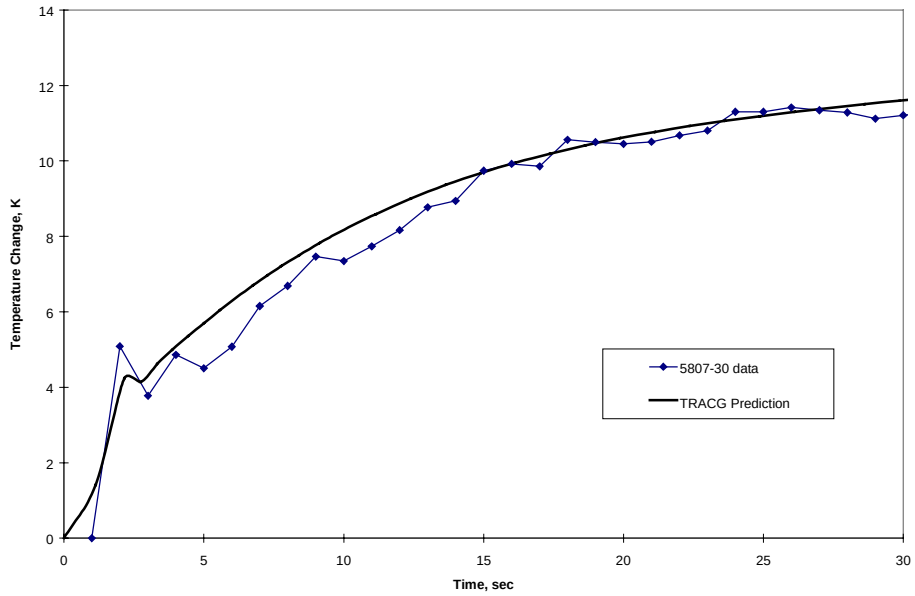

Fig. 14 Test 5807-30, Suppression Pool Mixed Mean Temperature Increase

5 CONCLUSIONS

Energy transport in the suppression pool of pressure suppression containments during the blowdown period of a loss-of-coolant accident is a high-energy, three-dimensional event. However, substantial qualitative understanding of the energy transport mechanisms in the suppression pool is gained by the use of analytical models. Integral formulations of well known free jet structures are used to construct a model to predict the influence of steam and liquid jets issuing from the main vents on thermal stratification in the pool. In doing so, interactions between adjacent jets have been neglected. The insight gained from the simplified models provides both an understanding of the scaling for pool mixing tests as well as the key parameters controlling the evolution of the pool surface temperatures.

To assess the usefulness of this simplified treatment, the analytical models are implemented into a system simulation code, TRACG, and used to model thermal stratification behavior in a scaled test facility. The results show good general agreement with the test data, however, the sparseness of the experimental data does not allow verification of the detailed local behavior in the pool. It is recommended that additional testing be undertaken to provide detailed temperature and velocity data adequate to identify the fluid structures present in the suppression pool. This testing could be supplemented with CFD analysis of the SP pool to aid in extrapolation of the data to other conditions and provide insight into the interaction of the jets.

6 NOMENCLATURE

A	area
a	distance from jet virtual origin to end of pipe (see Fig. 4)
c_p	specific heat
d	thickness of radial wall jet
D	diameter
E	energy
$\dot{E}$	energy rate
e	specific energy
Fr	Froude number
g	gravity force
Gr	Grashof number
H	distance from vent to opposite wall, height
h	specific enthlpy
L	length
m	mass
$\dot{m}$	mass flow rate
Q	volumetric flow rate
Re	Reynolds number
Ri	Richardson number
r	radial distance
T	absolute temperature
t	thickness of layer

u	velocity
V	volume
$\overline{V}$	average velocity
x	axial distance along jet
z	distance along radial wall jet
α_t	Taylor's entrainment constant
β	thermal coefficient of expansion
δ	wall jet thickness
η	similarity variable
ν	kinematic viscosity
ϕ	mass flow ratio (see eq. (19))
ρ	mass density
τ	time constant

6.1 Subscripts

½	position where axial velocity equals ½ of centerline velocity
a	ambient
c	condensation
e	entrainment
imp	impingement
o	jet exit
r	radial distance
sub	submergence
surf	surface
trans	point of transition from forced to buoyant

6.2 Acronyms

CFD	computational fluid dynamics
DW	drywell
ESBWR	european simplified boiling water reactor
LOCA	loss-of-coolant accident
PCC	passive containment cooling
PSTF	pressure suppression test facility
RPV	reactor pressure vessel
SBWR	simplified boiling water reactor
SP	suppression pool
SRV	safety relief valve
WW	wetwell

7 ACKNOWLEDGMENTS

This work was carried out with partial funding from the Electric Power Research Institute under the Advanced Light Water Reactor program.

8 REFERENCES

Andersen, J.G.M., Shaug, J.C., Shiralkar, B.S., 1986. TRAC Developments at General Electric. *Proc. 14th Water Reactor Safety Meeting*, NUREG/CR-0082, Vol. 5

Chun, M., Kim, Y., Park, J., 1996. An Investigation of Direct Condensation of Steam Jet in Subcooled Water. *Int. Comm. Heat Mass Transfer* **23**, 947-958.

Cumo, W., Farello, G.E., Ferrari, G., 1978. Direct heat Transfer in Pressure-Suppression Systems. *Proc. 6th Int. heat Transfer Conf.* **5**, 101-106.

Coddington, P., Andreani, M., 1995. SBWR PCC Vent Phenomena and Suppression Pool Mixing. *7th International Topical Meeting on Nuclear Reactor Thermal Hydraulics.*

Dodge, F.T., Ricker, R., Flow of Liquid Jets through Closely Woven Screens. *AIAA J. Spacecraft/Rockets*, 15, pp213-218, July-August 1978.

Dodge, F.T., Rogers, A.C., Lasher, L.E., Quencher Water Jet Loads Analytical Model, General Electric Report, NEDE-23539-P, August 1979.

Fitzsimmons, G.W. et al., Mark I Containment Program, Full Scale Test Program Final Report, General Electric Report, NEDO-24539, August 1979.

Gauntner, J.W., Livingood, J.N.B., Hrycak, P., Survey of Literature on Flow Characteristics of a Single Turbulent Jet Impinging on a Flat Plate, NASA TND-5652, February 1970.

Gebhart, B., Jaluria, Y., Mahajan, R.L., Sammakia, B., 1988. *Buoyancy Induced Flows and Transport*, Hemisphere, New York.

Grafton, W.A., Seely, D.S., Mark III Condensation Oscillation Data Analysis and Correlations, General Electric Report, NEDE-23972, October 1978.

Hinze, J.O., 1959. *Turbulence: An Introduction to Its Mechanism and Theory*, McGraw-Hill, New York.

Jirka, G. H., Harleman, D.R.F., 1979. Stability and Mixing of Vertical Plane Buoyant Jet in Confined Depth. *J. Fluid Mech*., **94**, 275-304.

Jirka, G. H. 1982. Turbulent Buoyant Jets in Shallow Fluid Layers. In *Turbulent Buoyant Jets and Plumes* (Edited by W. Rodi). Pergomon Press, New York.

Kudo, A., Egusa, T., Toda, S., 1974. Basic Study on Vapor Suppression. *Proc. 5th Int. heat Transfer Conf.* **3**, 221-225.

Lahey, R.T., Moody, F.J., 1993. *The Thermal Hydrualics of a Boiling Water Reactor*, 2nd ed. American Nuclear Society, Illinois. pp. 582.

Nariai, H., Aya, I., 1986. Fluid and Pressure Oscilations occurring at Direct Contact Condensation of Steam Flow with Cold Water. *Nuc. Eng. Des.* **95**, 35-45.

Peterson, P.F., 1994. Scaling and Analysis of Mixing in large Stratified Volumes. *Int. J. Heat Mass Transfer* **37** Suppl. 1, pp. 97-106.

Poreh, M., Tsuei, Y.G., Cermak, J.E., 1967. Investigation of a Turbulent Radial Wall Jet. *Journal of Applied Mechanics* **34** no. 2, pp. 457-463.

Rajaratnam, N., 1976. *Turbulent Jets*, Elsevier Scientific Publishing, New York. pp. 14.

Schlichting, H., 1960. *Boundary Layer Theory*, McGraw-Hill, New York. pp. 608.

Sfier, A.A., 1976. The Velocity and Temperature Fields of Rectangular Jets. *Int. J. Heat Mass Transfer* **19** pp. 1289-1297.

Simpson, M.E., Chan, C.K., 1982. Hydrodynamics of a Subsonic Vapor Jet in Subcooled Liquid. *Journal of Heat Transfer* **104**, 271-278.

Tin, G.D., Lavagno, E., Malandrone, M., 1982. Pressure and Temperature Measurements in a Vapour Condensing Jet. *Proc. 7th Int. heat Transfer Conf.* **6**, 159-164.

Upton, H.A., Torbeck, J.E., Billig, P.F., Duncan, J.D., Herzog, M., 1996. SBWR Design Update: Passively Safe, Nuclear Power Generation for the Twenty First Century *4th Int'l. Conf. On Nuclear Engineering* (ICONE-4) Vol. 2, pp. 379-394.

Varzaly, A.M., Grafton, W.A., Seely, D.S. Mark III Confirmatory Test Program, Full Scale Condensation and Stratification Phenomena - Test Series 5707, General Electric Report, NEDE-21853-P, August 1978.

Varzaly, A.M., Grafton, W.A., Chang, H. Mitchell, M.K. Mark III Confirmatory Test Program, 1/√3 Scale Condensation and Stratification Phenomena - Test Series 5807, General Electric Report, NEDE-21596-P, March 1977.

Varzaly, A.M., Yu, K.P., Kerinenen, J.A., Mark III Confirmatory Test Program, 1/9 Area Scale Multicell Condensation and Stratification Phenomena - Test Series 6003, General Electric Report, NEDE-24720-P, January 1980.

Weimer, J.C., Faeth, G.M., Olson, D.R., 1973. Penetration of Vapor Jets Submerged in Subcooled Liquids. *AIChE Journal* **19**, No. 3, 552-558.

Yadigaroglu, G., 1996. Derivation of General Scaling Criteria for BWR Containment Tests. *4th Int'l. Conf. On Nuclear Engineering* (ICONE-4) Vol. 1, Part-B, pp. 843-851.